Rishi Bodlos BSc.

Detailed microstructure characterization of a grade X70 steel modified with TiO2 using friction stir processing

MASTER'S THESIS

to achieve the university degree of

Diplom-Ingenieur

Master's degree programme: Advanced Materials Science

submitted to

Graz University of Technology

Supervisor:

Assoc.Prof. Dipl.-Ing. Dr.techn. Norbert Enzinger

Co-Supervisor:

Dipl.-Ing. Dr.techn. Rudolf Vallant

Institute of Materials Science, Joining and Forming

Graz, July 2018

AFFIDAVIT

I declare that I have authored this thesis independently, that I have not used other than the declared sources/resources, and that I have explicitly indicated all material which has been quoted either literally or by content from the sources used. The text document uploaded to TUGRAZonline is identical to the present master's thesis.

_____
Date

_____
Signature

Acknowledgement

I would like to thank Professor Toshihiko Koseki and Assistant Professor Shoichi Nambu from the Department of Materials Engineering, University of Tokyo for giving me guidance and access to the equipment of the Koseki-Inoue Lab my stay in Tokyo.

Furthermore, I would like to thank the FELMI-ZFE Graz for analyzing the TiO_2 powder and Dr. Rudolf Vallant for his guidance and help during the project.

Additionally, I would like to thank Professor Norbert Enzinger for his guidance and for setting up the cooperation between IMAT and Koseki-Inoue Lab enabling me to visit and work in Japan.

Index of abbreviations

Table of Contents

Abstract

X70 steel is one of several grades of high yield pipeline steels designed for the transportation of oil and natural gas, which sets a high requirement towards toughness and strength, especially towards the welded joints. To further improve the grade X70 steel, the chemical composition and production process can be modified to change the microstructures in a favorable way. A desired microstructure here is acicular ferrite, as it shows high crack toughness due to its disordered, needle shaped structure.

Goal of this thesis was to investigate the microstructure of X70 steel plates welded together with friction stir processing (FSP) and doped with TiO_2. The main focus was to detect acicular ferrite in the samples and to discover if TiO_2 plays a role in its formation. For that purpose, samples from a previous project [1] were prepared metallographically and analyzed using light optical microscopy, scanning electron microscopy and electron backscatter diffraction (EBSD).

A direct correlation of TiO_2 on the formation of acicular ferrite and could not be found in the analyzed samples. The result of the EBSD analysis however showed a correlation of TiO_2 and globular ferrite in a single sample. TiO_2 contained in the samples was found to increase wear of the WC-Co tool, especially in the center of the nugget zone. The WC in turn might have a role in the formation of martensite and possibly acicular ferrite.

Zusammenfassung

 X70 ist eine von vielen Pipeline Stahlqualitäten zum Transport von Rohöl und Gas über lange Distanzen, was hohe Ansprüche an Festigkeit und Zähigkeit stellt, vor allem an die Schweißverbindungen. Zur Verbesserung der Eigenschaften des Stahls kann die chemische Zusammensetzung und Herstellungsmethode angepasst werden um günstige Mikrostrukturen einzustellen. Eine dieser Mikrostrukturen ist Azikular-Ferrit. Er besitzt durch seine ungeordnete Mikrostruktur eine hohe Zähigkeit und kann die Rissausbreitung erschweren.

Ziel dieser Arbeit war die mikrostrukturelle Untersuchung von FSW geschweißten X70 Stahlproben mit TiO_2 Pulver als Additiv während des Schweißvorgangs. Der Fokus lag dabei in der Identifizierung von Azikular-Ferrit (AF) und in der Beurteilung, ob TiO2-Partikel die AF-Bildung bewirken bzw. fördern. Die analysierten Proben stammen aus einem vorangegangenen Projekt [1] und wurden mittels Lichtmikroskop, Rasterelektronenmikroskop und Elektronenrückstreubeugung untersucht.

Ein direkter Zusammenhang zwischen TiO_2 als Keimbildner für AF wurde nicht gefunden. Dennoch konnte mittels EBSD ein möglicher Zusammenhang zwischen TiO_2 und globularen Ferrit in einer Probe gefunden werden. Die Präsenz von TiO_2 hat zu einem erhöhten Werkzeugverschleiß geführt, wobei sich vor allem in der Schweißzone Wolframkarbid (WC) Abrieb befunden hat. Diese WC Partikel fördern vermutlich die Martensit-, sowie auch die AF Bildung.

1. Introduction and Tasks

Pipeline steels, such as the X70 type steel are generally used for the transportation of crude oil and natural gas over large distances. To assure a continuous pipeline and a long-term operation, parts need to be connected together and damages fixed without introducing weak points to the overall structure, which requires a suitable welding method. Conventional welding methods have the drawback of a loss of toughness due to the heat treatment caused by the welding process. Friction stir welding (FSW) as a welding method, when compared to conventional methods such as shielded metal arc welding (SMAW) has the advantage of being a non-melting weld procedure and limiting the loss of strength and toughness of the weld. To further limit the loss of toughness and even strengthen welded sections, the most desired microstructure, especially for low carbon steel would be acicular ferrite, which combines high strength and high toughness and therefore shows superior properties when compared to other hypo eutectoid microstructures such as bainite. [2, 3] One way of inducing acicular ferrite in steel is via additives such as TiO_2, manganese, nickel or chromium. In SMAW TiO_2 has been shown to induce the growth of acicular ferrite in steels but this has not yet been sufficiently proven for FSW. [4, 5]

The aim of this work is the analysis of 5 samples created with and without the addition of TiO_2 and to determine the effect of TiO_2 on the weld microstructure in FSW, with special focus on acicular ferrite.

After an initial microstructure investigation, searching for regions with both TiO_2 and acicular ferrite using light microscopy and electron microscopy was done, however the link between TiO_2 and acicular ferrite remained unclear. This lead to a second more throughout investigation of one of the samples (sample B) with the goal of finding a region showing an effect of TiO_2 on the microstructure of X70 steel. A notable region was found and investigated via an EBSD measurement comparing this region with same location on the reference sample. Additional samples were created via HIP to compare them to FSW but only one them was analyzed.

2. Basics and Literature research

2.1.   API 5L Pipeline steel grades

X70, the steel used in this thesis is a line pipe steel type manufactured using the API Line Pipe-5L standard or API 5L, the international equivalent being the ISO 3183 standard. Line pipes are primarily used in the oil and gas industry for the transportation of oil, gas, water and other liquids. The American Petroleum Institute differentiates in its API 5L standard between 3 main grades of steel, grade A, grade B and grade X. The grade X indicates a steel capable with a higher yield strength when compared to the A or B grade from the API Spec 5L. The numbers after the X stands for the minimum yield strength in kilopound per square inch (ksi), in the case of X70 above 70 ksi which is 70000 psi or 483 MPa. The real minimum yield strength for X70, according to the "API5L 45th Edition Specification for Line Pipe" is however 70300 psi or 485 MPa. Furthermore, API5L steels can be broken down into either PSL1 or PSL2. PSL2 steel has higher restrictions than PSL1, restricting manufacturing methods, prohibiting repair welds, including a maximum carbon equivalent and tighter restrictions on elemental composition. [6, 7]

2.2.   Microstructures in steel

2.2.1. Austenite

Austenite, named after Sir William Chandler Roberts-Austen, is the FCC form of iron. As a high temperature form of iron, it can be stabilized in steel only with the help of alloying elements.

At temperatures below 910°C and near zero carbon content austenite transforms into ferrite or below 723°C and at higher carbon contents to pearlite. Austenite as a FCC crystal is softer and more ductile than BCC iron but can dissolve carbon more readily. When cooled slowly the FCC iron changes into BCC iron and the carbon diffuses out of the FCC structure. [8 – 10]
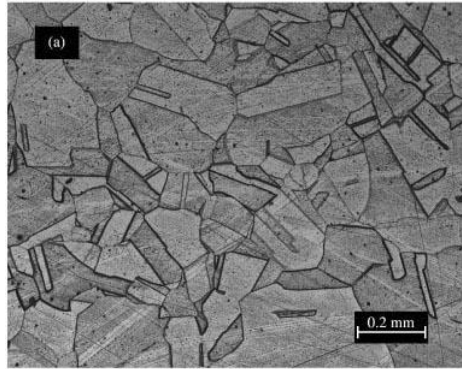
Figure 1 Microstructure of a metastable austenitic steel [11]

2.2.2. Pearlite

Pearlite, named after the mother pearl, to which the microstructure looks similar, is a 2-phase microstructure in steel. Pearlite is created during the transformation of austenite to ferrite, during which the austenite becomes supersaturated, the carbon diffuses out of the austenite cell and transforms into Fe_3C, creating a lamellar structure of alternating plates of cementite and ferrite. Overall this process is a eutectoid transformation at 0.8wt.%C. Below 0.8wt.%C proeutectoid ferrite will grow till the eutectoid concentration is reached and then pearlite will form at the grain boundaries. [12, 13]
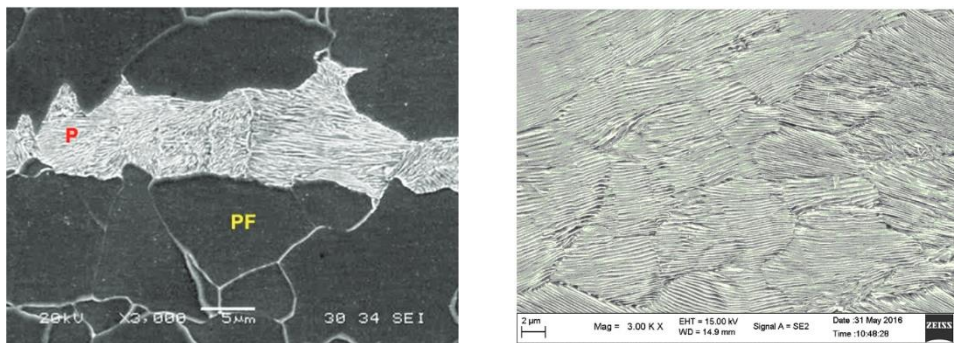
Figure 2 left: Pearlite (P) and polygonal ferrite (PF) in a X60 Steel [14], right: Pearlitic steel [15]

2.2.3. Ferrite

Alpha iron or ferrite, is one of four allotropes of iron and named after ferrum, the latin word stem for iron. α-Ferrite is formed by a FCC-BCC transformation from austenite. In steel, this transformation is both dependent on the cooling rate and the carbon content. While Austenite can absorb 2.14 wt.% carbon, the solubility of carbon in ferrite is only 0.022 wt.%. If carbon content of the steel exceeds this value pearlite is formed. If the cooling rate is too high martensite is formed. [10, 12, 13]

Depending on cooling rate and nucleate content different forms of ferrite can nucleate such as Widmanstätten ferrite, acicular ferrite, globular ferrite, polygonal ferrite, allotriomorphic ferrite and idiomorphic ferrite, which will be discussed below.

5

Widmanstätten ferrite

Named after Alois von Beckh Widmanstätten, Widmanstätten ferrite is a sawtooth or lath like form of ferrite, often resembling needles. It has a Kurdjumov Sachs relationship with the austenite grain [16]. The definition of Widmanstätten ferrite is not clear and closely linked to acicular ferrite. Some publications see Widmanstätten ferrite as a type of acicular ferrite, other do not, pointing towards acicular ferrite nucleating on nucleates, while Widmanstätten ferrite grows on grain boundaries, either prior to the formation of allotriomorphic ferrite directly or afterwards from allotriomorphic ferrite. Other authors define acicular ferrite as a type of intergranular Widmanstätten ferrite. [17 – 20]
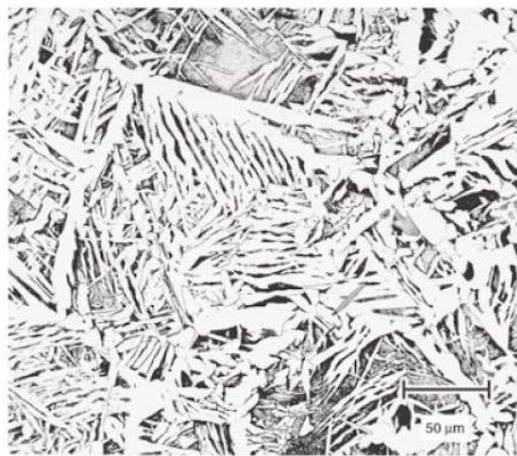
Figure 3 Widmanstätten ferrite [12]

Acicular ferrite

Acicular ferrite is a thin needle like form of ferrite, generally nucleated on a nonmetallic inclusion. The main defining factor of acicular ferrite is grains that impede each other and are pinned. Acicular ferrite can either be defined as intergranular Widmanstätten ferrite, a form of intergranular nucleated bainite or a mixture of intergranular idiomorphic ferrite, intergranular Widmanstätten ferrite and intergranular polygonal ferrite. Literature suggests that the main cause of acicular ferrite are additives such as titanium oxides, sulfur or silicon carbide which can both serve as a nucleation site and reduce the carbon content of the surrounding steel, promoting the formation of bainite and ferrite. [20 – 22]

6
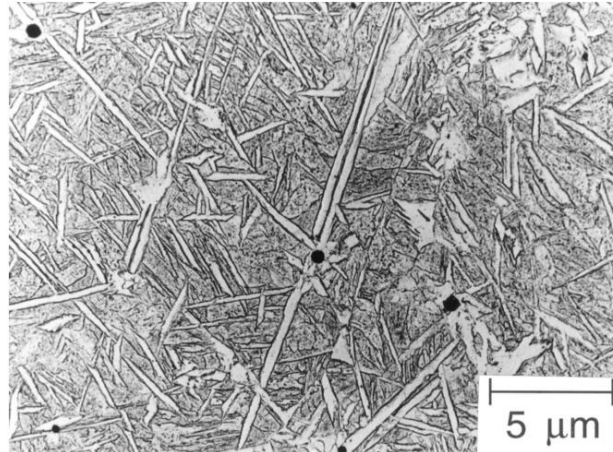
Figure 4 Replica transmission electron micrograph of acicular ferrite [21]

Globular ferrite

Globular ferrite is a form of ferrite that like acicular ferrite shows no form of orientation or substructures and is commonly found in form of globules. Literature suggests it is created as a result of metastable forms of ferrite such as acicular ferrite breaking apart. [23]
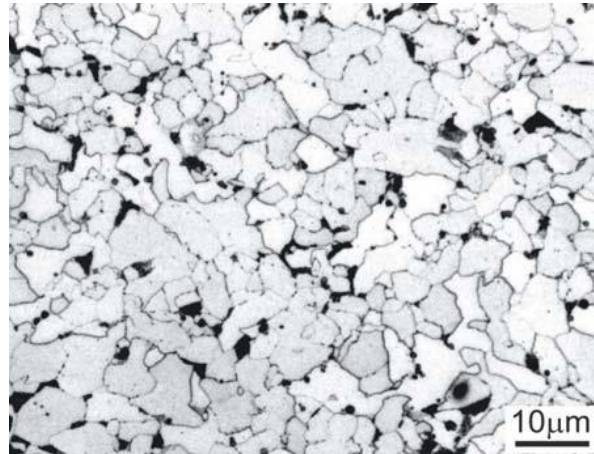
Figure 5 Ferritic microstructure (white) containing globular ferrite with grain boundary pearlite (black) [24]

Polygonal ferrite

Polygonal ferrite is a type of ferrite formed under high temperature at the grain boundary and grows to equiaxed grains. The main difference to globular ferrite is that the grain boundaries are linear and continuous. [25]

Figure 6 polygonal ferrite(light) and martensite (dark) [25]

Allotriomorphic and idiomorphic ferrite

The final two microstructures discussed in this section are allotriomorphic ferrite and idiomorphic ferrite, which are both a result of diffusional decomposition of austenite. Allotriomorphic ferrite starts at prior austenite grain boundaries, covers it and is typically the first decomposition product of austenite. Idiomorphic ferrite on the other hand tends to form around larger nucleates and is also known as intergranular ferrite. [26, 27]
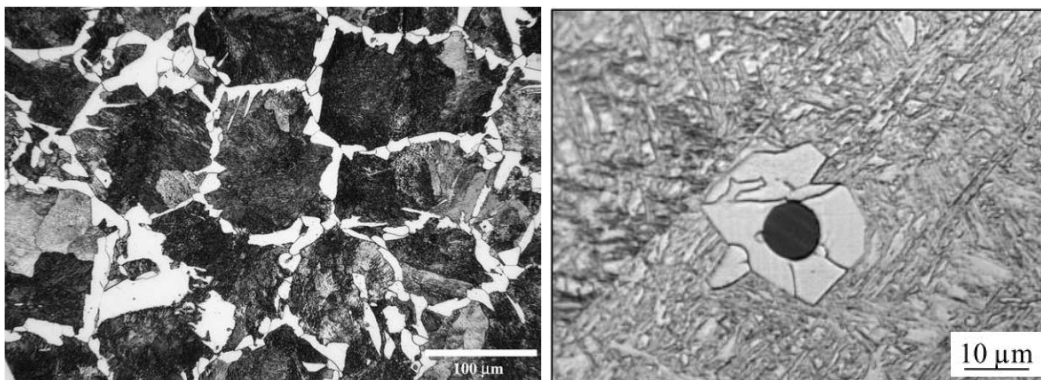
Figure 7 left: Allotriomorphic ferrite (white) surrounding pearlite (black) [28] right: Intergranular ferrite around large TiO$_2$ nucleate [29]

2.2.4. Bainite

Bainite, named after Edgar Collins Bain, is a microstructure in steel. Bainite appears as a combination of ferrite and a second, carbon richer microstructure, either austenite, cementite or martensite.

The bainitic ferrite forms 3 dimensionally connected plates, sub units, which in turn form wedge like plates called sheaves. The subunits have the morphology of either a lenticular plate or a lath. Bainite can be separated into upper and lower bainite which both differ in structure and formation temperature. Upper bainite is formed at higher temperatures, 350-500°C while lower

8

bainite is generally formed at lower temperatures. The main difference is that upper bainite has no carbide within the ferrite, while lower bainite has precipitates of carbides between the plates and carbide particles inside the bainite. Both have carbide between the ferrite layers. The morphology and size of the subunits and the dislocation density within the bainite can further refined using various methods. The bainitic ferrite in upper bainite shares a relationship with the austenitic grain which comes close to either the Kurdjumov Sachs (KS) or the Nishiyama Wassermann (NW) relationship. As for lower bainite it displays a twin relationship between the lathes and seems to show a near NW relationship. Furthermore, the transformation must occur within the Bain region, which means that during austenite to bainitic ferrite transformation, rotation of both the planes and the direction has to be 11° or less. Non bainitic, allotropic ferrite does not show this behavior, individual orientations may be with the Bain region or show near KS or NW orientation relationships but overall the orientation seems to be independent from the austenitic grains. [21]
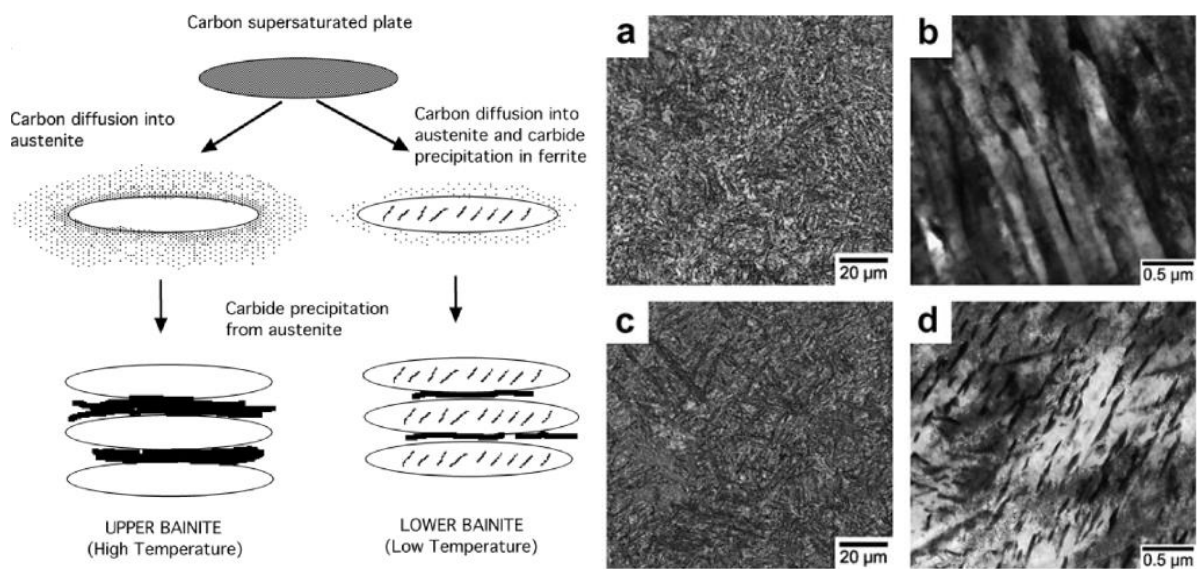
Figure 8 left: Mechanisms of Bainite transformations [21], right: Upper (a, b) and lower (c, d) bainite in electron microscope [30]
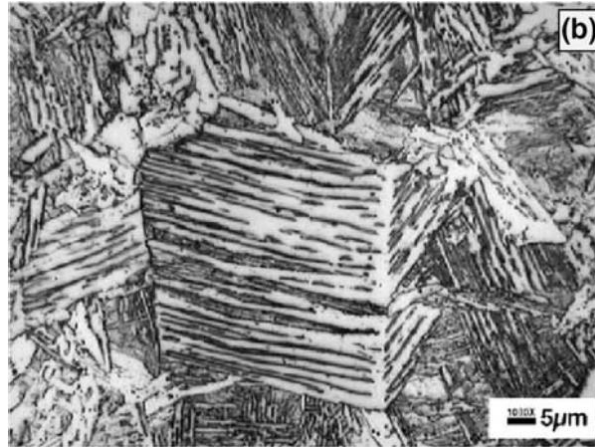
Figure 9 upper Bainite [27]

2.2.5. Martensite

Martensite, named after Adolf Martens, is a microstructure in steel. Martensite is created from carbon rich austenite by rapid cooling.

If the austenite is cooled too fast for the carbon to diffuse out of the crystal to form cementite, the crystal system is distorted, forming a highly strained body centered tetragonal structure that is supersaturated with carbon. This structure is known as martensite. This highly distorted structure increases the hardness of the steel but makes it more brittle. To reduce brittleness, strain and dislocations but also the hardness, the martensitic structure can be heat treated, which relaxes the structure, and decreases the martensite concentration. Since martensite is not an equilibrium structure, but a metastable structure, as it is formed by quenching, it is not shown on the iron carbon diagram. There are two main types of martensite, plate martensite and lath martensite. Lath martensite is formed between 0-0.6%C and plate martensite is formed at higher carbon concentrations. Due to the formation of carbide precipitates this transformation is irreversible. Martensite transformation starts at Ms, the martensitic start temperature; and needs a gradual cooling to be completed. Initial martensitic growth at Ms can be close to the speed of sound. [13, 31, 32]
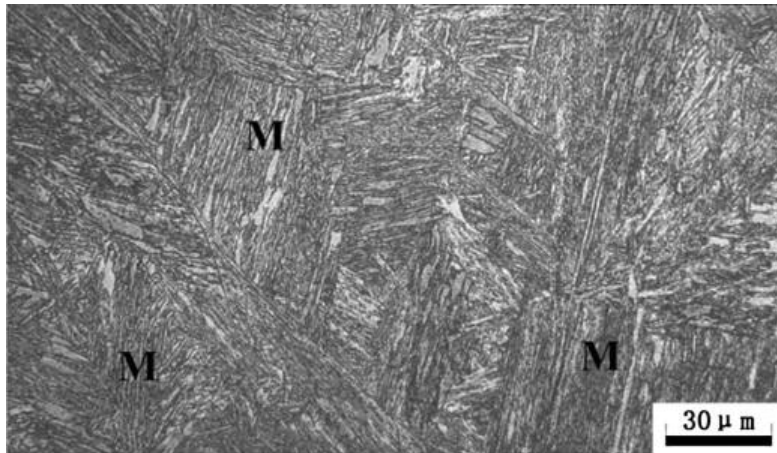
Figure 10 Martensite in the coarse grain heat affected zone of a HSLA steel joint [33]

2.3. Kurdjumov Sachs and Nishiyama Wassermann orientation relationship

The Kurdjumov Sachs (KS) and Nishiyama Wassermann (NW) orientation relationship are two of multiple possible orientational relationships between FCC and BCC crystal systems. Both KS and NW have in common that the close packed planes (111) FCC and (110) BCC are parallel. In the KS relationship however the [1-11] BCC direction and the [0-11] FCC direction are parallel, while in the NW relationship the [001] BCC and the [-101] FCC directions are parallel. A 5.26° rotation around the closed packed plane can transform the NW relationship into the KS and vice versa. [13] The KS and NW relationships play a large role in the BCC-FCC phase transformation of austenite into ferrite, bainite and martensite as all three have morphologies that are formed according either or both orientation relationships [20, 21, 31].

2.4. Influence of FSW on the Microstructure of Steel

FSW can change both microstructure and grain size of steel depending on welding parameters and microstructure of the steel:

Austenitic steel

FSW of 304 austenitic stainless steel causes the grain size to slightly decrease, increasing dislocations and sub-grains (see Figure 11). Additionally, fine grained ferrite forms along the austenite grain boundaries. The weld shows an increase in hardness after FSW. [34]

11
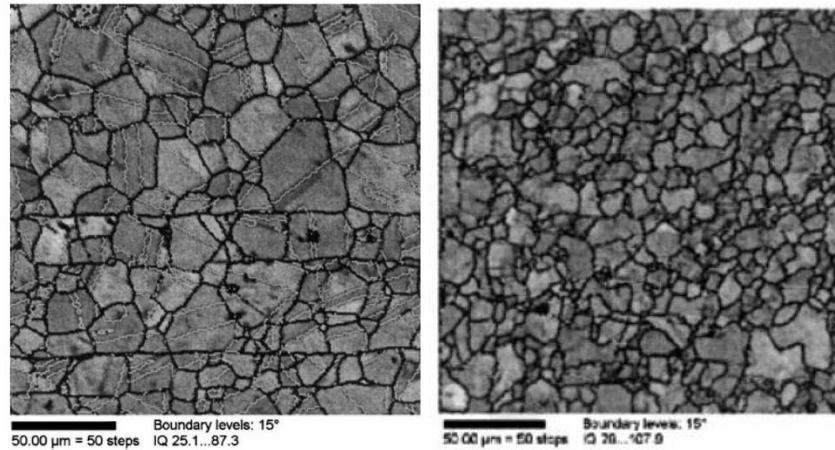
Figure 11 Orientation imaging microscopy (OIM) map of base material (left) and stir zone (right) in 304 austenitic steel [35]

Ferritic steel

In 409 ferritic stainless steel the stir zone undergoes dynamic recrystallization and results in ferrite grain refinement. This fine grained ferritic microstructure leads to an increase in hardness (see Figure 12). [35]
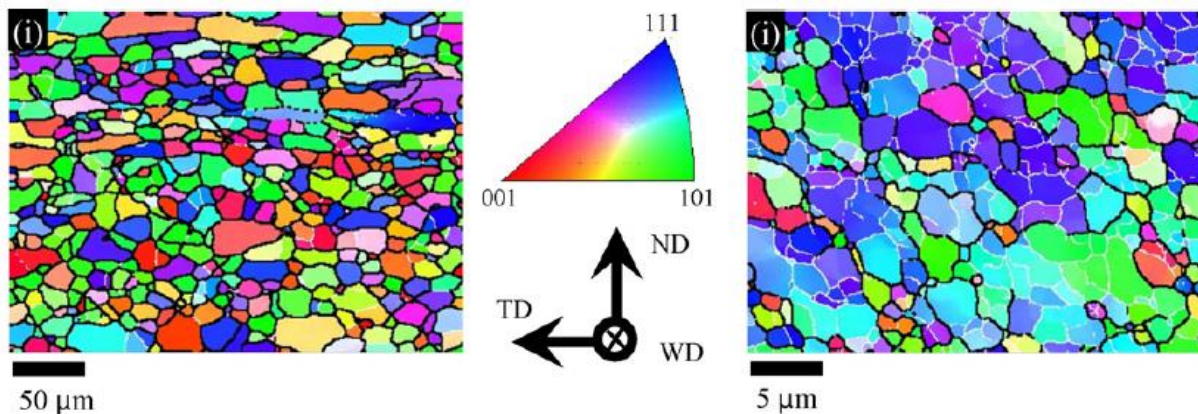
Figure 12 Orientation map of 409 ferritic steel base material (left) and stir zone (right) with different magnifications due to grain refinement by FSW [35]

In 409M ferritic steel, a derivate of 409 steel designed to allow partial transformation of ferrite to austenite, the microstructure changes from a coarse ferritic structure to a fine-grained duplex structure of ferrite and martensite (Figure 13). This results in an increase of both tensile strength and hardness. The formation of Fe_6W_6C from tool abrasion which formed precipitates in the sample on the other hand lead to a reduction in impact toughness and ductility. [36]
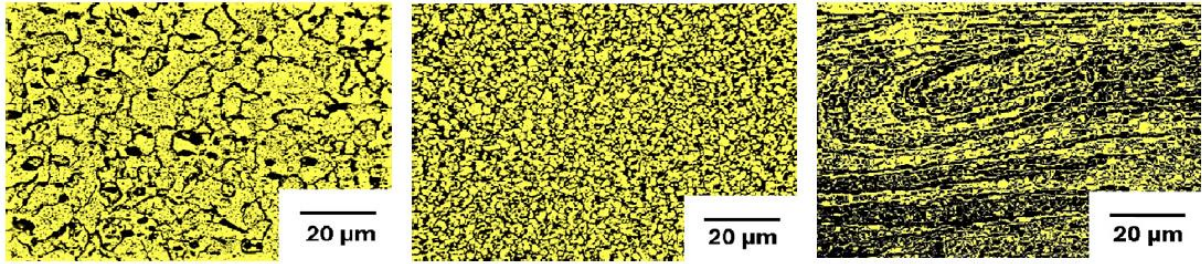
Figure 13 Microstructure of 409M ferritic steel base material(left), stir zone shoulder influenced zone(mid) and stir zone pin influenced zone(right) [36]

Martensitic steel

30Cr15Mo1N is a high nitrogen martensitic steel. The FSW process leads to a transformation of martensite to austenite with a loss in hardness but an increased corrosion resistance (see Figure 14). [37]
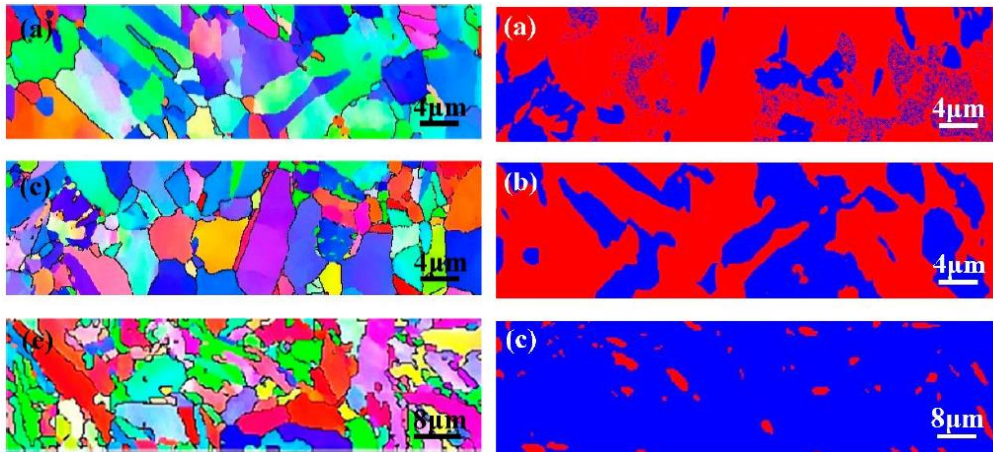
Figure 14 Grain boundary map (left) and austenite (red) to martensite (blue) distribution of base material (c), top of stir zone (a), bottom of stir zone(b) [37]

Dual Phase steels/Duplex steels

DP600 is a dual phase steel consisting of martensite islands in a ferrite matrix. FSW results in the formation of bainite, fine ferrite and ferrite-carbide aggregates in the nugget and heat affected zone (see Figure 15). Hardness is reduced due to the loss of martensite. [38]

13
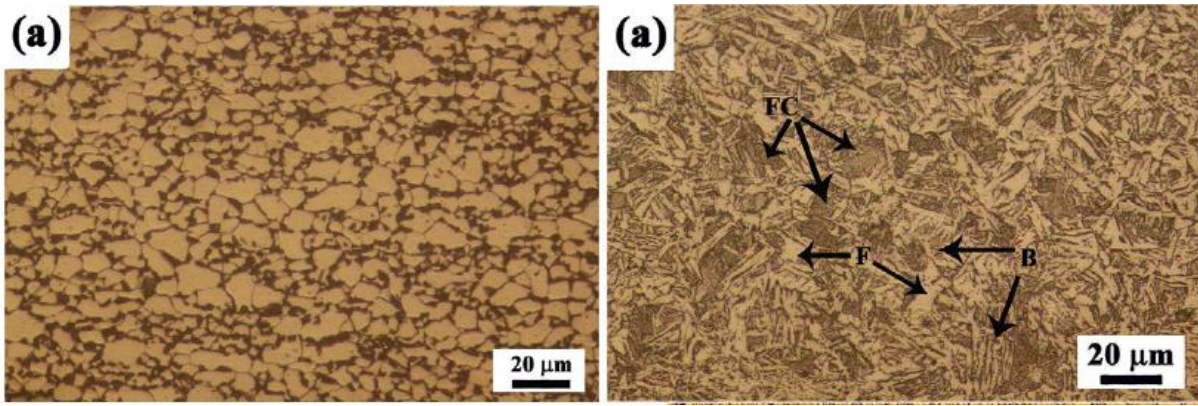
Figure 15 Microscopy image of base material (left) and stir zone (right) in DP600 dual phase steel F = Ferrite, FC = ferritic carbide B = Bainite [38]

SAF 2507 super duplex steels consists of a mixture of austenite and ferrite. FSW does not change the phases present but instead causes a grain refinement of both ferrite and austenite, leading to an increase in strength and hardness within the stir zone (see Figure 16). [39]
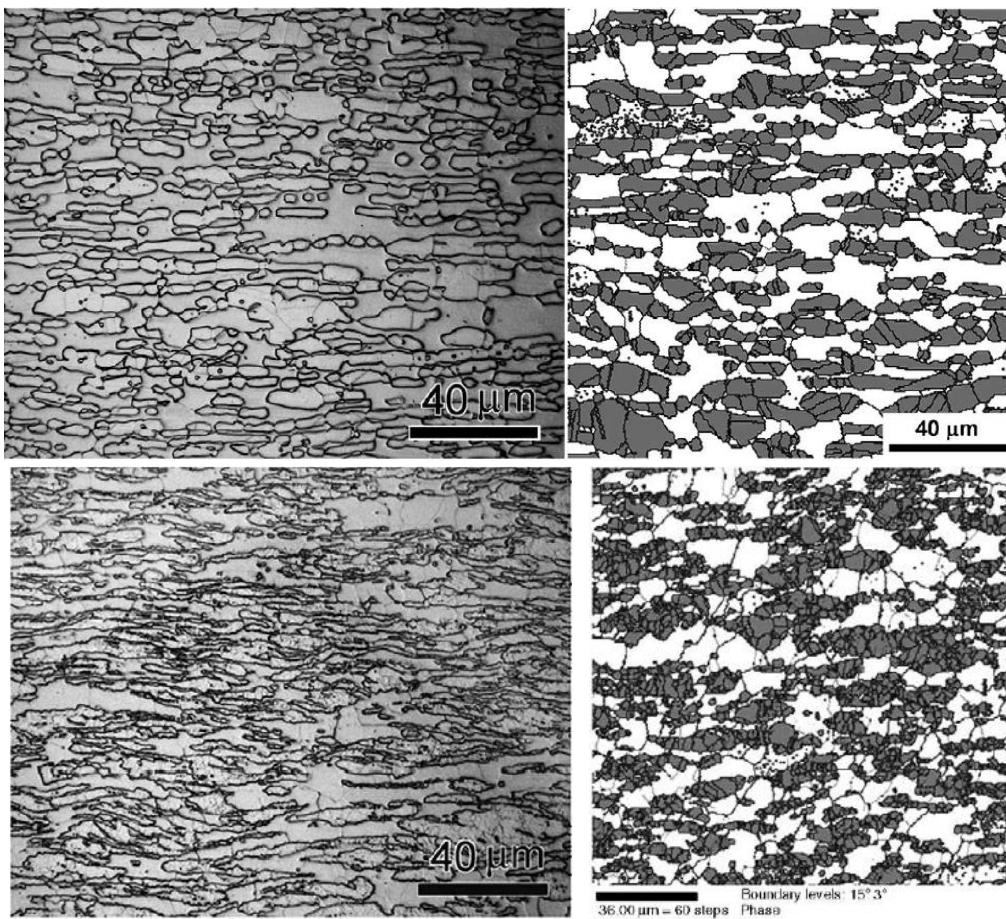
Figure 16 Microscopy image (left) and OIM phase map of base material (top) and stir zone (bottom) in SAF 2507 super duplex steel [39]

High strength low alloy steels (HSLA)

A588 Grade K HSLA steel is a steel made up of a polygonal ferrite and pearlite microstructure. After FSW the weld nugget consists primarily of upper bainite and fine-grained ferrite. Increasing the traversing speed leads to a decreased ratio of upper bainite due to the reduced heat input and higher cooling rate. Another consequence of higher traversing speeds is an increase in welding defects and a decreasing grain size (see Figure 17). Due to the changed microstructure the hardness of the steel increases after FSW but this increase is lost at higher speeds due to the defects and decrease of bainite. [40]
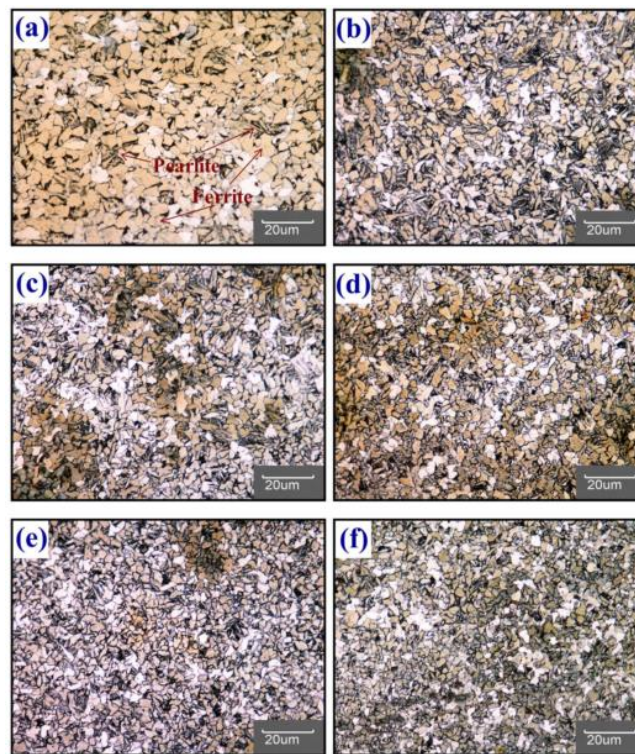
Figure 17 Microscopy image of A588 Grade K HSLA steel base material (a) and stir zone (b-f) with increasing traverse speeds from 57 mm/min (b) up to 97 mm/min (f) [39]

HSLA-65 is a steel consisting of upper bainite islands in a matrix of polygonal ferrite. The microstructure after welding depends on FSW heat input. At low heat input the microstructure is transformed into lath bainite. Higher heat input increases the formation of upper bainite and ferrite (see Figure 18). [41]

15
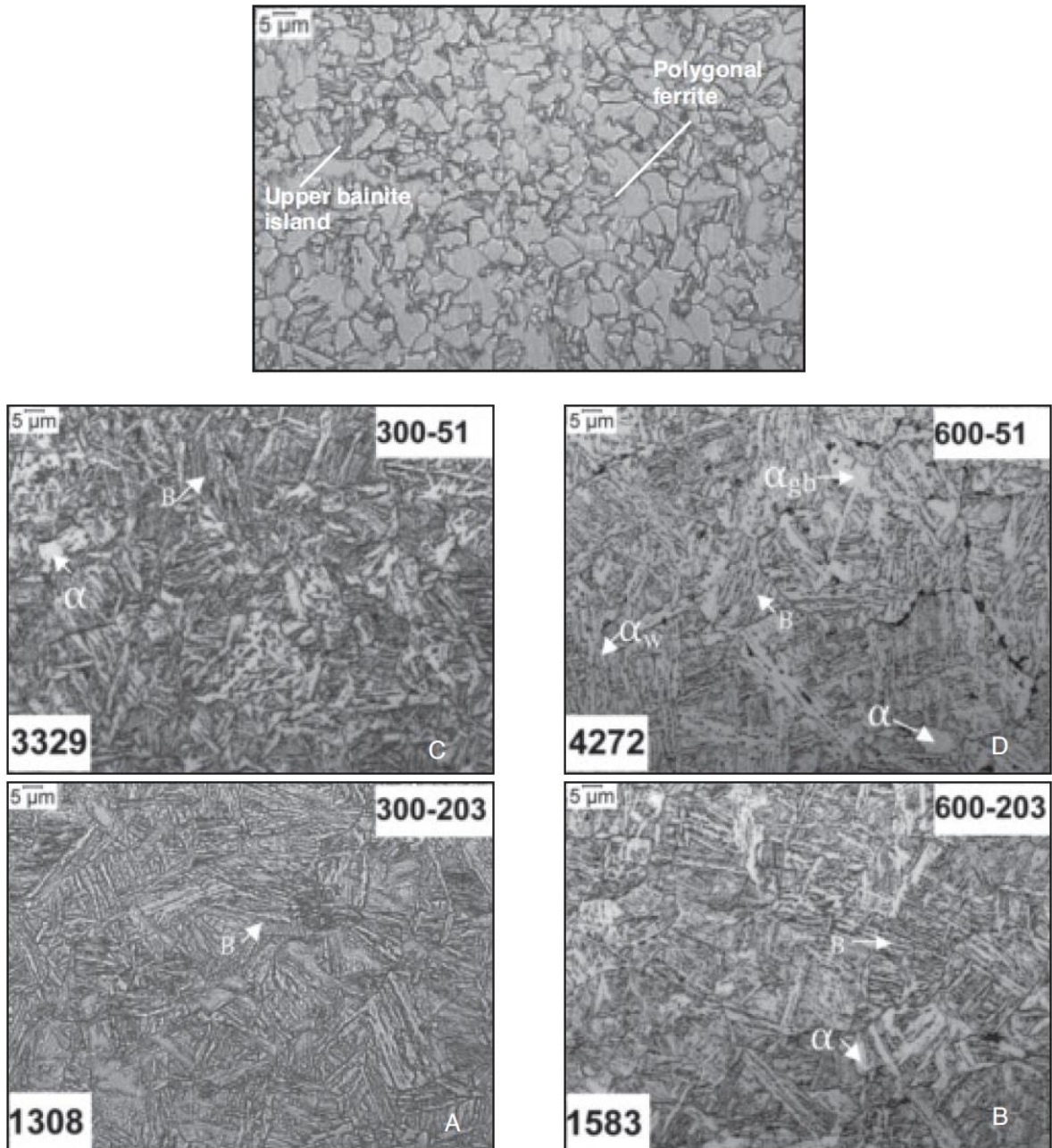
Figure 18 HSLA65 optical microscopy of base material (top center) and stir zone (below) at two different rotation speeds (300/600 rpm) and traversion speeds (51/203 mm/min) B = bainite, α = ferrite, gb = grain boundary, W = Widmanstätten [41]

High strength steels

S690 is a ferritic-bainitic steel with homogenously distributed precipitates. The Microstructure after FSW is similar to the base material but with larger, more randomly oriented grains and a lower density of precipitates (see Figure 19). [42]

16
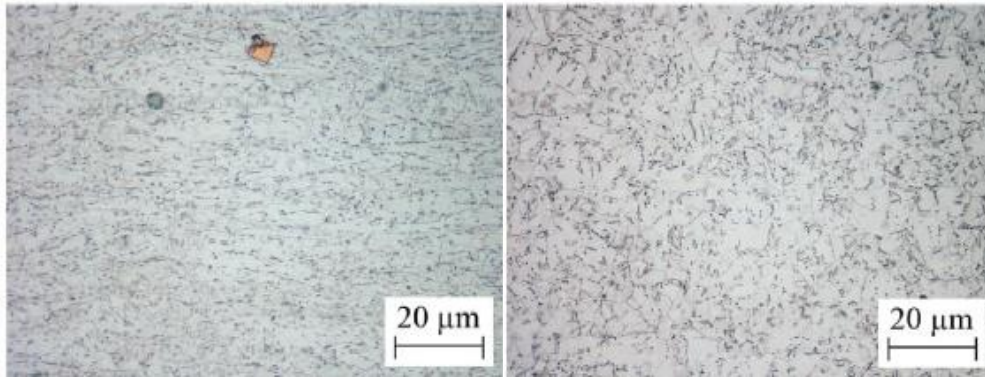
Figure 19 Optical microscopy of S690 steel base material (left) and stir zone (right) [42]

S355 is a steel with a polygonal ferrite microstructure containing pearlite islands. After FSW the microstructure is primarily lath bainite and acicular ferrite with larger grains (see Figure 20).

Both steels show an increase in fatigue strength, but the decreased density of precipitates in S690 decreases the hardness while the microstructural change in S355 increases hardness. [42]
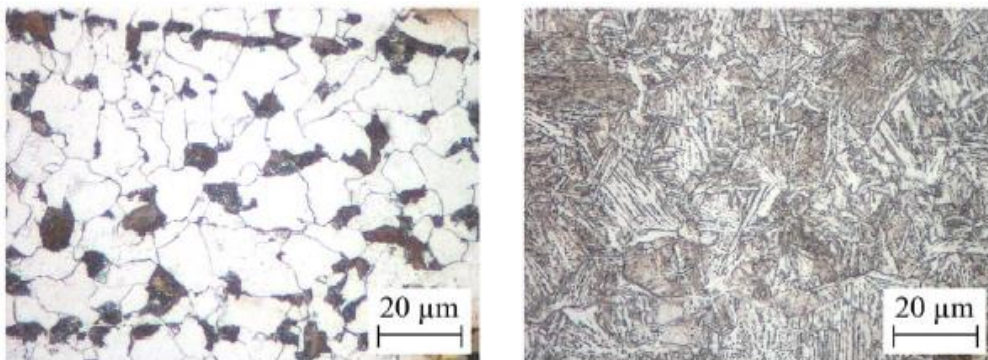
Figure 20 Optical microscopy of S355steel base material (left) and stir zone (right) [42]

Pipeline steels

X100 steel is made up of the two phases ferrite and bainite. During FSW the formation of acicular shaped bainite and fine grained, dynamically recrystallized ferrite in the stir zone occurs, increasing the hardness of the material (see Figure 22). The heat affected zone on the other hand experienced a grain size increase which lead to a decrease in hardness when compared to the base material. The thermomechanically affected zone shows a grain refinement due to dynamic recrystallization of ferrite. [43]
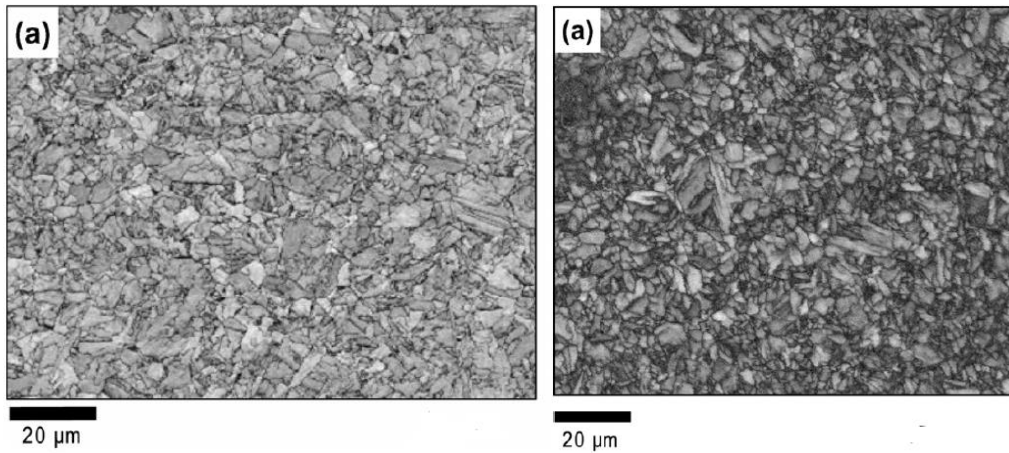
Figure 21 X100 steel base material (left) and stir zone (right) [44]

In X80 steel, which is made of ferrite, degenerated pearlite (DP) and martensite-austenite constituents (MA), the microstructure is shown to be dependent on the welding parameters (see Figure 21). At a speed to revolution ratio of 20 mm/revolution, the microstructure of the stir zone changes to degenerated upper bainite consisting of elongated MA, ferritic and an elevated cementite concentration, which reduces fracture toughness. 29 and 33 mm/revolution on the other hand produce massive MA, lower carbide content and higher fracture toughness. The heat affected zones of all 3 speed-revolution ratios show a mixture of massive MA and moderate levels of carbide and have an elevated fracture toughness. The grain size undergoes a refinement at 20 mm/revolution from 5 mm to 3mm but stays constant at 4mm for 29 and 33 mm/revolution. [44]
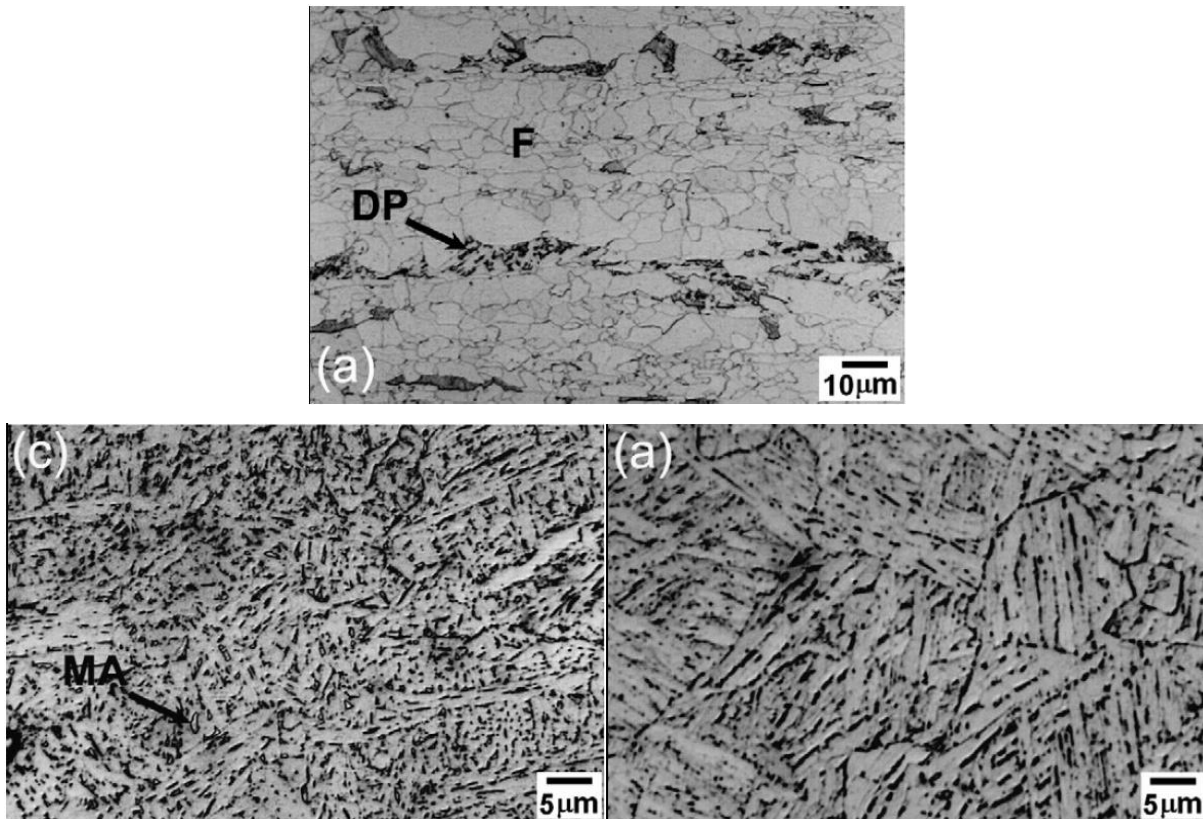
Figure 22 X80 steel optical microscopy of base material (top center) and stir zone (below) at 0.2 rev/mm (below left) and 0.29 rev/mm (below right) [43]

2.5. Titanium dioxide

Titanium dioxide is the natural oxide of titanium (IV) and the most important titanium product, as about 95% of all titanium ore is processed to TiO_2. Titanium dioxide has 4 natural polymorphs in addition to 3 metastable polymorphs and 3 high pressure polymorphs. The four natural polymorphs are rutile, anatase, brookite and TiO_2 (B). Under standard conditions rutile is the most stable microscopic polymorph of TiO_2 while anatase becomes the most stable polymorph when the grain size is reduced to the nanoscale. At standard conditions but at a temperature of 500°C and above, anatase transforms into rutile permanently. The titanium ores used primarily for the production TiO_2 are ilmenite and rutile. Ilmenite can be transformed to pure TiO_2 via sulfate process, involving treatment with sulfuric acid to remove the iron. Both rutile and ilmenite can also be treated via the chloride process, in which TiO_2 is deoxidized with carbon, chlorinated to $TiCl_4$ and reoxidized back to TiO_2 to remove all impurities up to a certain degree. TiO_2 is mainly used as a pigment, due to its white color and high refractive index, mostly as paint but also in glazes, plastics, food and cosmetics as it is deemed as safe for consumption. Nanocrystalline TiO_2 is a semiconductor, absorbs UV light and is a photocatalyst. It is mostly used as sunscreen as titanium dioxide nanopowder and zinc oxide nanopowder are

19

the only 2 non organic compounds on the "*list of UV filters allowed in cosmetic products*" of the European Union. [45 – 48]
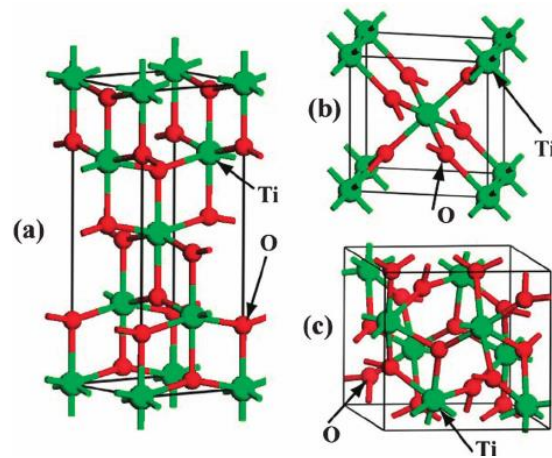
Figure 23 Structure of Anatase(a), Rutile (b) and Brookite(c), green Titanium, red Oxygen [49]

2.5.1. Influence of TiO_2 particles on the microstructure of Steel

As briefly touched upon before the presence of titanium dioxide can induce the formation of acicular ferrite. This is primarily due to two different factors, the nucleation site and the reduction of carbon content. TiO_2 can decarburize the surrounding steel, which favors the growth of both bainite and ferrite and in turn enables the growth of acicular ferrite [21, 50]. TiO_2 also has a low lattice mismatch to FCC iron of around 9% which allows TiO_2 particles to be a nucleation site for acicular ferrite [21, 51].

Furthermore, oxides such as TiO_2 are known to induce recrystallization in steel which leads to the formation of intergranular ferrite around the particle, with larger particle sizes inducing intergranular ferrite, rather than acicular ferrite [52, 53]. Finely distributed TiO_2 particles can also reduce the growth of austenite grains via the Zener pinning effect resulting in a finer microstructure [50, 54].

According to literature an oxide content of 200-300 ppm and nucleate grain size of 0.3-0.9μm are ideal for acicular ferrite formation, while a grain sizes of 2 micron and above induce formation of intergranular ferrite instead [29, 55–57].

2.6. Methods for Microstructure investigation

2.6.1. Optical microscopy

 A light microscope (LOM) is designed to create a magnified image of an object via the use of a light source and lenses. Light is focused on a small area of the surface of a sample, diffracted,

bundled by 2 magnifying lenses and then viewed either by eye or on a screen [58]. Standard microscopes reach their limit at about 1000 times magnification, with magnifications as high as 4900 times reported [59, 60]. The theoretical resolution of optical microscopy is limited by the wavelength of the light and of light but several methods have been developed to circumvent this limit and achieve a resolution of up to 20 nm [61].

2.6.2. Scanning electron microscopy

Scanning electron microscopy (SEM) uses electrons to form highly magnified images, diffraction patterns or elemental mapping of a sample. Analogue to LOM SEM particles are emitted from a source, bundled by lenses, hit a surface and the diffracted/emitted particles are detected. Unlike optical microscopy the particles are electrons, the lenses are magnetic lenses, the types of detectable particles and detectable information about the sample are more extensive and the detectors are different, see Figure 24. The detectable electrons are secondary electrons (SE) and back scattered electrons (BSE) as wells as Auger and transmitted electrons for special electron microscopy methods. Additionally, X-rays which are emitted from the sample and Bremsstrahlung can also be detected, see Figure 25. The detection limits of optical microscopy do not apply to electron microscopy and with the use of special methods such as using high-resolution transmission electron microscopy (HRTEM) even singular atoms can be resolved. [62] The SEM used in this thesis had a magnification limit of 1 million times. The following sections will focus on the 3 main methods used in course of the experimental work in this thesis.
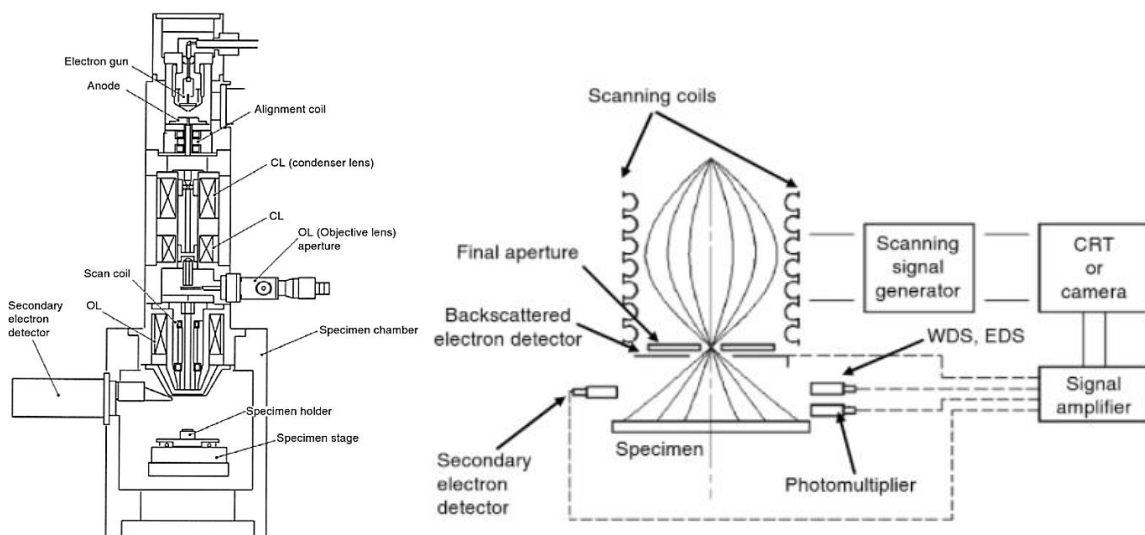
Figure 24 left: General setup of SEM [63] right: SEM sample region and detectors [63]
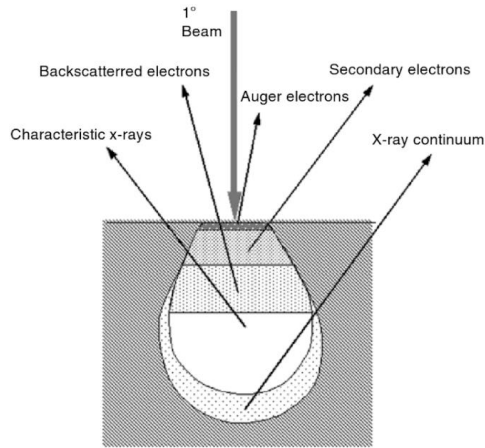
Figure 25 SEM beam and types of detectable particles [63]

2.6.2.1. SEM

Scanning electron microscopy or SEM is one the main setups for electron microscopy. The electron beam which impacts at the specimen surface is transformed to an image of a very small area and scanning coils move the beam along the chosen area to form the larger image viewed. The main mode of SEM is secondary electron imaging in which the electron beam excites the atoms of the sample which in turn emit secondary electrons that are detected by the secondary electron detector such as the Everhart-Thornley detector. Electrons that are backscattered from the areas beneath the surface can also be detected via special detectors (Figure 25). The secondary electrons deliver mainly information about near-surface areas such as topography and surface roughness while backscattered electrons deliver information about areas beneath the surface. [63]

2.6.2.2. EDS

Energy-dispersive X-ray spectroscopy or EDS is an elemental analysis method that uses X-rays emitted from the sample surface to detect the composition of the sample. The electrons of the atomic orbits of the samples are exited, reach an orbit, and emit characteristic X-rays when falling back to the lower energy orbit. These are detected by an X-ray detector. The resulting spectra is element specific as the X-rays emitted are characteristic for each element. Hence every element has a distinct pattern of lines in the spectra which allows the composition of the sample to be estimated. [64]

2.6.2.3. EBSD

EBSD or electron backscatter diffraction is an analysis method in electron microscopy used to obtain crystallographic information about the sample. A small number of electrons from the primary electron beam are backscattered and those exiting at the right angles cause diffraction, which in turn results in a diffraction pattern, which is defined by the lattice parameters of the crystal. Using this pattern crystallographic orientations of grains and sub grains can be determined. [63, 65]

2.6.3. Laser scanning confocal microscopy

A laser scanning confocal microscope (LSCM) uses a laser beam instead of white or polarized light or electrons for the magnification of the sample. Both, the method and the magnification of the LSCM lies in-between a light microscope and a SEM as the microscope uses photons in form of a laser but scans the surface like an SEM to form the image. The higher magnification and better resolution origins in the pin hole which eliminates out-of-focus light and greatly increases axial resolution. A half-mirror scans the surface of the surface and reflects the signal into the detector (see Figure 26). [66, 67] Additionally as seen in Figure 26 the setup can include a heating/cooling unit to enable in situ observation of microstructure formation and change. [68]
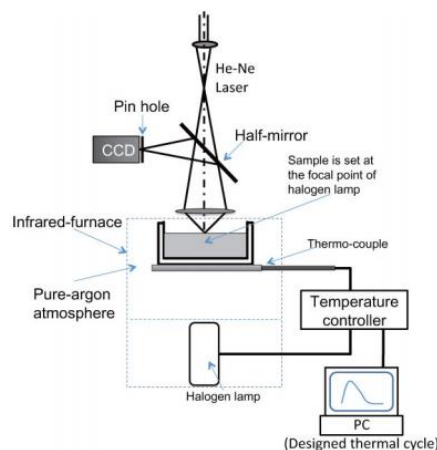

Figure 26 Setup of a heated LSCM system [68]

2.7.   Friction stir welding

Friction stir welding is a solid state joining method patented by The Welding Institute, UK in 1991 [69]. It is primarily used for joining metal alloy parts made of aluminum, titanium and to a lesser extent steel.

FSW tool

The FSW setup is that of a motor driving a rotating tool, which is cylindrical and has a smaller pin, which penetrates the material. The welding heat is mainly produced by the friction of the shoulder on the specimen surface. The shape of the pin and shoulder can differ depending on welding method, welding material, type of weld and material thickness. (Figure 27)
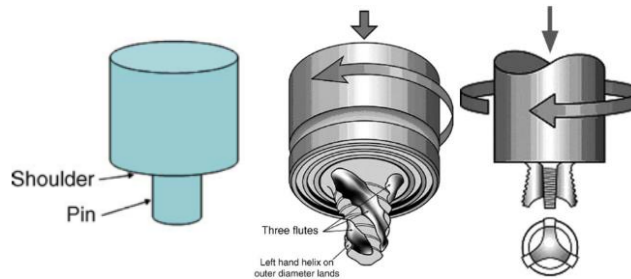
Figure 27 Schematics of a standard tool (left) [70] and two specialized tools (mid, right) [71]

Welding

There are two main ways to weld two plates together via friction stir welding, the butt weld and the overlap weld, also known as friction stir lap welding (FSLW) [72].

The tool is rotated and the pin is pressed into the material whereas the shoulder causing friction at the surface necessary for to heat and thus soften the material. Friction induced heat due to the tool rotation causes the material to flow plastically and is stirred by the pin. This destroys the original interface, creating a new bonded surface which joins both surfaces.

The material itself is only heated up to 80% of the melting temperature, which means that there is no solid-liquid-solid phase transition involved during heating and cooling, which in turn leads to different properties of the welding area compared to conventional welding.

The main advantages of friction stir welding when comparing it to conventional welding methods include speed, lack of filler, lack of preparation for welding, improved mechanical properties, lack of residual stress, good reproducibility and consistency, no pollution with welding fumes, automatability, no solid-liquid transitions.

Nevertheless, there are a few disadvantages to FSW, including an asymmetrical weld, a hole at the end of the weld, needs to be removed, high (axial) forces, less flexibility and less complex shapes welds possible. Additionally, a strong clamping and fixation of the welded parts are necessary.

Applications include welding the tanks of rockets, parts of newer car models and components in the aerospace industry.

When looking at the weld it can primarily be separated in halves. The half in welding direction

is called the advancing site while the second half is called the retreating site. Material generally flows from the retreating site in the advancing site in rotation direction. (Figure 28) The weld itself can be further distinguished in nugget zone, thermomechanically affected zone and heat affected zone. The nugget zone is the part of the weld in which the pin has been plunged in and the surrounding area. This area has been heavily deformed and affected by the friction heat, leading to dynamic recrystallization and thus to a fine grain zone. The thermomechanically affected zone TMAZ, is an area affected by the FSW tool and the friction heat but not as heavily as the nugget zone. The heat affected zone HAZ, has not been affected by deformation but experiences a thermal cycle, which can change the microstructure and mechanical properties. Outside of the HAZ the unaffected base material appears. Its microstructure has not been altered by deformation or temperature and is therefore identical to the unwelded sample in terms of mechanical properties and microstructure. [71, 73–75]
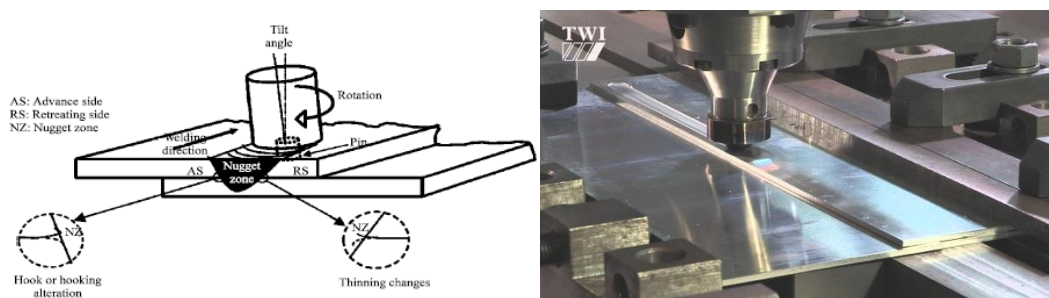
Figure 28 Schematics (left) [76] and picture(right) [77] of a FSLW setup
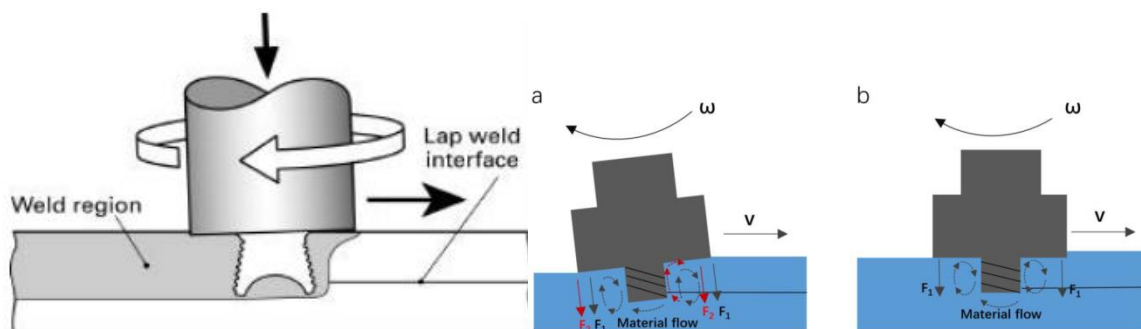
Figure 29 Side view of a FSLW process [72, 78]

2.8. Hot pressing

Hot pressing is a method for the sintering of ceramic particles, first proposed during the early 20th century with first process details emerging in 1930 [79]. The main setup consists of two punches or tools which compact material heated by heating elements and thereby sintering them, see Figure 30 Temperatures up to 2400°C and 50MPa pressure can be achieved [80]. The

same setup can however be used for thermomechanical deformation simulation in machines such as the Thermecmaster-Z, which is used in this thesis and the Gleeble [81, 82].
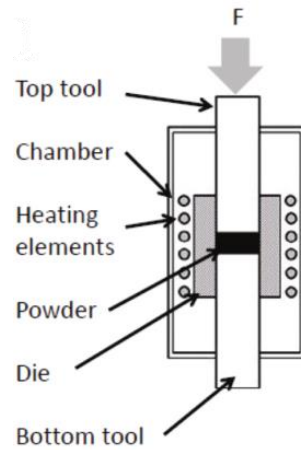
Figure 30 Pressing setup similar to the one used in this thesis [80]

Thermecmaster-Z

The Thermecmaster-Z uses inductive heating and either helium, N_2 or water as coolant for temperature cycles. It can achieve temperatures of up to 1600°C at a rate of up to 1400°C/s and cooling rates of up to 300°C/s when using water as coolant or 60°C/s with helium as coolant. The maximum load applicable is 100kN. [83]

3. Experimental section

3.1.   Friction stir welding [1]

3.1.1. Base material

The steel used in this thesis is an API5l grade X70 steel as described in the literature section. The composition of the X70 steel can be seen in Table 1and the measurements of the plate used in Figure 31 but it has to be noted that both width and thickness of the plates varied depending on the sample with the plate thickness varying between 2 and 4 mm.

Table 1 Composition of the investigated X70 steel [1]

Elements	C	Si	Mn	Ni	Mo	S	P	Cr	Nb	Ti	V
%wt.	0.081	0.167	1.43	0.35	0.063	0.003	0.009	0.15	0.021	0.013	0.055
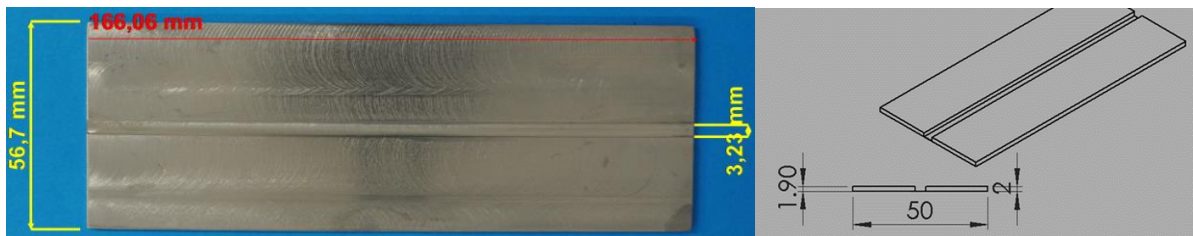
Figure 31Measurement X70 steel plate with groove(left) and approximate dimensions of groove and plate in mm(right)

The TiO_2 used can be separated into two different powders, anatase nanopowder and rutile micropowder.

The anatase micropowder is from Tecnan nanomat, Spain with a purity of 99.986% and a grain size of 10-15 nanometer.

The rutile micropowder from AMA Industrial Company, Tehran, see Figure 32, has a composition as seen in Table 2 and a grain size between 63 and 90 micrometers.

Table 2 Composition of TiO_2 micropowder [1]

Elements	C	Si	Fe	P	S	V	Zr	Ti
%wt.	0.022	2.5	0.68	0.011	0.022	0.52	0.68	94

Figure 32 TiO$_2$ micro powder

A WC-Co tool BB10 with a shoulder diameter of 19 mm, and a tapered probe with 3.7 mm length was used. The tool is shown in Figure 33.
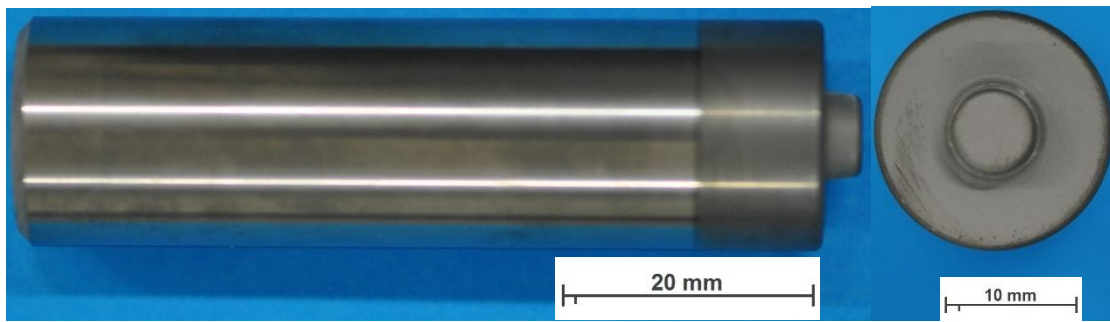
Figure 33 WC tool

The tool is made by Böhlerit, Kapfenberg composed of WC embedded in a Cobalt matrix with a weight ratio of 92% WC and 8% Co [74] and was replaced after each plate. The selected spindle speed is 600 rpm and the welding speed is 30 mm/min. The tool was tilted 2.5° against welding direction.

3.1.2. Process overview and sample parameters

The samples A-F were created by lap welding, whereas two plates were put on each other and the powder filled in a grove was distributed by FSW in the stir zone.

As seen in Figure 34 and Figure 35 the samples were created by lap welding 2 metal plates via friction stir welding. The bottom plate contained, except for sample A, a groove which, was either unfilled, filled with TiO$_2$ or with a ball milled mixture of TiO$_2$ and X70. After filling the groove of the bottom plate (step 3), a flat plate was put on the former (step 4), turned around (step 5) and FSW applied (step 6) with multiple samples per plate, up to six.
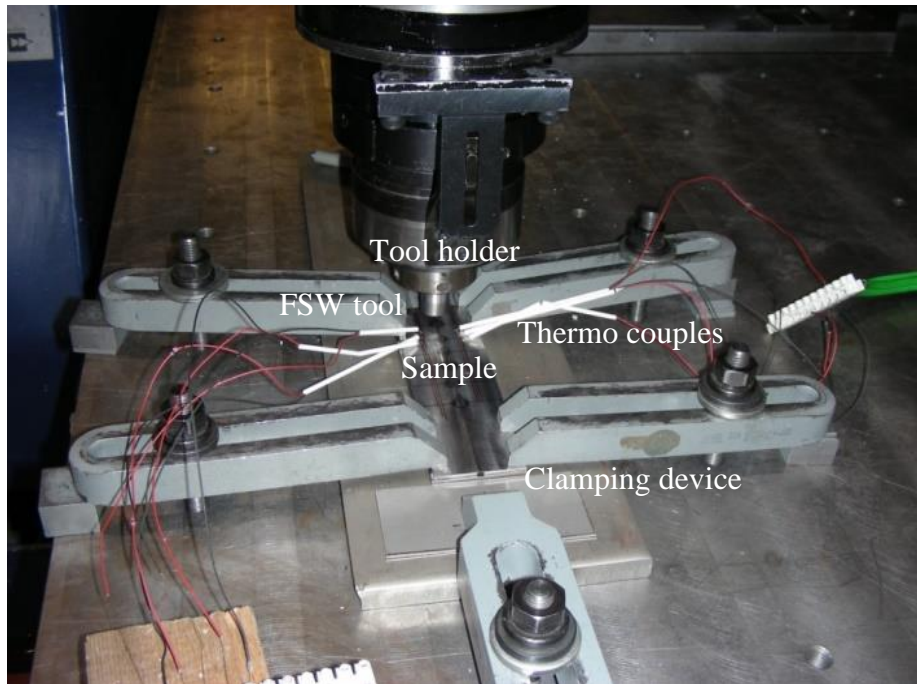
Figure 34 Experimental setup for the FSW process using the MTS ISTIR BR4 friction stir welding machine
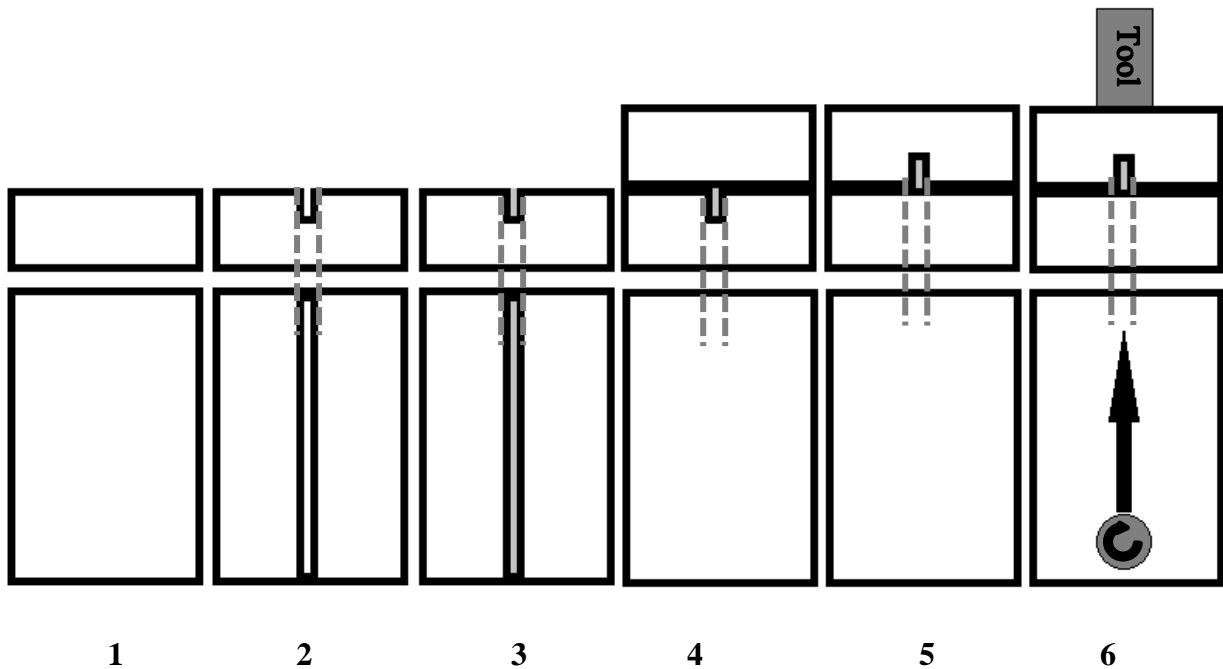
Figure 35 The welding process in 6 steps with side- (above) and top view (below): 1. Bottom sheet 2. Bottom with groove cut in 3. Groove filled with TiO_2 or $TiO_2/X70$ powder 4. Top plate added 5. Turning the plates around 6. Clamping and welding

In Figure 36 the thermal welding cycles at the advancing side (AS) and the retreating side (RS) is shown. They were measured using thermo couples, fixed 11mm away from the FSW center.
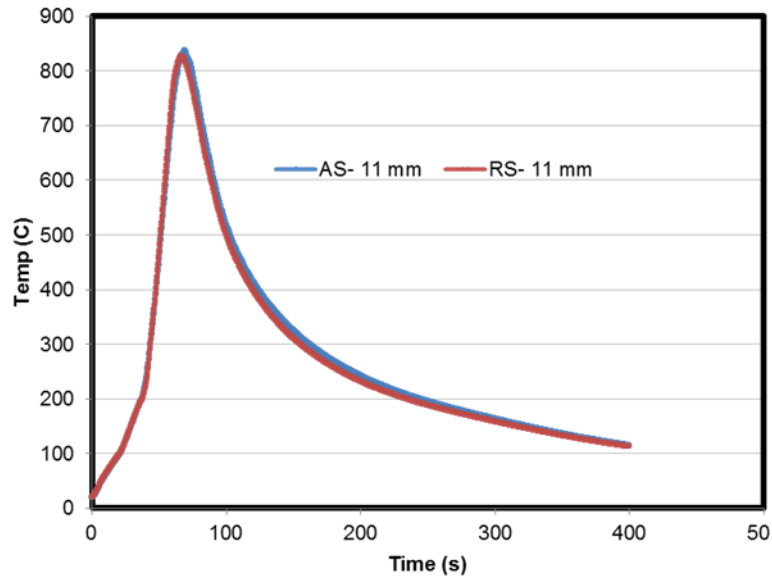
Figure 36 Temperature curve of the welding process measured 11mm from the center of the plate for advancing site (AS) and retreating site (RS)

3.1.3. FSW manufacture of samples A-E

Sample A was the reference sample, hence it had no additives or groove. The groove of sample B was filled with 0.02% Nano TiO_2, with "0.02%" being 0.02% of the mass of the steel removed while creating the groove or 0.02 percent of the density of iron multiplied with the volume of the groove.

Sample C was filled with a mixture of 99.94% steel powder and 0.06% TiO_2 micro powder. Sample D had just an empty groove, as it was at the end of a plate containing five other samples with varying amount of TiO_2 micro powder and it is assumed that the TiO_2 powder is partly transferred from one sample to the next by the FSW process and finally into Sample D as this plate was created in one continuous weld. The other samples on the same plate as sample D were not available for analysis.

The main difference of Sample D and the other samples is that the other samples only had 3 samples per weld, with each sample welded separately and of which only the first sample was analyzed (see Figure 38 for a side by side comparison of sample D and E).

Sample E was filled with a mixture of 99.98% steel powder and 0.02% TiO_2 Nano powder. Table 3 shows the composition of the samples and a summary of the welding parameter for all FSW samples chosen for analysis can be seen in Table 4.

Additionally, sample F, a hot-pressing sample was chosen for a LOM analysis, see next chapter.

30

Table 3 Summary of sample composition and welding parameters for FSW samples

Sample name	TiO_2 content in %	Type of TiO_2 powder	Steel powder in %
A	0	-	0
B	0.02	Nano	0
C	0.06	Micro	99.94
D	"0"	"Micro"	"0"
E	0.02	Nano	99.98

Table 4 Welding parameters

rpm	mm/min	Z-Force [kN]	Tilt angle
600	30	25	2.5°

Figure 37 FSW samples E (left, labeled 212a) and D (right, labeled 0)

3.2. Hot pressing

For pressing, 4x4x4mm cubes were cut out of the base material section of an unused sample, then further cut in half. Between both parts a small amount of micro TiO_2 powder was added and sheets of carbon and silica were attached on both ends to prevent contact with the pressing cylinder similar to the setup in Figure 38 . Afterwards the sample parts were fused using hot pressing, see Figure 39. The sample was heated to 1200 degrees Celsius, then held for 120 seconds while a load maximum of 4 kN was steadily applied to the sample during this time to create a diffusion weld between the halves. Afterwards the sample was cooled down while the load was removed and then a temperature curve resembling the FSW welding cycle from Figure 36 was applied.
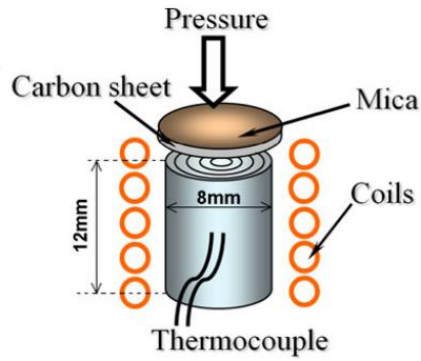
Figure 38 Hot pressing setup similar to the one used in this thesis [81]

Figure 39 Thermecmaster Z (left) [81] and pressing process (right) similar to the one used in the thesis [84]

3.3. Sample preparation and analysis

The samples were taken over from a previous investigation [1], hence they were re-polished using an automatic polishing machine etched with a 2% Nital solution and investigated. As the resin was nonconductive and too large for the SEM, the sample preparation had to be changed while working at the Koseki-Inoue Lab. The samples were re-embedded in a conductive resin, grinded, polished with a 1 micrometer polishing suspension of aluminum oxide or a diamond polishing spray and then etched with a 2% Nital solution. The samples were analyzed via light optical microscopy, electron microscopy, EDS and EBSD. The TiO_2 micro powder (Figure 32) was further analyzed via XRD by the Institute of Electron Microscopy and Nanoanalysis (FELMI) at Graz University of Technology to determine the exact phase and impurities.

4. Results and Discussion

4.1. WC tool abrasion

During the FSW process the tool was under constant pressure (force controlled mode) and rotation speed. Due to the high temperature by friction of the shoulder and the abrasive load of the material and the TiO_2 particles on the pin, the tool suffered severe wear. The pin was strongly worn out and the shoulder was broadened. This means that the worn-out tool material WC-Co was incorporated in the microstructure of the steel.

Figure 40 Tool wear during the welding process: initial (left) after 160mm (middle) after one plate (right)

4.2. Overview samples A-E and center of the weld

Figure 41 shows a macroscopic overview of samples A-E. A clear separation of the heat affected zone and the base material is present in form of a gray semicircle. The heat affected zones of sample B and C seem to go nearly to the bottom of the sample while the other samples show a shallower HAZ. The darker area at the top of the sample is WC tool residue, which can also be found within the center of the weld zone in sample B, C and E. The WC abrasions can be seen in Figure 42 as gold colored areas, while TiO_2 shows a gray-blue coloring.
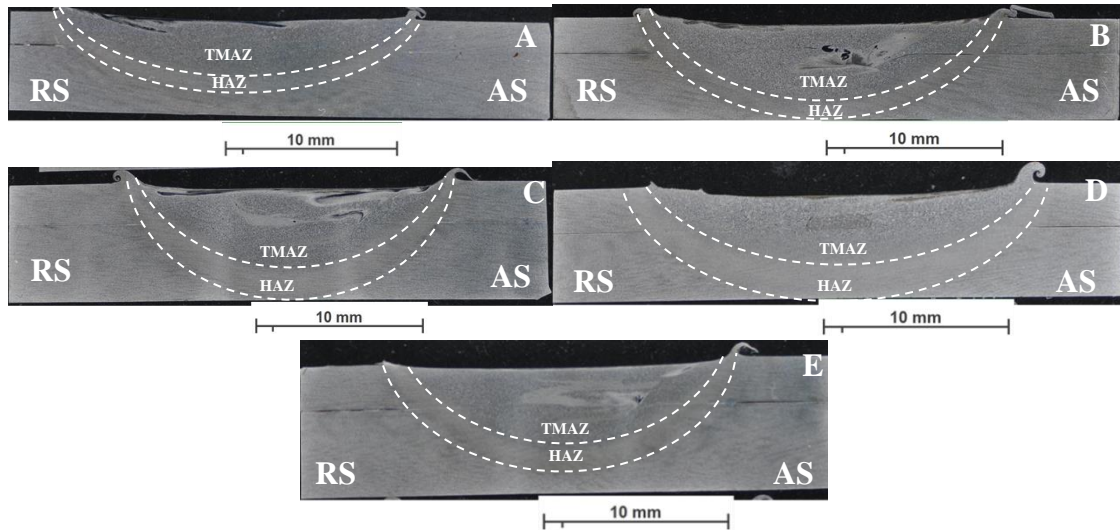
Figure 41 Macroscopic overview of the weld for samples A-E (see red letters)

Figure 42 Colored images showing the weld area of sample B (top left), C (top right) and E (below) gold is WC, grey TiO$_2$

4.3. Microstructural investigation

4.3.1. Sample A (reference, no groove, no TiO$_2$)

The surface of the sample close to WC abrasion shows a finer, more dendritic microstructure (see Figure 43①), which can be either attributed to a chemical effect of the WC, WC particles acting as a nucleation site, the cobalt content of the tool abrasion (see 4.3.8) or even due to the higher plastic deformation rate in the region, which causes the WC abrasion.

The center and lower center of the sample shows a primarily ferritic or bainitic microstructure with the particle size being larger than in other regions (see Figure 43②③). This seems to be a recrystallization effect as friction stir welding temperatures can reach up to 80% of the melting point at the center of the weld and high plastic deformation is present in the nugget zone and TMAZ. The base material of the weld located outside the HAZ shows a ferritic microstructure with grain sizes smaller than within the weld (see Figure 43④). EBSD was performed on the

center right of the sample, which shows the same microstructure as the mid center (see Figure 43⑤) as a reference to the EBSD analysis of sample B (see next chapter).

Figure 43 Sample A - LOM microstructure details: ① near surface close to WC abrasion, ② stir zone center and ③ below center, ④ base material outside HAZ and ⑤ center right (AS)

When looking at the EBSD results of the center right of the nugget zone (Figure 44), a major conclusion can be drawn: 1), the grains of sample A show a preference towards certain orientations. 2), when separating the area into prior austenite grains, 5 grains can be found, each of which corresponding with a Kurdjumov Sachs orientation relationship (see page 78 Figure 69). Taking this into account the ferrite can be identified as the ferrite of upper bainite which shows preferred orientations which are in a near Kurdjumov Sachs orientation with the austenite grain. This could also apply to martensite but the LOM images do not show martensite laths or plates and the slow cooling rate of the steel and low carbon content make martensite formation unlikely. The grain size in this region is large compared to the base material with most of the area occupied with grains of a diameter larger than 10 microns.
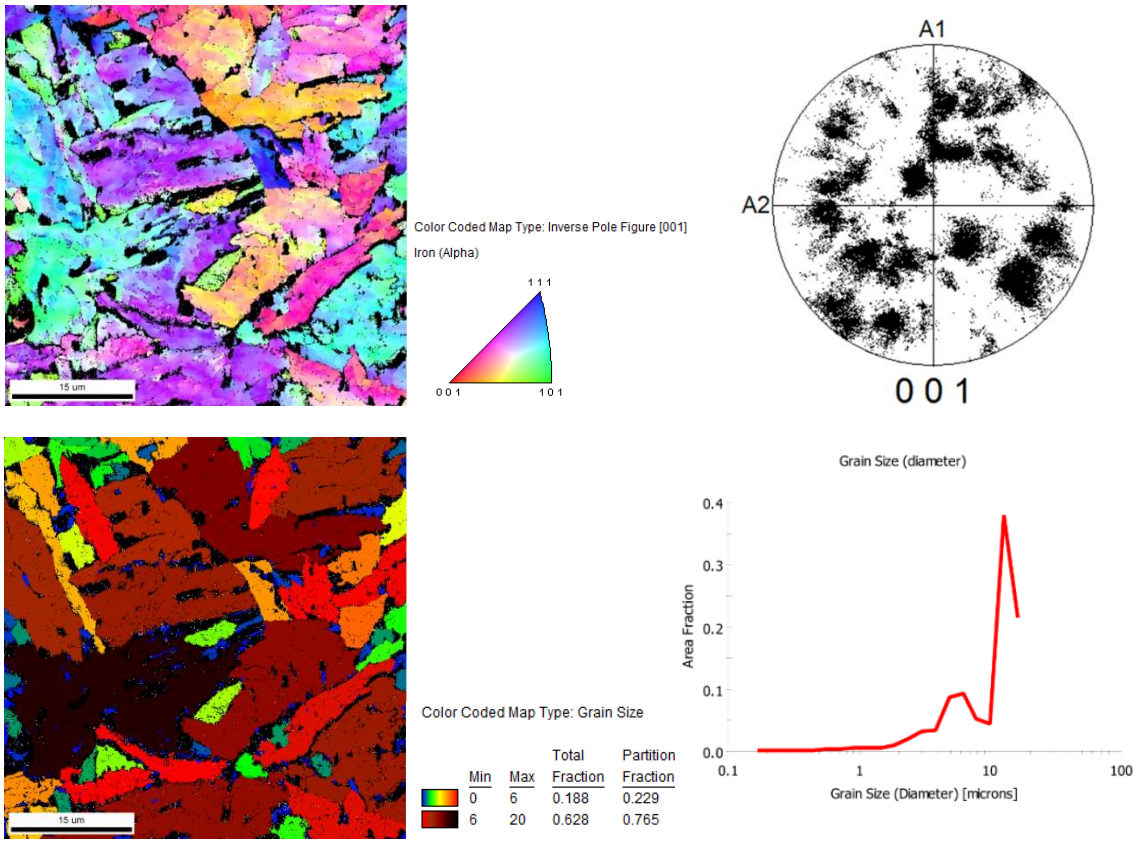
Figure 44 Sample A - ⑤ center right (AS) / (above) EBSD image and pole figure / (below) grain size and grain size distribution

4.3.2. Sample B (0.02% TiO$_2$ nanopowder, no steel powder)

Sample B seems to show a similar microstructure for the surface in as Sample A, (see Figure 45①). The area in the mid center of section 1 shows a large titanium grain and the lower center shows some WC abrasion and a more dendritic microstructure than sample A, (see Figure 45②,③). The bottom center of section 1 the weld is similar to sample but with a slight difference in grain size due to the HAZ going till the bottom of sample B resulting in larger grains possibly as a result of recrystallization, (see Figure 45④)

At the connection point of both plates, TiO$_2$ can be seen trapped in-between (see Figure 45⑤), which would suggest that the TiO$_2$ escaped the groove during the flipping of the plate or was squeezed in-between the plates during the welding process. This represents a harder, more brittle area in between the plates which can be seen as a weak point and reduce bonding and elastic properties of the weld.

In contrast to the reference sample there is tool abrasion not only on the upper surface of the sample but also within the center (see Figure 45⑥). This tool abrasion also covers a large area, seen as gold and iridescent colors in light microscopy images. TiO$_2$ can be also seen in this region with a big grain in the center and several smaller grains surrounding it. This can be further seen in Figure 72 and Figure 73. Surrounding the TiO$_2$ particles is a ring of intergranular ferrite (see Figure 45⑥a), b), page 83 Figure 74).

This area can be split in 2 areas, the upper area seen in (see Figure 45⑥a) seems to contain Widmanstätten ferrite and EDS mapping imaging shows no sign of WC in this area. The lower area (see Figure 45⑥b) seems to contain acicular ferrite. EDS analysis however shows that this region also contains WC (Figure 46, page 84 Figure 76). Further below dendritic, seemingly acicular microstructure can be seen near WC.

A region of the center right was chosen for EBSD due to having fine TiO$_2$ grains without WC presence and a microstructure finer than the surrounding area (see Figure 45⑦).
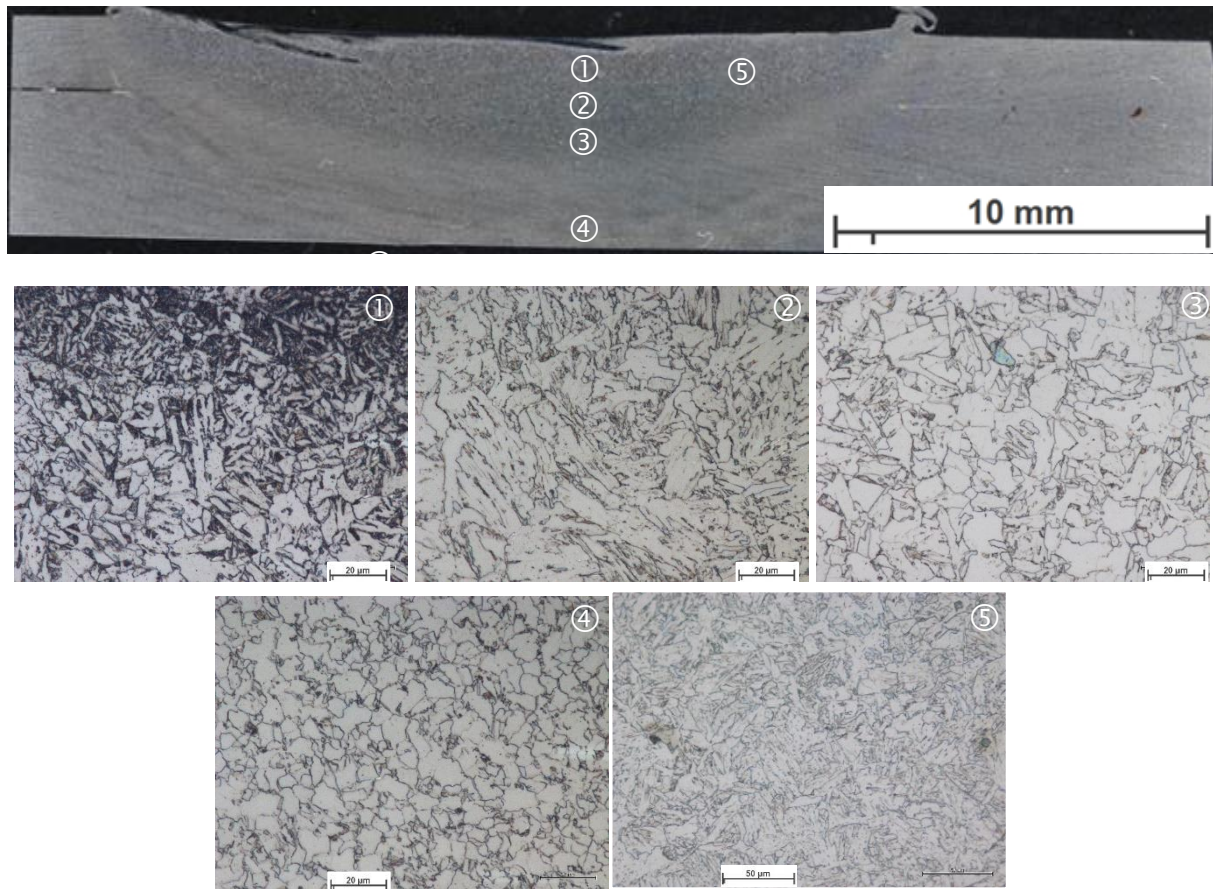
Figure 45 Sample B - LOM microstructure details: ① near surface close to WC abrasion, ② stir zone center and ③ below center, ④ outside TMAZ,⑤ TiO₂ between plates⑥, ⑥a) and ⑥b) stir zone center near TiO₂, ⑦ center right (AS))
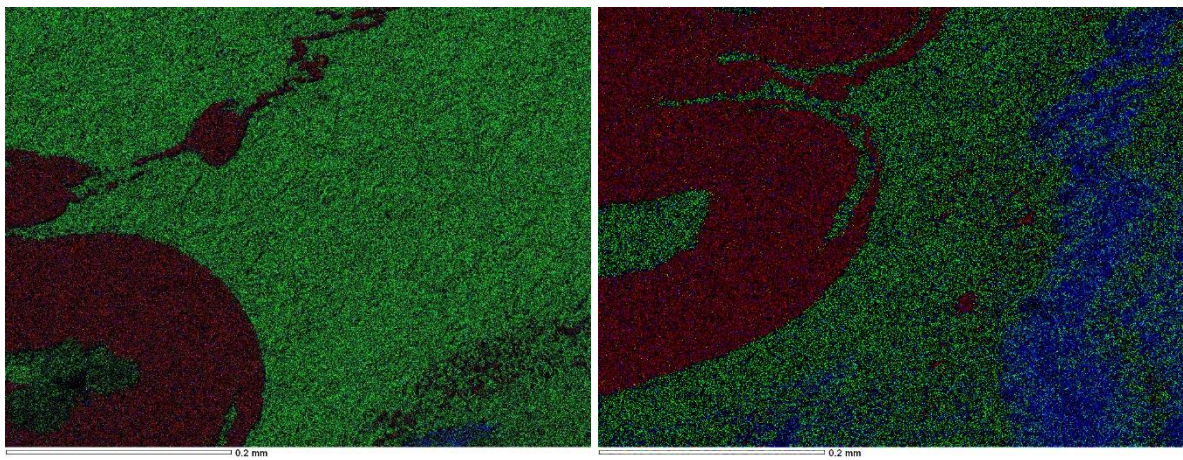
Figure 46 Sample B ⑥ EDS:⑥a (left image) and ⑥b (right image) red TiO₂, green Fe, blue WC

When looking at the EBSD analysis results and comparing it with the same area within sample A, sample A has a higher degree of order, while the same region in sample B is disordered. The pole figures of sample A and B show a clear difference as sample B shows no overall preference in orientation in the area observed and has a more circular form. When comparing the EBSD results to the LOM and SEM images (see page 85 Figure 78) it can be identified as globular ferrite. As this region contains TiO_2, while sample A has no TiO_2, the formation of globular ferrite could be attributed to TiO_2 as nucleate or indirectly due to temperature differences or a different material flow surrounding the particles. The austenite grains of sample B could not be identified. Additionally, this area seems to contain pearlite. When comparing the grain size of sample A and B in this region it can be seen that sample A has both, larger grains and a larger percentage of large grains while the grain size is smaller and more uniform in sample B (see Figure 47). This is in good agreement with the observations of LOM (see page 85 Figure 78).
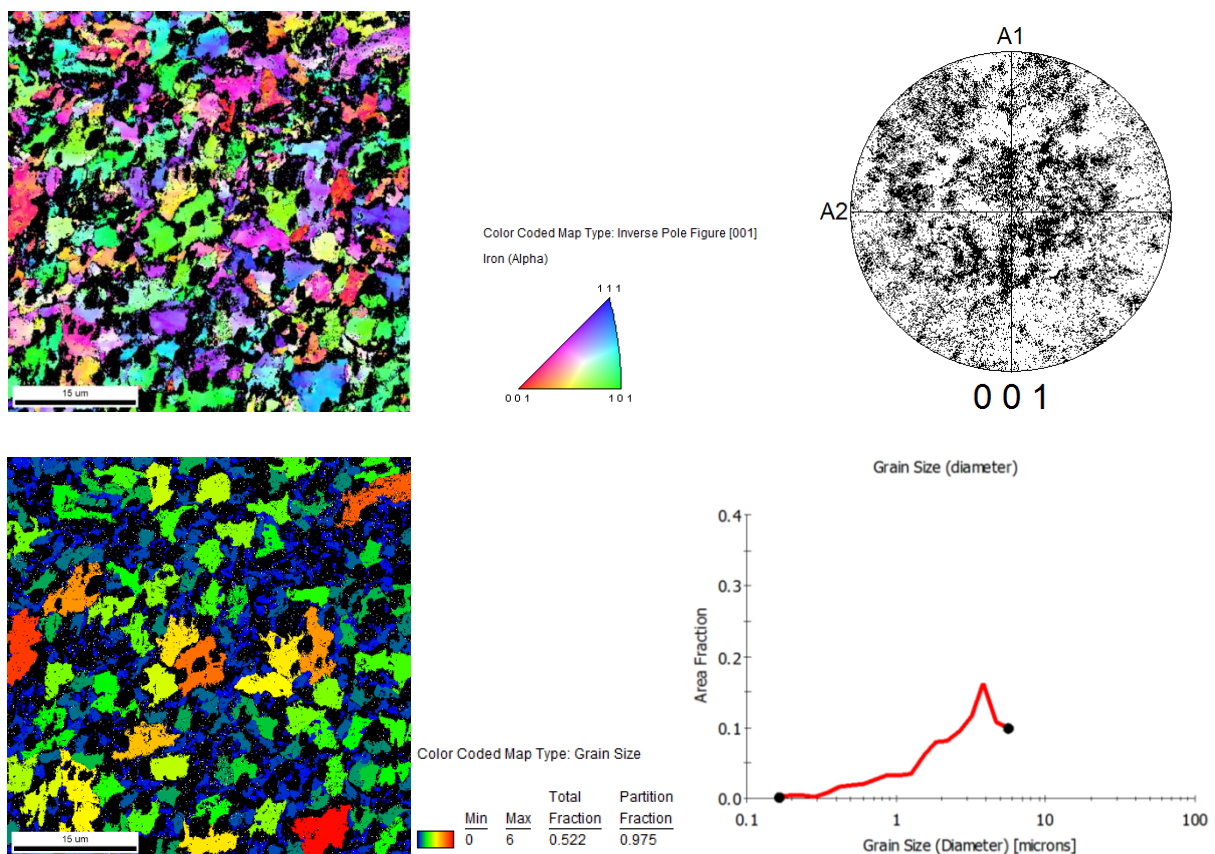
Figure 47 Sample B section 4: grain size and grain size distribution sample B

39

4.3.3. Sample C (0.06% TiO$_2$ micropowder, 99.94%steel powder)

Sample C has a similar microstructure to the reference sample (see Figure 48 ① - ④), aside from a few specific regions, such as the lower center region (see Figure 48 ③). Like in sample B, WC abrasions are present in the center of the weld and the microstructure is different along a darker region visible with macroscopic imaging (see Figure 48 ⑤). This darker area starting at the WC abrasion at the center contains a stripe-like pattern and is not present in sample A and could be due to WC abrasion and tool deformation due to the TiO$_2$ particle. Another possibility is the steel powder which was added as a filler and might has an abrasive effect.

In the center of the nugget zone a singular TiO$_2$ can be found (see Figure 48 ⑥). The TiO$_2$ grain has the typical intergranular ferrite ring around it. Beyond the ferrite ring the microstructure can be seen as primarily ferritic, made up of polygonal ferrite grains, separated by another phase at the grain boundary.
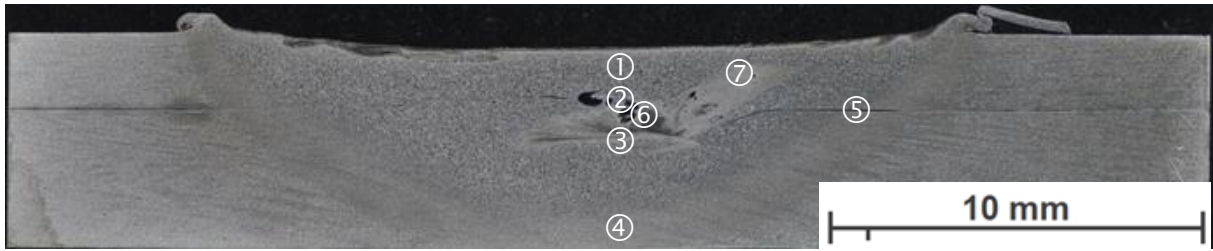

Figure 48 Sample C - LOM microstructure details: ① near surface close to WC abrasion, ② stir zone center and ③ below center, ④ outside TMAZ,⑤ center left (RS),⑥ TiO$_2$ Grain in center)

Using the SEM and EDS to investigate this phase and comparing it with literature [85], the phase seems to be pearlite (see Figure 49). Both the region near the TiO_2 and the region further away, which does not contain TiO_2 according to EDS, have a comparable microstructure see Figure 50. A direct effect of TiO_2 on this sample cannot be seen.

Figure 49 Sample C Region ⑥: EDS box scan showing pearlite at grain boundary

Figure 50 Sample C region ⑥ containing TiO_2 and region ⑤ with no TiO_2

The area surrounding the WC particle (Figure 48 Figure 50 region 6) has a similar needle like structure to sample A. starting from the WC particle a series of dark areas can be seen in both the LOM and SEM (see Figure 48 ⑤) as mentioned above. When comparing with the unpolished samples these can be narrowed down to either inclusions, defects or precipitates. An EDS analysis of this area reveals that these spots do not correspond to TiO_2, which fits the LOM observations as the particle color seems too dark to be TiO_2 in LOM images. Instead these areas seem to correspond to Si peaks in EDS and seem to have a layer with a different focus plane, which both seem to indicate that these are either inclusions or defects and the Si is SiO_2 from the grinding step.

41

Figure 51 EDS analysis region ⑤ showing no TiO_2

4.3.4. Sample D (empty groove left unfilled)

As mentioned in the experimental section Sample D had no TiO_2 in the groove but the neighboring sample had 0.06% TiO_2 in the groove, a fraction of which was assumed to have been pushed into Sample D, see Figure 52.
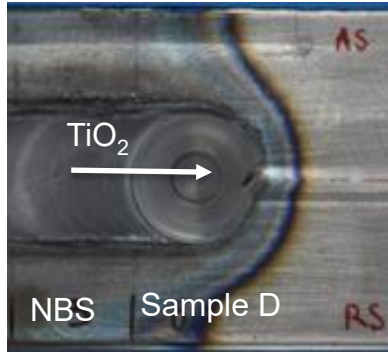
Figure 52 Sample D and neighboring sample (NBS)

Sample D has a microstructure which is very similar to sample A (see Figure 53① - ④), with the major exception of the center (see Figure 53③). In the center, at the location of the groove visible cracks exist filled with particles (see Figure 53⑤). Near this area the microstructure is similar to acicular ferrite and tiny dark spots, impurities or inclusions, which were initially assumed to be smaller grains of TiO_2 are visible in LOM which makes this region the region of most interest (see Figure 53⑤a).

Further investigation using SEM and EDS (see Figure 54) revealed that the area with the acicular microstructure does not contain TiO_2 above the detection limit of an EDS scan. The particles in the cracks which looked like TiO_2 in the light optical microscope showed a completely different appearance than TiO_2 in the electron microscope and were revealed to be SiO_2 particles via EDS.

Additionally, the tiny dark spots, which were assumed to be TiO_2 particles were in fact revealed to be small defects or inclusions, not TiO_2 particles (see Appendix chapter 7.3). Similar inclusions can be found in literature [86], where TiO_2 is not used hence it can be assumed that this not an effect of the TiO_2 but possibly be due to contaminations during welding or sample preparation.
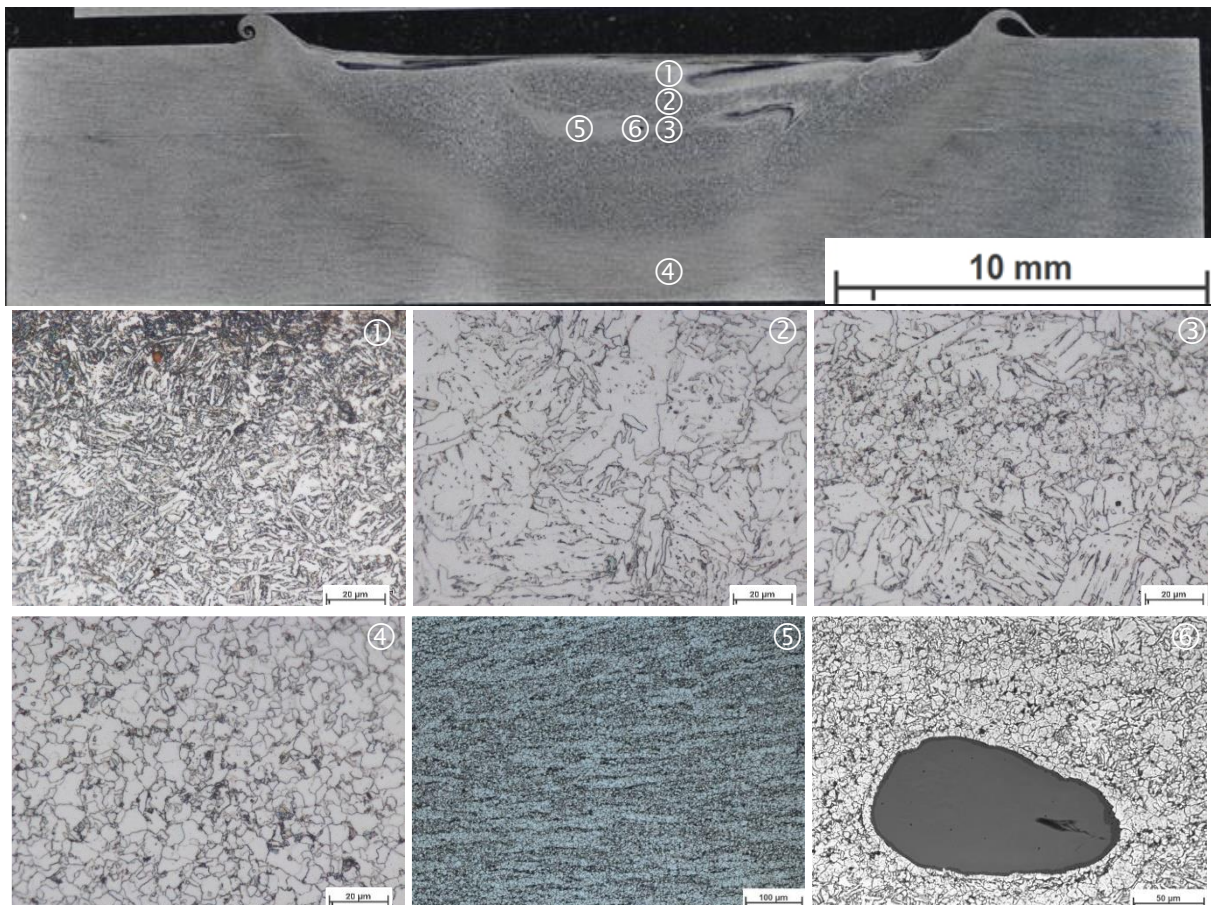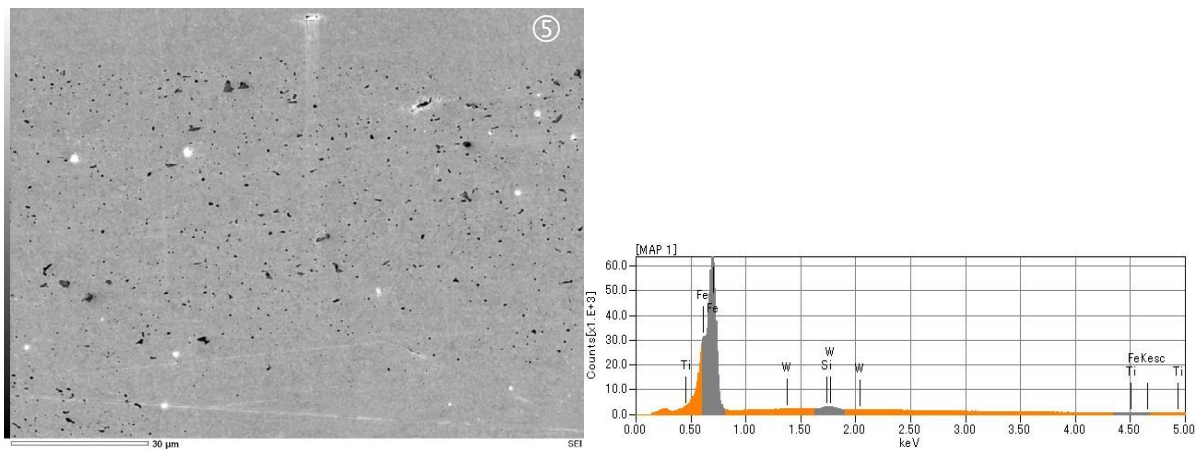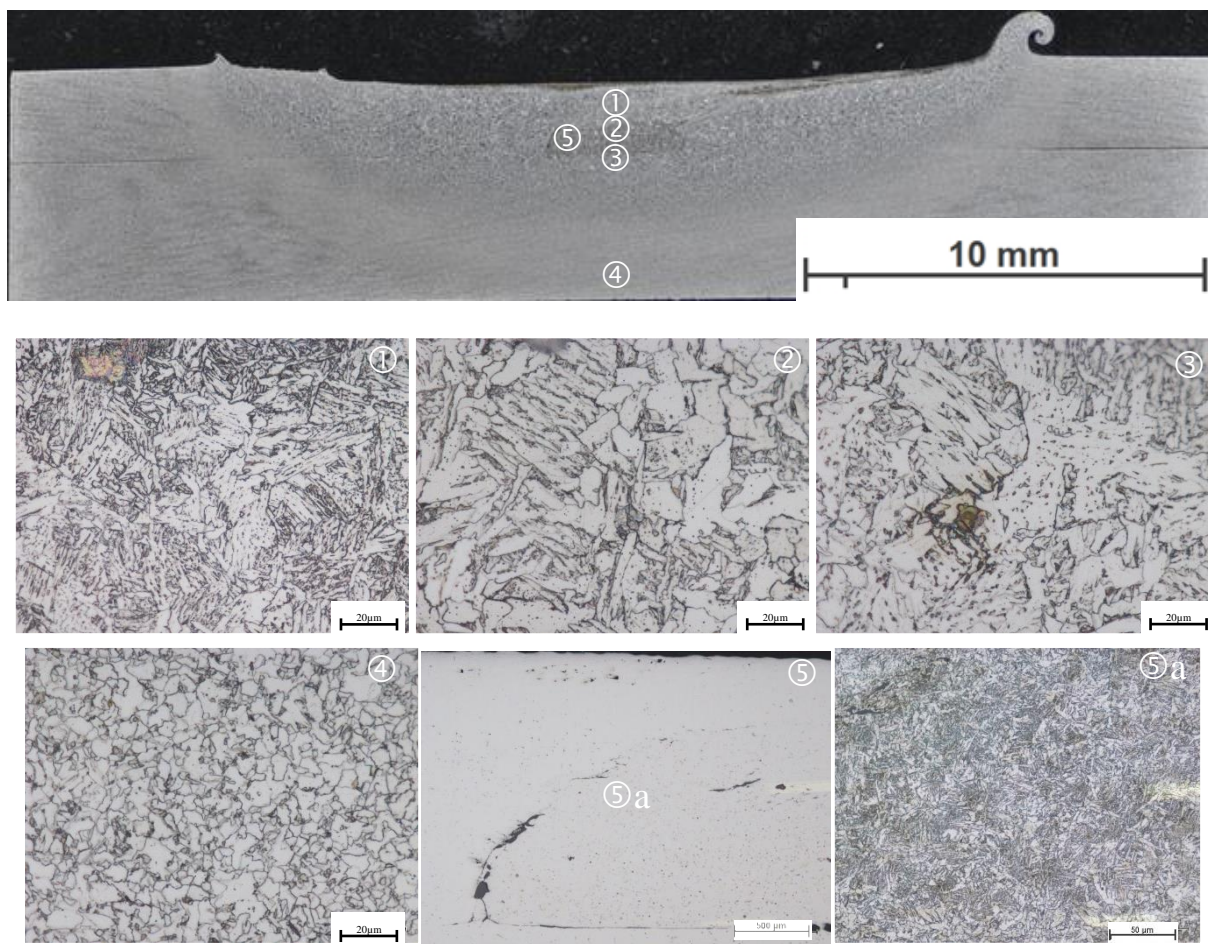
Figure 53 Sample D - LOM microstructure details: ① near surface close to WC abrasion, ② stir zone center and ③ below center, ④ outside TMAZ,⑤ particles and crack at center, ⑤a region of interest
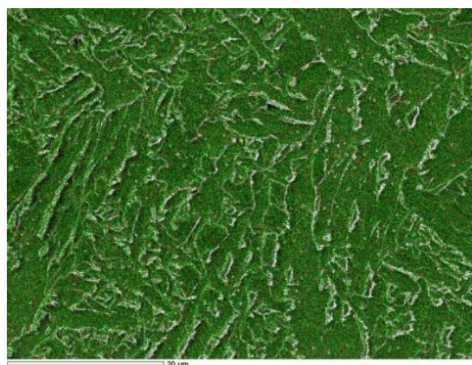
Chemical formula	ms%	mol%	Sigma
C*	1.32	5.78	0.03
O*	0.35	1.15	0.05
Si*	0.66	1.24	0.10
Ti	nd	nd	
Fe*	97.50	91.78	0.30
W*	0.16	0.05	0.39
Total	100.00	100.00	
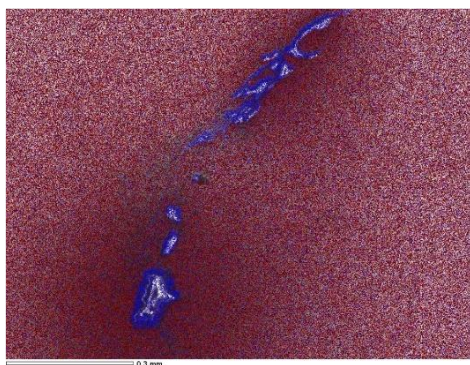
Chemical formula	ms%	mol%	Sigma
C*	1.17	5.00	0.03
O*	1.60	5.11	0.05
Si*	0.99	1.79	0.09
Ti	nd	nd	
Fe*	96.24	88.10	0.30
W	nd	nd	
Total	100.00	100.00	

Figure 54 Sample D: region⑤a SEM (top) and EDS of biggest grain in region ⑤ (below)

44

As no TiO_2 could be found in sample D the assumption that TiO_2 was being pushed in from other areas of the sample, is not valid or only in a non-detectable concentration. This fits well with the lack of WC abrasion in the middle of the center of the weld, which every sample containing TiO_2 showed.

Chemically this sample seems to be identical to the reference sample, as for why the microstructure is different, there are several possible explanations:

- A major difference is the groove: the reference sample is just two plates welded together without a groove, while sample D had an empty groove at the nugget zone, hence the welding conditions are different from the reference plate.

- At the center of the weld, sample D has several cracks or welding defects of varying size (see Figure 53⑤), which in turn might influence microstructure formation. The origin of these cracks might be the groove at the center of the weld, as this is the only sample with an empty groove and the only sample with cracks in the nugget zone.

- The tool conditions are different for sample D when compared to the other samples as the other samples were done in multiple welds per plate (Figure 37a) with each sample being taken from the first weld on the plate. Sample D on the other hand was the final sample on a weld created by using a pin for the entire plate in one continuous weld (Figure 37b). Abrasion and deformation of the tool and should therefore be much more pronounced on the tool of sample D when compared to a shorter weld, which might lead to different conditions in terms of stirring, friction and tool abrasion when comparing it with the other samples, such as the reference. This might explain the different microstructure when compared to the reference sample.

4.3.5. Sample E (0.02% TiO₂ nanopowder, 99.98% steel powder)

Sample E is similar to A in its microstructure at the center (see Figure 55 ① - ④), but contains WC abrasions in the center and a dark pattern in the TMAZ starting at the WC particle as with sample C. The main difference is that sample E's nugget zone has regions similar to the reference sample in the dark area (see Figure 55 ⑤, Figure 56).
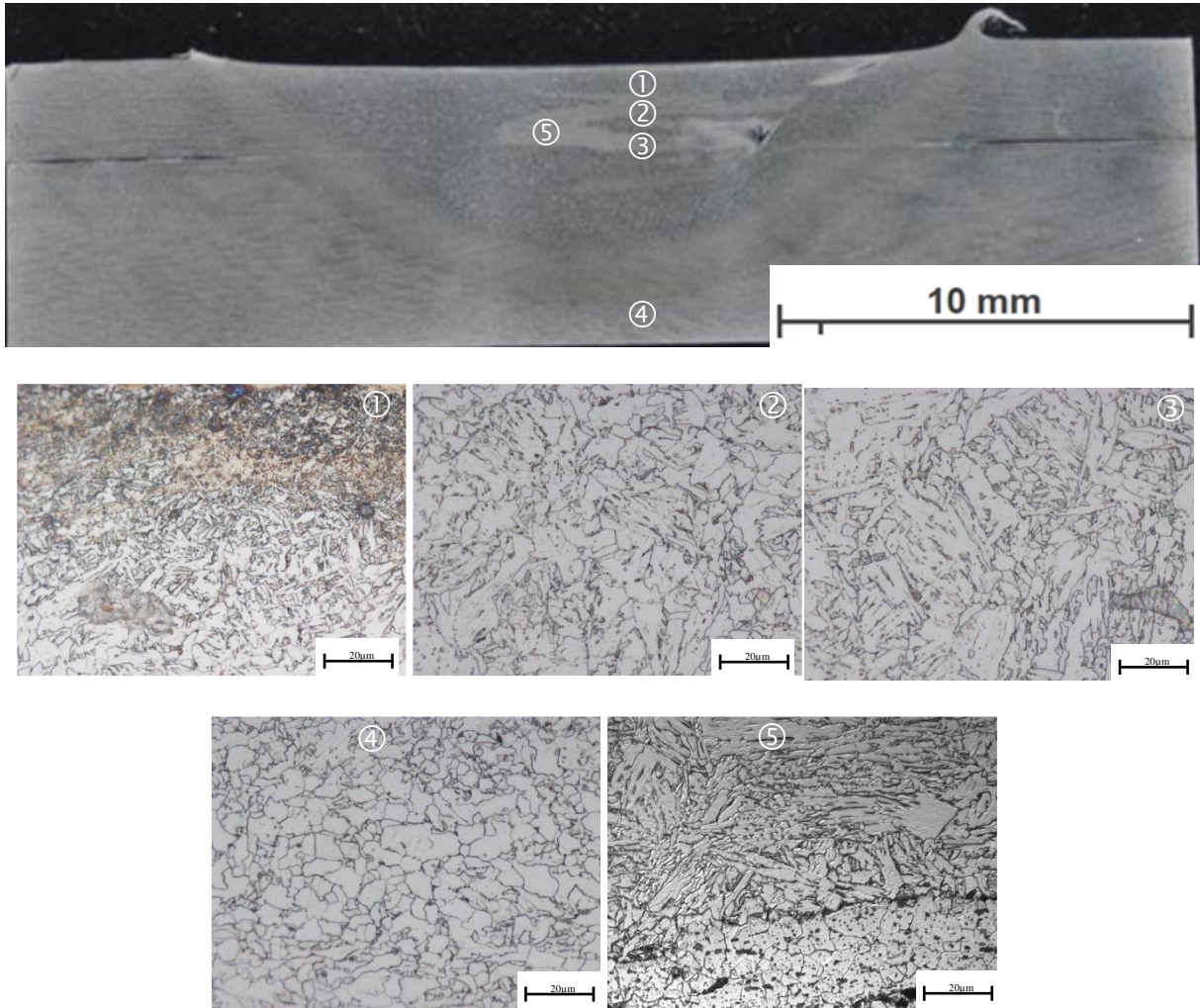

Figure 55 Sample E - LOM microstructure details: ① near surface close to WC abrasion, ② stir zone center and ③ below center, ④ outside TMAZ,⑤ center left (RS))

This might be explained by the lower content of TiO₂ than in sample C, which might have led to a lower amount of tool abrasion, which in turn might have led to a limited microstructure change in the sample. Another explanation would be the higher iron powder content leading to the formation of localized microstructure similar to the reference sample by recrystallization of the iron powder.

The EDS in the darker region shows similar results as with sample C not containing any TiO₂ but Si instead. Silicon is introduced into the sample during grinding and polishing. As with sample C the dark area shows a different focal plane meaning it is either a defect or an

inclusion.

There are two major possibilities for these observations:

- The dark areas in EDS could be defects caused by abrasion during grinding, which were then filled with silicon from the sandpaper. This would not explain why Sample A and B do not show the dark spots and why the defects are bigger, deeper and the defect area larger in sample C and E than in sample D. Therefore, this explanation seems to be unlikely.
- The steel particles might have remained solid instead of semi-fluid during welding and created defects through abrasion of the surrounding softened material. These defects would then be filled with silicon during the grinding process. This explanation seems more likely as only Sample C and E both show the dark areas and are the only samples containing steel powder

These cause for the defects or inclusions cannot be verified with the limited data available, therefore they remain a point of speculation.

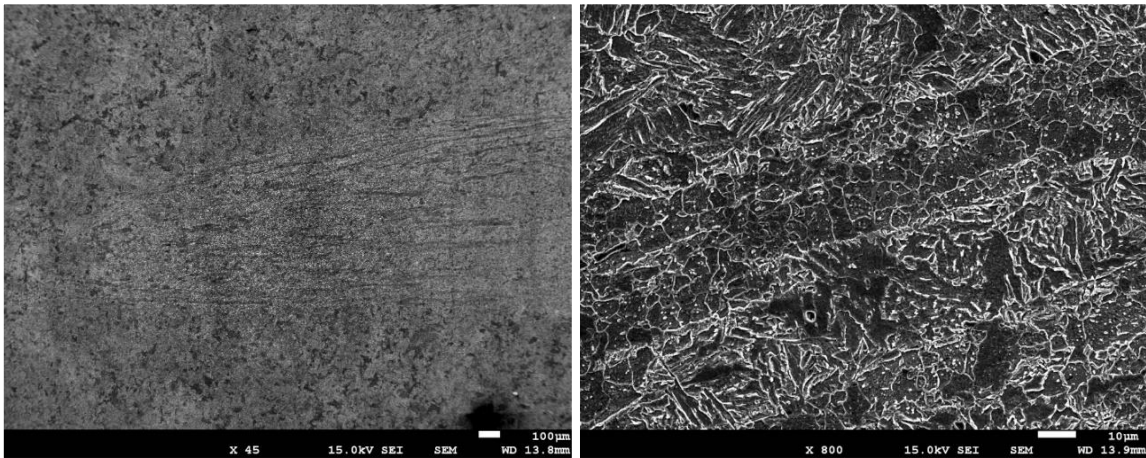Figure 56 Dark area SEM showing ferrite grains like sample E and bainite akin to reference

As with sample B and C WC abrasions are present in the center of the sample. The microstructure is more needle like in the surrounding area of WC. The dark welding pattern seems to origin within the WC abrasion, if this is due to the abrasion being located at the center of the nugget zone or due an effect of the abrasion itself is unknown.

4.3.6. Sample F (Hot pressing sample)

As mentioned in the experimental part, the pressing process was done in two thermal cycles. One was with load meant to fuse the samples and one with just the temperature cycle of the FSW process which simulates the thermal aspect of the welding process, see Figure 57. Shortly after reaching 1150°C in the first heating cycle the heating current started to break down as soon as the load was increased, stopped breaking down as the load surpassed 2,5 kN and recovered slightly but never went above 800°C (see Figure 57 below 400 seconds). The second heating cycle went exactly as planned (see Figure 57 above 800 seconds).

Possible reasons for the current breakdown:

- Sample dimensions and shape differ from the standard cylindrical samples for this machine, therefore the machine is not designed to handle these samples.
- Until the load was applied the upper part of the sample rested on TiO_2 particles which are not conductive hence the moment a load was applied the heating coil had to deal with two conductors connected by a semiconductor, followed by two conductors connecting with regions of non-conductivity.

The exact explanation cannot be determined, as there is not enough data and in-depth knowledge in the field of mechanics and working of the machine setup to judge the situation. The sample created during this process, sample F was analyzed. The microstructure of sample F (see Figure 58) is similar to the microstructure of the reference sample but contains the ferrite ring around the TiO_2 as seen in the FSW samples containing TiO_2 (see Figure 58).
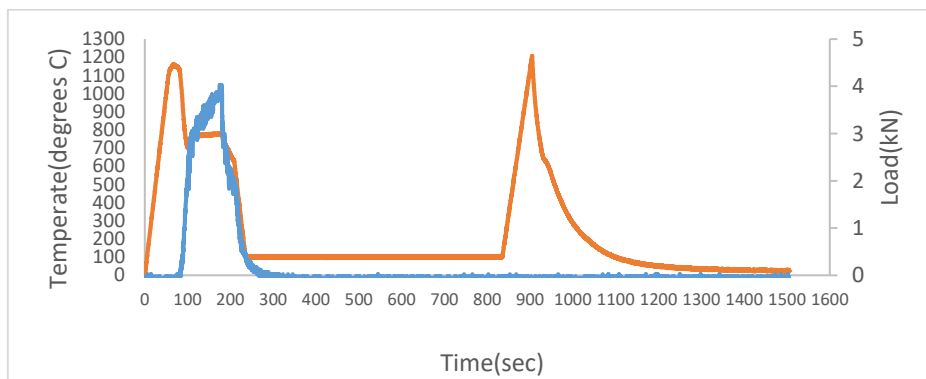

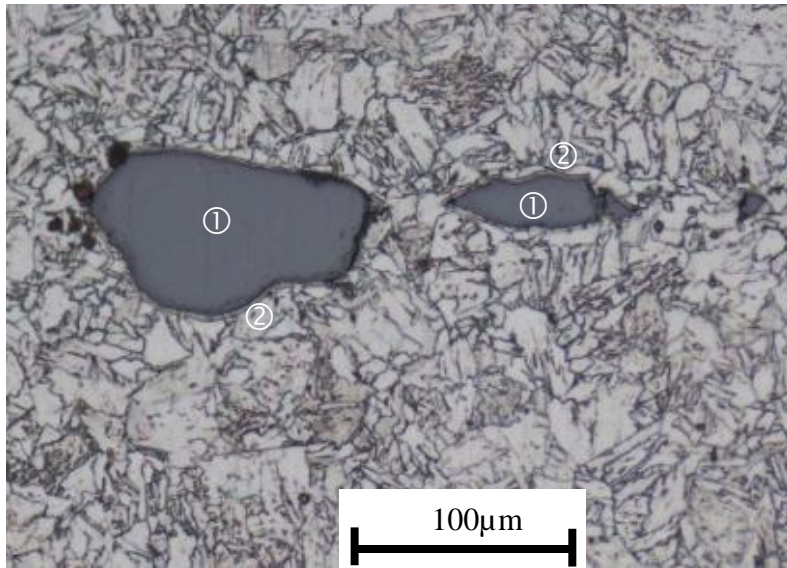Figure 57 Temperature (orange) and load (blue) of sample F

Figure 58 TiO$_2$ in sample F (①) with a thin ferrite ring surrounding it (②)

4.3.7. TiO₂ composition and Influence on microstructure

The TiO_2 micropowder which was used to create the sample C had a black, crystalline appearance, contrary to the white powdery appearance described in literature and product catalogs of TiO_2 producers, therefore it was analyzed using SEM and XRD [87, 88].

The analysis showed that there are impurity particles containing Zr, Si, Al and that even some of the TiO_2 particles are coated with these impurities and with iron impurities. The FELMI report assumes the main impurity to be $ZrSiO_4$.

Furthermore, the TiO_2 could be identified as rutile without anatase and brookite (see chapter 7.3 for EDS results). The metallic impurity particles and coating of the TiO_2 could be the explanation for the dark color and metallic gloss of the TiO_2 powder. Further literature search revealed that the TiO_2 is possibly rutile sand, which is a heavy mineral sand composed of the mineral rutile and used in SMAW flux powders and rods. [89 – 92]

The seller of the TiO_2 powder, AMA Industrial Co, sells flux powders but not pure TiO_2 [93]. The photos of rutile sand from multiple manufacturing companies are near identical in texture color and gloss when compared to the TiO_2 micropowder.

Hence it can be assumed that the powder used during manufacturing is not as previously thought industrially manufactured TiO_2 via chloride process from ilmenite or sulfate process from rutile minerals. The lack of chlorification and re-oxidization leads to a different color and morphology for natural rutile compared to synthetic rutile and explains the high impurity content, when compared to synthetic rutile powder. [94, 95]

The TiO_2 in the samples B and C and shows a similar appearance of particles. The sample without steel added, sample B shows the largest grain size and the highest amount of TiO_2 in the sample. Sample C has a smaller grain size and less TiO_2 within the weld zone, while in sample E TiO_2 particles were not found. Sample B and E both contained anatase nanopowder with a grain size of 10-15 nm while sample C had rutile micropowder with a grain size of 63 to 90 micrometers. Nevertheless, both sample B and C formed large agglomerates of sintered particles without any major difference with sizes visible to the naked eye. This can be attributed to two major factors. Firstly, anatase undergoes an irreversible phase transformation into rutile at temperatures between 500 and 700°C which is well below the temperate of the welding process. Nevertheless this process needs time and it is unclear if it can be completed during the FSW thermal cycle. [45, 96]

Secondly, under high pressure the sintering temperate of TiO_2 can be drastically reduced down to 550°C-1000°C also depending on TiO_2 dispersion and particle size [96]. However, the exact details of this process and how the TiO_2 could be sintered so fast, since sintering is both a

function of time, pressure and temperature, the former measured in hours not seconds cannot be determined as there remain too many unknown factors and there was no literature available concerning the sintering of TiO_2 using friction stir welding or friction stir processing.

Another factor is that the size and amount of TiO_2 does not seem to correspond with the percentage of TiO_2 added, as sample B and E should contain the same amount of TiO_2, but sample B shows a lot more TiO_2 particles. Sample C should contain three times the amount of TiO_2 than sample B or E and therefore a higher density of TiO_2 particles but this could not be found within the sample instead sample B has the greatest amount of TiO_2 agglomerates of all samples.

As mentioned in the methodic section sample B was created without the addition of steel powder and the TiO_2 was observed to stick to the tool, was pushed towards the end of the welding zone and agglomerated there. To prevent such agglomeration Sample C and E on the were created by mixing steel powder and TiO_2 in a ball mill and adding this mixture into the groove, the percentage of TiO_2 being 0.02% for sample C and 0.06% for sample E with the rest being steel powder, see Table 3.

Since the regions of the weld from where the samples were obtained were not documented, the sampling point of sample C and E are unknown.

Sample B however has a significant amount of TiO_2 in the sample and should therefore come from the end of the weld section due to the TiO_2 sticking to the tool till the end of the weld as mentioned above. Therefore, if all three samples were taken from the same region of the weld, the mixing with steel powder does not seem to cause as much of an agglomeration as without the steel powder, which would explain the difference between sample B and samples C and E. The difference between sample C and E on the other hand cannot be explained by this, especially the lack of TiO_2 agglomerates in sample E unless it is assumed that low amounts of Nano TiO_2 do not agglomerate and are easier dispersed than micro TiO_2. This theory does not fit to the characteristics of nanoparticles which have a huge surface energy and therefore tend to agglomerate to minimize their surface energy [97].

If the samples were not taken from the same region, a lower amount of agglomeration in sample C cannot be assumed and the difference between the samples could simply be from the different locations within the weld. Overall, this question cannot be answered with the data available and therefore remains uncertain.

The ring of ferrite surrounding the TiO_2 particles however can be explained as intergranular ferrite.

Finally, the high heat capacity and specific heat of TiO_2 which is magnitudes higher than

X80steel, which is similar to X70 would point towards a much slower cooling rater in the area surrounding the TiO$_2$. [98, 99] This would explain the ferrite ring and possibly the area of Widmanstätten ferrite in the center right of sample B as the low cooling rate lead to microstructure of different ferrite types and pearlite instead of bainite or even martensite.

4.3.8. Influence of WC tool wear

WC tool wear is present in form of a gold colored, partly tinted deposition at the surface of all 5 samples. This area is in direct contact with the tool, which explains the abrasion at the surface. Additionally, all samples with measurable TiO_2 content show WC abrasions inside the nugget zone. This can be attributed to the WC being sheared off on the TiO_2 particles, which possess around 3 times the hardness of the surrounding steel. [100 – 103]

After etching the area surrounding the WC is darker than the rest of the sample and in some samples tint colored. EDS analysis shows the presence of low amounts of WC in this area (see chapter 4.3.2).

This area and the area surrounding it has a finer, more needle like structure, which might be attributed to WC nucleation particles.

The melting point of WC lies at 2870°C [104], which puts it far above the heat caused during FSW. Therefore, it can be assumed that WC remains solid and in its carbide form, although a chemical decarburization might be possible. A look at its phase diagram also excludes any phase transformations [105].

The cobalt matrix on the other hand has a lower melting point of 1495°C [106], comparable to steel, which makes it more susceptible to flow and mixing with the sample. Cobalt might therefore form finely dispersed particles on acicular ferrite could nucleate but there is literature available to prove this theory and the EDS did not include Co, as the cobalt matrix was not considered during the SEM observation phase.
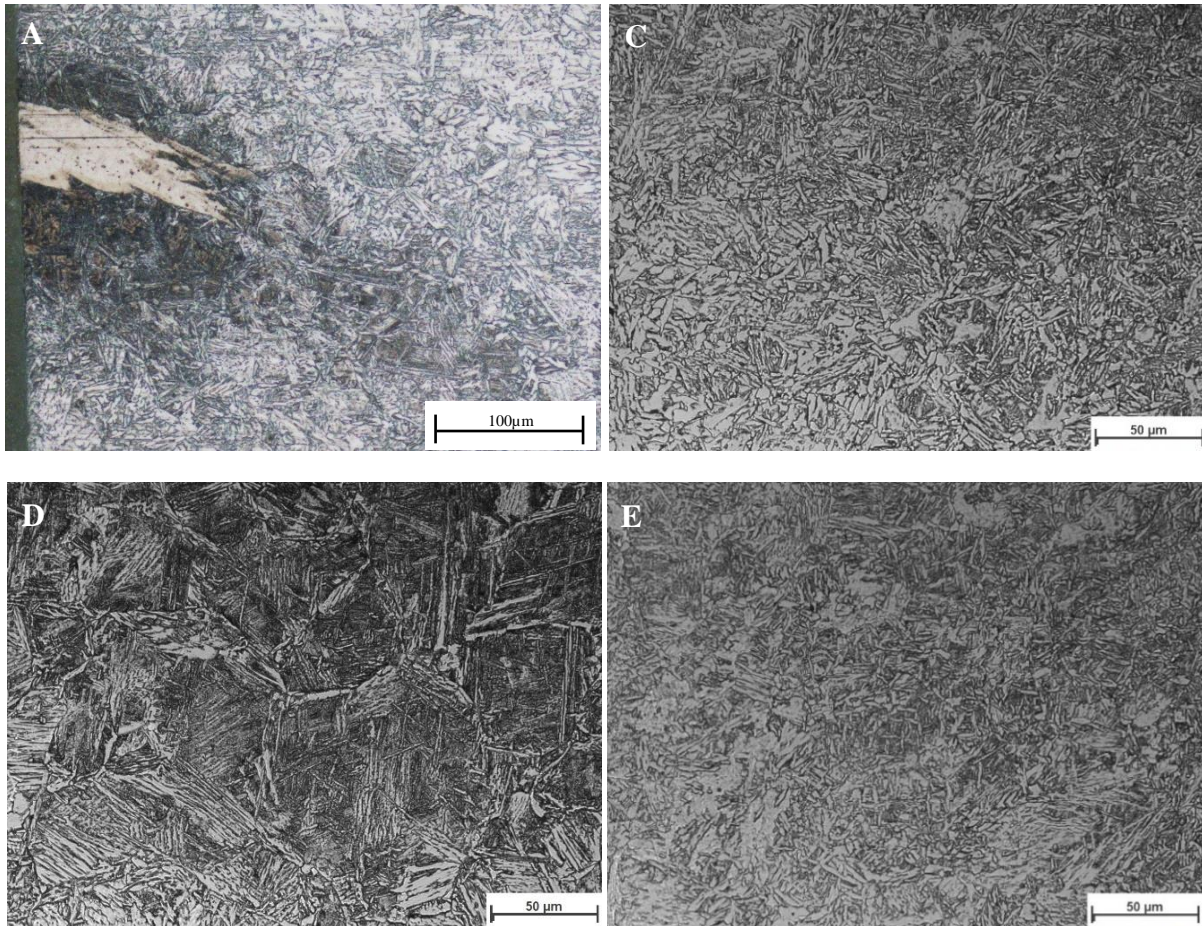
Figure 59 LOM WC containing area sample A, C, D, E

4.3.9. Acicular ferrite locations and formation

As mentioned above, only sample B and sample D show microstructure similar to acicular ferrite and Widmannstätten ferrite.

Sample B shows acicular in regions where WC abrasion and TiO_2 particles overlap and sample D shows it in a region not containing either compounds.

The overlap of WC and TiO_2 in the regions containing acicular ferrite in sample B makes the effect of TiO_2 on the formation acicular ferrite ambiguous, as this could be also attributed to an effect of the WC, due a particle induced nucleation similar to the effect of oxides.

If the presence of WC in the acicular region of sample B is not seen as an influencing factor, the finer particles of TiO_2 visible in LOM would explain the formation of acicular ferrite in this region as it would be consistent with nucleation of acicular ferrite on fine grained TiO_2 mentioned in the literature. A possibility why most of the samples lack acicular ferrite is that the TiO_2 particle size is too big for the formation of acicular ferrite.

Both sample B and D show Widmanstätten ferrite, sample B in a region near TiO_2 and between the major tool abrasion, sample D again shows Widmanstätten ferrite in a region not containing WC or TiO_2.

54

Since sample D shows both acicular ferrite and Widmanstätten ferrite without any TiO_2, the growth mechanism of both acicular ferrite and Widmanstätten ferrite X70 steel created via FSP seems to be unclear, certain literature suggests a link between cooling time and acicular ferrite formation, with acicular ferrite forming at cooling rates between 5 and 40°C/s. [107]

5. Conclusion and Outlook

5.1.   Conclusions

Different amounts of TiO$_2$ powder types were distributes in X70 steel using FSP. The following shortcomings arose:

- An agglomeration of the TiO$_2$ powder and of WC particles from tool wear was found in the stir zone. Thus, all the manufactured specimens were inhomogeneous.
- The sampling points are unknown and there it is uncertain whether all samples are from the same section of the weld.

When looking at the results following conclusions can be made:

- No clear link between TiO$_2$ and acicular ferrite can be found in the samples.
- In sample B a link between TiO$_2$ and Widmanstätten ferrite can be found.
- A link between TiO$_2$ and fine grained globular ferrite can was found.
- A mixture of TiO$_2$ and steel seems to result in a polygonal ferritic microstructure.
- The TiO$_2$ particles themselves seem to agglomerate and sinter under FSP conditions.
- WC-Co tool abrasion seems to be surrounded with a needle like, possibly acicular ferrite microstructure which suggests a possible link between WC or cobalt and acicular ferrite.

Nevertheless, the small number of samples and large difference between most samples does not allow for definite conclusions.

5.2.   Outlook

5.2.1. Recommended changes to sample creation and preparation

As this thesis has been a follow-up to the work of a predecessor and the samples not made especially for this thesis some parts of the sample creation and preparation process need to be improved to get a higher amount of information during analysis:

- The main improvement would be a higher number of welds with the same conditions and a higher number of sampling points on each weld to get more representative results for sample.
- To have better references for the different types of samples such as the samples with mixed additives like steel mixed with TiO$_2$ or samples which are located next to filled groove but have only an empty groove, multiple reference samples should be created, such as a sample with the groove filled with only steel powder and a sample with just

an empty groove. These reference samples should be compared with each other and the corresponding sample with additive. The same sampling points on the weld should also be chosen to have comparable results.

- To compare TiO_2 nanopowder, TiO_2 micropowder, steel-TiO_2 mix and pure TiO_2 samples of each powder type should be created and analyzed for all concentration ranges. A higher purity of the micropowder would also be required to be sure that effect of impurities can avoided, which would require either purified rutile or more pure rutile sand.

- As the abrasions lead to a fast wear down of the welding tool and to a modified microstructure, this could be avoided by using tools made from the superhard materials class such as cubic boron nitride, WB_4 or OsB_2 but the price may be prohibitively expensive. Alternatively composites with high hardness, such as WC-Co-BN could be used.

5.2.2. Additional recommended analyses

In the course of this thesis several unanswered questions have been encountered and some analyses cut short, both could be concluded in future projects:

- An investigation into the agglomeration and sintering of ceramic particles such as TiO_2 under FSW/FSP conditions and methods on how to avoid agglomeration and sintering could lead to a finer more dispersed TiO_2 inside the weld which in turn might promote the formation of acicular ferrite. Suggested methods would be multi-pass welding, spray drying of TiO_2 inside the weld groove, creating a better mixture of steel and TiO_2 by using similar grain sizes during mixing or the use of surfactants to reduce surface energy of the additive.

- An investigation of the creation and effect of WC abrasion on the microstructure of FSW welded X70 with and without the TiO_2 steel or FSW with WC particles instead of TiO_2 could lead to a better understanding on the effect of the WC abrasions on the microstructure of pipeline steel.

- Another point of interest would be the cobalt content of the FSW tool and the effect on the microstructure of steel.

- During the project additional EBSD measurements were done for sample C and E but the reference measurement on sample A failed due to drift while measuring. Therefore, the EBSD results of sample C and E were not further analyzed. This analysis could be redone and compared with the result from Sample B.

- In addition to sample F further hot pressing samples were created using just the FSW temperature cycle. The samples were created with and without TiO_2 addition. Due to time constraints investigation of these was halted. The other hot pressing samples could be analyzed and compared to sample F.

- The reason for the appearance of acicular ferrite but the lack of TiO_2 or WC in sample D's welding zone is worth further investigation as it could lead to an additive free way of producing acicular ferrite with FSW.

- Using laser confocal microscopy to simulate the temperature program of the FSW process and film the formation of acicular ferrite during cooling was planned but suspended after the initial test runs due to the unclear origin of acicular ferrite in Sample B and D. This method could supplement and improve some of the above-mentioned analyses and is therefore recommended.

6. References

[1] R. Pouriamanesh and K. Dehghani, "Micro structure and Hardness of Steel-TiO2 Composite Produced by Friction Stir Welding," *Indian J. Sci. Technol.*, vol. 11, no. 8, pp. 1–11, Feb. 2018.

[2] V. Schwinn, M. Gräf, and K. Hulka, "Production of Large Diameter Pipes Grade X 70 with High Toughness using Acicular Ferrite Microstructures," *Int. Conf. Appl. Eval. High Grade Linepipes Hostile Environ.*, vol. 47, p. 14, 2002.

[3] I. K. Nuruddin, "Effect of welding thermal cycles on the heat affected zone microstructure and toughness of multi-pass welded pipeline steels," CRANFIELD UNIVERSITY, 2012.

[4] S. Ghahremani Ghadar, T. Saeid, J. Mollaei Milani, and M. Saman Safavi, "Effect of inclusions on the microstructure and mechanical properties of SMAW welded API 5L Grade B steels," 2016.

[5] S. Balos, L. Sidjanin, M. Dramicanin, D. Labus, and B. Pilic, "Rutile Electrodes Enhanced with TiO2 Nanoparticles," *Adv. Mater. Res.*, vol. 1138, pp. 69–74, Jul. 2016.

[6] "API5L 45th Edition Specification for Line Pipe." AMERICAN PETROLEUM INSTITUTE, 2012.

[7] *ISO 3183*, vol. Third edit. International Organization for Standardization, 2012.

[8] J. L. Dossett and H. E. Boyer, "Practical heat treating," *Fundam. Heat Treat. Steel*, p. 296, 2006.

[9] T. Chihi, A. Bouhemadou, and S. Bin-Omran, "Structural, elastic, and thermodynamic properties under pressure of the FeC in the martensitic phase: an ab-initio study," *High Press. Res.*, vol. 33, no. 3, pp. 572–583, Aug. 2013.

[10] H. Berns, G. Scheibelein, and W. Theisen, *Ferrous Materials: Steel and Cast Iron*. Springer Berlin Heidelberg, 2008.

[11] C. West, V. B. Trindade, U. Krupp, and H.-J. Christ, "Theoretical and experimental study of carburisation and decarburisation of a meta-stable austenitic steel," *Mater. Res.*, vol. 8, no. 4, pp. 469–474, Dec. 2005.

[12]   F. C. Campbell, *Elements of Metallurgy and Engineering Alloys*. ASM International, 2008.

[13]   D. a. Porter and K. E. Easterling, *Phase Transformations in Metals and Alloys*. 1992.

[14]   L. B. Godefroid, L. C. Cândido, R. Vicente, B. Toffolo, L. Henrique, and S. Barbosa, "Microstructure and Mechanical Properties of Two Api Steels for Iron Ore Pipelines."

[15]   Z. Li, Z. Wen, F. Su, R. Zhang, and Z. Zhou, "Modeling research on pearlite-to-austenite transformation in hypereutectoid steel containing Cr," *J. Alloys Compd.*, vol. 727, pp. 1050–1056, 2017.

[16]   G. N. Haidemenopoulos, *Physical Metallurgy: Principles and Design*. CRC Press, 2018.

[17]   B. L. Bramfitt and A. O. Benscoter, *Metallographer's Guide: Practice and Procedures for Irons and Steels*. ASM International, 2001.

[18]   R. Ghomashchi, W. Costin, and R. Kurji, "Evolution of weld metal microstructure in shielded metal arc welding of X70 HSLA steel with cellulosic electrodes: A case study," *Mater. Charact.*, vol. 107, pp. 317–326, Sep. 2015.

[19]   R. A. Ricks, "The nature of acicular ferrite in HSLA steel weld metals," vol. 17, pp. 732–740, 1982.

[20]   G. Thewlis, "Classification and quantification of microstructures in steels," *Mater. Sci. Technol.*, vol. 20, no. 2, pp. 143–160, 2004.

[21]   H. K. D. H. Bhadeshia, *Bainite in Steels: Transformations, Microstructure and Properties*, 2nd Revise. IOM Communications Ltd, 2001.

[22]   D. Rasouli, S. Khameneh Asl, A. Akbarzadeh, and G. H. Daneshi, "Effect of cooling rate on the microstructure and mechanical properties of microalloyed forging steel," *J. Mater. Process. Technol.*, vol. 206, no. 1–3, pp. 92–98, 2008.

[23]   A. David, "Ferrite Morphology and Variations in Ferrite Content in Austenitic Stainless Steel Welds," *Weld. J.*, pp. 63–71, 1981.

[24] Y. Li, J. A. Wilson, D. N. Crowther, P. S. Mitchell, A. J. Craven, and T. N. Baker, "The Effects of Vanadium, Niobium, Titanium and Zirconium on the Microstructure and Mechanical Properties of Thin Slab Cast Steels," *ISIJ Int.*, vol. 44, no. 6, pp. 1093–1102, 2004.

[25] G. Krauss, *Steels: Processing, Structure, and Performance, Second Edition*. ASM International, 2015.

[26] Y. T. Chi, Y. T. Tsai, B. M. Huang, and J. R. Yang, "Investigation of idiomorphic ferrite and allotriomorphic ferrite using electron backscatter diffraction technique," *Mater. Sci. Technol. (United Kingdom)*, vol. 33, no. 5, pp. 537–545, 2017.

[27] S. S. Babu, "The mechanism of acicular ferrite in weld deposits," *Curr. Opin. Solid State Mater. Sci.*, vol. 8, no. 3–4, pp. 267–278, 2004.

[28] T. A. Palmer and J. W. Elmer, "Direct observations of the formation and growth of austenite from pearlite and allotriomorphic ferrite in a C-Mn steel arc weld," *Scr. Mater.*, vol. 53, no. 5, pp. 535–540, 2005.

[29] K. F. Al Hajeri, C. I. Garcia, M. Hua, and A. J. Deardo, "Refinement of Ferrite Grain Size through Particle Stimulated Nucleation (PSN) Mechanism in Heavy Steel Sections," *Mater. Sci. Technol.*, pp. 51–62, 2005.

[30] S. J. Lee, J. S. Park, and Y. K. Lee, "Effect of austenite grain size on the transformation kinetics of upper and lower bainite in a low-alloy steel," *Scr. Mater.*, vol. 59, no. 1, pp. 87–90, 2008.

[31] E. Nagy, V. Mertinger, F. Tranta, and J. Solyom, "Deformation induced martensitic transformation in stainless steels," *Mater. Sci. Eng. A*, vol. 378, pp. 308–313, 2004.

[32] A. G. Khachaturyan, *Theory of Structural Transformations in Solids*. Dover Publications, 2013.

[33] H. Dong, X. Hao, and D. Deng, "Effect of Welding Heat Input on Microstructure and Mechanical Properties of HSLA Steel Joint," *Metallogr. Microstruct. Anal.*, vol. 3, no. 2, pp. 138–146, Apr. 2014.

[34] S. H. C. Park, Y. S. Sato, H. Kokawa, K. Okamoto, S. Hirano, and M. Inagaki, "Microstructural characterisation of stir zone containing residual ferrite in friction stir welded 304 austenitic stainless steel," *Sci. Technol. Weld. Join.*, vol. 10, no. 5, pp. 550–556, 2005.

[35] H. Cho *et al.*, "Microstructural analysis of friction stir welded ferritic stainless steel," *Mater. Sci. Eng. A*, vol. 528, no. 6, pp. 2889–2894, 2011.

[36] A. K. Lakshminarayanan and V. Balasubramanian, "An assessment of microstructure, hardness, tensile and impact strength of friction stir welded ferritic stainless steel joints," *Mater. Des.*, vol. 31, no. 10, pp. 4592–4600, 2010.

[37] X. Geng *et al.*, "Microstructure, Mechanical and Corrosion Properties of Friction Stir Welding High Nitrogen Martensitic Stainless Steel 30Cr15Mo1N," *Metals (Basel).*, vol. 6, no. 12, p. 301, 2016.

[38] H. Ashrafi, M. Shamanian, R. Emadi, and M. Ahl Sarmadi, "Comparison of Microstructure and Tensile Properties of Dual Phase Steel Welded Using Friction Stir Welding and Gas Tungsten Arc Welding," *Steel Res. Int.*, vol. 89, no. 5, pp. 1–8, 2018.

[39] Y. S. Sato, T. W. Nelson, C. J. Sterling, R. J. Steel, and C. O. Pettersson, "Microstructure and mechanical properties of friction stir welded SAF 2507 super duplex stainless steel," *Mater. Sci. Eng. A*, vol. 397, no. 1–2, pp. 376–384, 2005.

[40] R. Ramesh, I. Dinaharan, R. Kumar, and E. T. Akinlabi, "Microstructure and mechanical characterization of friction stir welded high strength low alloy steels," *Mater. Sci. Eng. A*, vol. 687, pp. 39–46, 2017.

[41] L. Wei and T. W. Nelson, "Correlation of Microstructures and Process Variables in FSW HSLA-65 Steel," *Weld. J.*, vol. 90, pp. 95–101, 2011.

[42] G. Sorger, E. Lehtimäki, S. Hurme, H. Remes, P. Vilaça, and L. Molter, "Microstructure and fatigue properties of friction stir welded high-strength steel plates," *Sci. Technol. Weld. Join.*, vol. 1718, pp. 1–7, 2017.

[43] H. H. Cho *et al.*, "Microstructural evolution in friction stir welding of high-strength linepipe steel," *Mater. Des.*, vol. 34, pp. 258–267, 2012.

[44]   T. F. A. Santos, T. F. C. Hermenegildo, C. R. M. Afonso, R. R. Marinho, M. T. P. Paes, and A. J. Ramirez, "Fracture toughness of ISO 3183 X80M (API 5L X80) steel friction stir welds," *Eng. Fract. Mech.*, vol. 77, no. 15, pp. 2937–2945, Oct. 2010.

[45]   N. Rahimi, R. A. Pax, and E. M. Gray, "Review of functional titanium oxides. I: TiO2 and its modifications," *Prog. Solid State Chem.*, vol. 44, no. 3, pp. 86–105, 2016.

[46]   A. Weir, P. Westerhoff, L. Fabricius, and N. von Goetz, "Titanium Dioxide Nanoparticles in Food and Personal Care Products," *Environ. Sci. Technol.*, vol. 46, no. 4, pp. 2242–2250, 2012.

[47]   "LIST OF UV FILTERS ALLOWED IN COSMETIC PRODUCTS," 2018. [Online]. Available: http://ec.europa.eu/growth/tools-databases/cosing/pdf/COSING_Annex VI_v2.pdf. [Accessed: 11-May-2018].

[48]   S. Nafisi and H. I. Maibach, "Nanotechnology in Cosmetics," in *Cosmetic Science and Technology*, vol. 1, no. 3, Elsevier, 2017, pp. 337–369.

[49]   J. Zhang, P. Zhou, J. Liu, and J. Yu, "New understanding of the difference of photocatalytic activity among anatase, rutile and brookite TiO $_2$," *Phys. Chem. Chem. Phys.*, vol. 16, no. 38, pp. 20382–20386, 2014.

[50]   C. Chen, H. Xue, H. Peng, L. Yan, L. Zhi, and S. Wang, "Inclusions and microstructure of steel weld deposits with nanosize titanium oxide addition," *J. Nanomater.*, vol. 2014, 2014.

[51]   M. N. Ilman, R. C. Cochrane, and G. M. Evans, "Effect of titanium and nitrogen on the transformation characteristics of acicular ferrite in reheated C-Mn steel weld metals," *Weld. World*, vol. 58, no. 1, pp. 1–10, 2014.

[52]   H. F. Al Hajeri, C. I. Garcia, M. Hua, and A. J. De Ardo, "Particle-stimulated Nucleation of Ferrite in Heavy Steel Sections," *ISIJ Int.*, vol. 46, no. 8, pp. 1233–1240, 2006.

[53]   G. Thewlis, J. A. Whiteman, and D. J. Senogles, "Dynamics of austenite to ferrite phase transformation in ferrous weld metals," *Mater. Sci. Technol.*, vol. 13, no. 3, pp. 257–274, Mar. 1997.

[54] K. Hui *et al.*, "The mechanism of intragranular acicular ferrite nucleation induced by Mg-Al-O inclusions," *Adv. Mater. Sci. Eng.*, vol. 2015, pp. 1–7, 2015.

[55] J. S. Seo, C. Lee, and H. J. Kim, "Influence of Oxygen Content on Microstructure and Inclusion Characteristics of Bainitic Weld Metals," *ISIJ Int.*, vol. 53, no. 2, pp. 279–285, 2013.

[56] Z. Zhang and R. A. Farrar, "Role of non-metallic inclusions in formation of acicular ferrite in low alloy weld metals," *Mater. Sci. Technol.*, vol. 12, no. 3, pp. 237–260, Mar. 1996.

[57] F. J. Barbaro, P. Krauklis, and K. E. Easterling, "Formation of acicular ferrite at oxide particles in steels," *Mater. Sci. Technol.*, vol. 5, no. 11, pp. 1057–1068, 1989.

[58] D. B. Murphy and M. W. Davidson, *Fundamentals of Light Microscopy and Electronic Imaging*. Wiley, 2012.

[59] D. Payne, "Use and limitations of light microscopy for diagnosing malaria at the primary health care level.," *Bull. World Health Organ.*, vol. 66, no. 5, pp. 621–626, 1988.

[60] D. B. Murphy and M. W. Davidson, *Fundamentals of Light Microscopy and Electronic Imaging*. Wiley, 2012.

[61] M. J. Rust, M. Bates, and X. Zhuang, "Sub-diffraction-limit imaging by stochastic optical reconstruction microscopy (STORM)," *Nat. Methods*, vol. 3, no. 10, pp. 793–796, Oct. 2006.

[62] L. G. Chen, J. Warner, A. I. Kirkland, F. R. Chen, and D. Van Dyck, "Snapshot 3D Electron Imaging of Structural Dynamics," *Sci. Rep.*, vol. 7, no. 1, pp. 4–10, 2017.

[63] W. Zhou and Z. L. Wang, *Scanning Microscopy for Nanotechnology: Techniques and Applications*. Springer New York, 2007.

[64] J. C. Russ, M. A. Frs, R. Kiessling, and J. Charles, *Fundamentals of Energy Dispersive X-Ray Analysis: Butterworths Monographs in Materials*, Revised. Butterworth-Heinemann, 2013.

[65] A. J. Schwartz, M. Kumar, B. L. Adams, and D. P. Field, *Electron Backscatter Diffraction in Materials Science*. Springer US, 2013.

[66] S. W. Paddock, *Confocal Microscopy: Methods and Protocols*. Springer Science & Business Media, 1999.

[67] P. M. Conn, *Techniques in Confocal Microscopy*. Academic Press, 2010.

[68] Y. Komizo and H. Terasaki, "Optical observation of real materials using laser scanning confocal microscopy Part 1 – techniques and observed examples of microstructural changes," *Sci. Technol. Weld. Join.*, vol. 16, no. 1, pp. 56–60, 2011.

[69] W. M. Thomas, E. D. Nicholas, J. C. Needham, M. G. Murch, P. Temple-Smith, and C. J. Dawes, "Friction welding," 1991.

[70] A. Kumar, A. S. Karur, S. Chipli, and A. Singh, "Optimization of FSW Parameters to Improve the Mechanical Properties of AA2024-T351 Similar Joints Using Taguchi Method," *J. Mech. Eng. Autom.*, vol. 5, no. 3B, pp. 27–32, 2015.

[71] R. S. Mishra and Z. Y. Ma, "Friction stir welding and processing," *Mater. Sci. Eng. R Reports*, vol. 50, no. 1–2, pp. 1–78, 2005.

[72] S. Zou *et al.*, "Multi-Track Friction Stir Lap Welding of 2024 Aluminum Alloy: Processing, Microstructure and Mechanical Properties," *Metals (Basel).*, vol. 7, no. 1, p. 1, 2016.

[73] J. Azevedo, L. Quintino, V. Infante, R. M. Miranda, and J. dos Santos, "Friction stir welding of shipbuilding steel with primer," *Soldag. e Insp.*, vol. 21, no. 1, pp. 16–29, 2016.

[74] T. Weinberger, "Process and tool Development for Friction Stir Welding of Steel," Graz University of Technology, 2010.

[75] P. L. Threadgill, A. J. Leonard, H. R. Shercliff, and P. J. Withers, "Friction stir welding of aluminium alloys," *Int. Mater. Rev.*, vol. 54, no. 2, pp. 49–93, 2009.

[76] F. Fadaeifard, F. Gharavi, K. A. Matori, A. R. Daud, M. K. A. M. Ariffin, and M. Awang, "Investigation of Microstructure and Mechanical Properties of Friction Stir Lap Welded AA6061-T6 in Various Welding Speeds," *J. Appl. Sci.*, vol. 14, no. 3, pp. 221–228, 2014.

[77] TWI, "Stationary shoulder friction stir welding - Lap weld." [Online]. Available: https://www.youtube.com/watch?v=Yx5SVQTfTzU. [Accessed: 09-Apr-2016].

[78] R. E. D. Wayne M. Thomas, "Friction Stir Welding Developments," in *6TH International Conference on Trends in Welding Research*, 2002.

[79] A. G. THOMAS and H. J. JONES, "Hot Pressing of Ceramic Powders," *Powder Metall.*, vol. 3, no. 6, pp. 160–169, 1960.

[80] L. A. Dobrzanski, A. D. Dobrzanska-Danikiewicz, A. Achtelik-Franczak, L. B. Dobrzanski, E. Hajduczek, and G. Matula, "Fabrication Technologies of the Sintered Materials Including Materials for Medical and Dental Application," in *Powder Metallurgy - Fundamentals and Case Studies*, InTech, 2017, pp. 17–52.

[81] J. Favre, Y. Koizumi, A. Chiba, D. Fabregue, and E. Maire, "Deformation behavior and dynamic recrystallization of biomedical Co-Cr-W-Ni (L-605) alloy," *Metall. Mater. Trans. A Phys. Metall. Mater. Sci.*, vol. 44, no. 6, pp. 2819–2830, 2013.

[82] TMS, J. Favre, Y. Koizumi, A. Chiba, D. Fabregue, and E. Maire, "Recrystallization of L-605 Cobalt Superalloy during Hot-Working Process," *3rd Int. Symp. High-Temperature Metall. Process.*, pp. 257–264, 2012.

[83] "Device outline ThermecmasterZ." [Online]. Available: http://www.nsst.nssmc.com/technology/metallurgy/metallurgy03/. [Accessed: 27-Apr-2018].

[84] "Hot deformation simulator (Thermec Master-Z)." [Online]. Available: http://www.chibalab.imr.tohoku.ac.jp/english/equipment/index.html. [Accessed: 09-Apr-2018].

[85] L. B. Godefroid, L. C. Cândido, R. V. B. Toffolo, and L. H. S. Barbosa, "Microstructure and mechanical properties of two Api steels for iron ore pipelines," *Mater. Res.*, vol. 17, no. suppl 1, pp. 114–120, 2014.

[86] R. Ghomashchi, W. Costin, and R. Kurji, "Evolution of weld metal microstructure in shielded metal arc welding of X70 HSLA steel with cellulosic electrodes: A case study," *Mater. Charact.*, vol. 107, pp. 317–326, 2015.

[87] RSC - Advancing the Chemical Sciences, "TiO2 : Manufacture of Titanium Dioxide," *R. Soc. Chem.*, no. 207890, p. 5, 2016.

[88] U.S. Environmental Protection Agency, "Titanium tetrachloride production by the chloride ilmenite process," 1995.

[89] K.-H. Tseng and K.-L. Chen, *Comparisons between TiO2- and SiO2-flux assisted TIG welding processes*, vol. 12. 2012.

[90] M. Majid and R. K. Phanden, "Effect of TiO 2 Addition in Saw Flux on Mechanical Properties of AISI 1020 Welds Groove face Root opening Root face," vol. 2, no. 7, pp. 1085–1091, 2015.

[91] S. Balos, L. Sidjanin, M. Dramicanin, D. Labus, B. Pilic, and M. Jovicic, "Modification of cellulose and rutile welding electrode coating by infiltrated TiO2nanoparticles," *Met. Mater. Int.*, vol. 22, no. 3, pp. 509–518, 2016.

[92] Indian Bureau of Mines, "Indian Minerals Yearbook 2015," *Indian Miner. Yearb. 2015 (Part-III Miner. Rev.*, vol. 54th Editi, pp. 1–9, 2016.

[93] "Products." [Online]. Available: http://www.ama-co.com/95/Products.aspx. [Accessed: 14-Apr-2018].

[94] K. Yamada, M. Saito, R. Ohashi, T. Nakai, K. Deguchi, and T. Shimizu, "Solid-state 47/49 Ti Nuclear Magnetic Resonance of TiO 2," *Chem. Lett.*, vol. 43, no. 9, pp. 1520–1521, Sep. 2014.

[95] "physical characteristics of rutile." [Online]. Available: https://vvmineralblog.wordpress.com/2014/04/17/physical-characteristics-of-rutile/. [Accessed: 06-Apr-2016].

[96] S. C. Liao, W. E. Mayo, and K. D. Pae, "Theory of high pressure/low temperature sintering of bulk nanocrystalline TiO2," *Acta Mater.*, vol. 45, no. 10, pp. 4027–4040, 1997.

[97] I. Malsch and C. Emond, *Nanotechnology and Human Health*. CRC Press, 2016.

[98] T. D. S. Antonino, P. B. Guimarães, R. D. A. Alécio, Y. P. Yadava, R. Artur, and S. Ferreira, "Measurements of the Thermophysical Properties of the API 5L X80," *Mater. Sci. Appl.*, vol. 5, no. June, pp. 617–627, 2014.

[99] "Titanium Dioxide." [Online]. Available: https://www.azom.com/properties.aspx?ArticleID=1179. [Accessed: 02-Jul-2018].

[100] C. J. McHargue, J. B. Darby, M. J. Yacamán, and J. R. Gasga, *Synthesis and Properties of Advanced Materials*. Springer US, 2013.

[101] B. Basu and K. Balani, *Advanced Structural Ceramics*. Wiley, 2011.

[102] "Tungsten Carbide - An Overview (visited 02.04.2018)," *https://www.azom.com/properties.aspx?ArticleID=1203*.

[103] H. T. Angus, *Cast Iron: Physical and Engineering Properties*. Elsevier Science, 2013.

[104] H. O. Pierson, *Handbook of Refractory Carbides and Nitrides: Properties, Characteristics, Processing and Applications*. Elsevier Science, 1996.

[105] A. S. Kurlov and A. I. Gusev, "Tungsten carbides and W-C phase diagram," *Inorg. Mater.*, vol. 42, no. 2, pp. 121–127, 2006.

[106] *Sintering Technology*. Taylor & Francis, 1996.

[107] H. M. Yang, "Continuous cooling transformation behavior of X70 pipeline steel," *Adv. Mater. Res.*, vol. 690, pp. 2205–2209, 2013.

7. Appendix

7.1. Microstructure overview across the welding zone

To choose an optimal region for EBSD of sample B, both the microstructure of both samples sample A and sample B were analyzed via LOM across the weld, with exception of the regions mentioned of the center, which has already been analyzed. The results can be seen in Figure 60 and Figure 61.
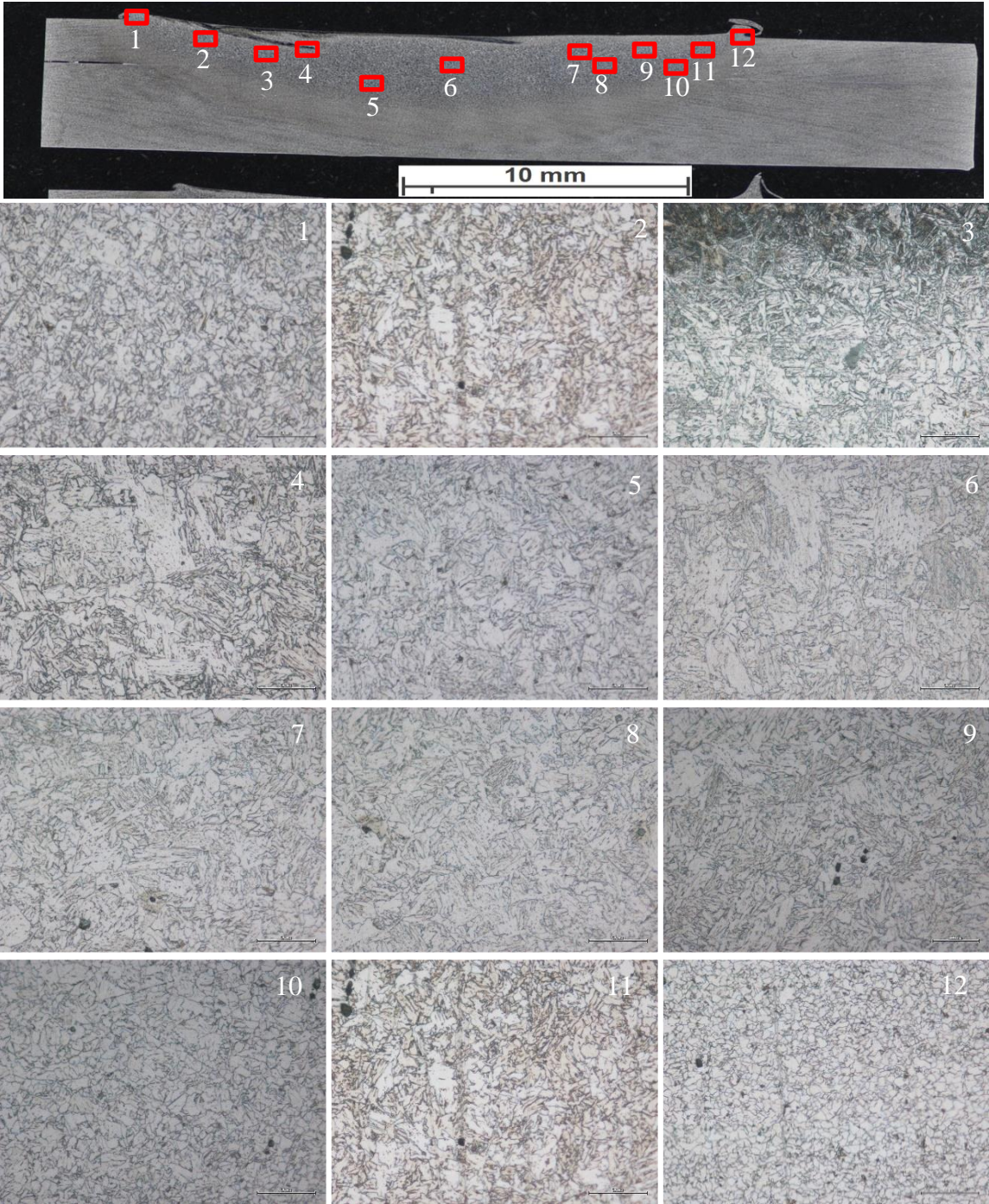
Figure 60 Overview of the Welding Zone for Reference sample with small grains on the edge (1- 2, 10-12), big grains in the Center (5, 6) and dendritic grains near WC (4)
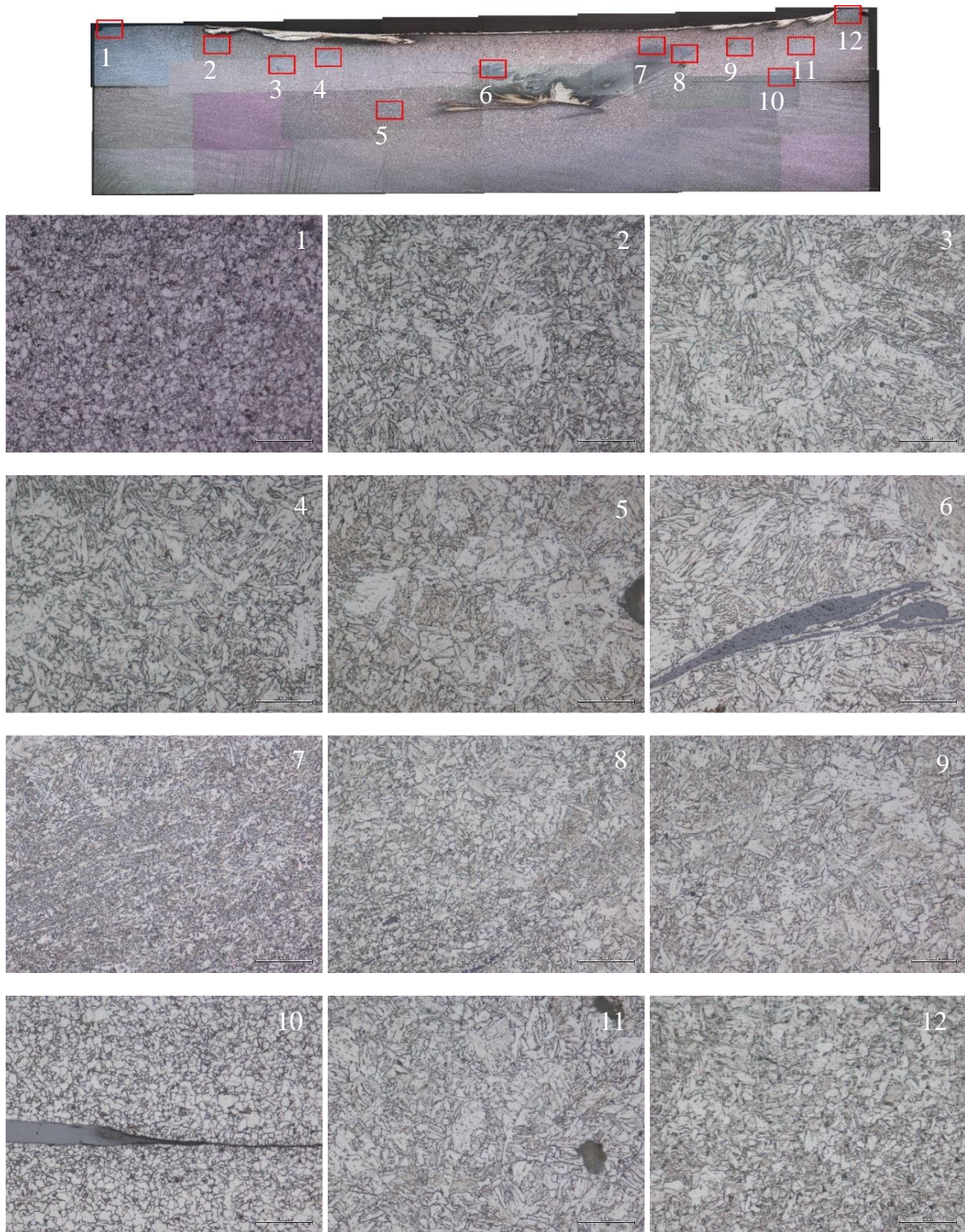
Figure 61 Overview of the Welding Zone for sample 2 with exception of the lower center, with small grains on the edge and outside (1- 2, 10-12), big grains around the Center (3-5), and titanium grains with ferrite rings in the center

7.2. Sample D inclusions

As mentioned in Section 4.3.4, the dark spots found in Sample D were analyzed via multiple spot scans (see Figure 62). No TiO_2 was found and the detected elements, primarily silicon and aluminum might be a result of the grinding and polishing process, as grinding was done with sandpaper and polishing with aluminum oxide suspensions. When comparing it with literature of a SMAW welded X70 steel without TiO_2 addition [86], a similar microstructure can be seen (See Figure 63) and is there theorized to be a result of contamination of the weld during the process either from the environment or from electrode components. Nevertheless, FSW does not result in a molten weld as with SMAW and the contamination by electrode covering is also not applicable to FSW as W was not detected. There is not enough data available to draw a definite conclusion concerning the origin of the inclusions or defects.
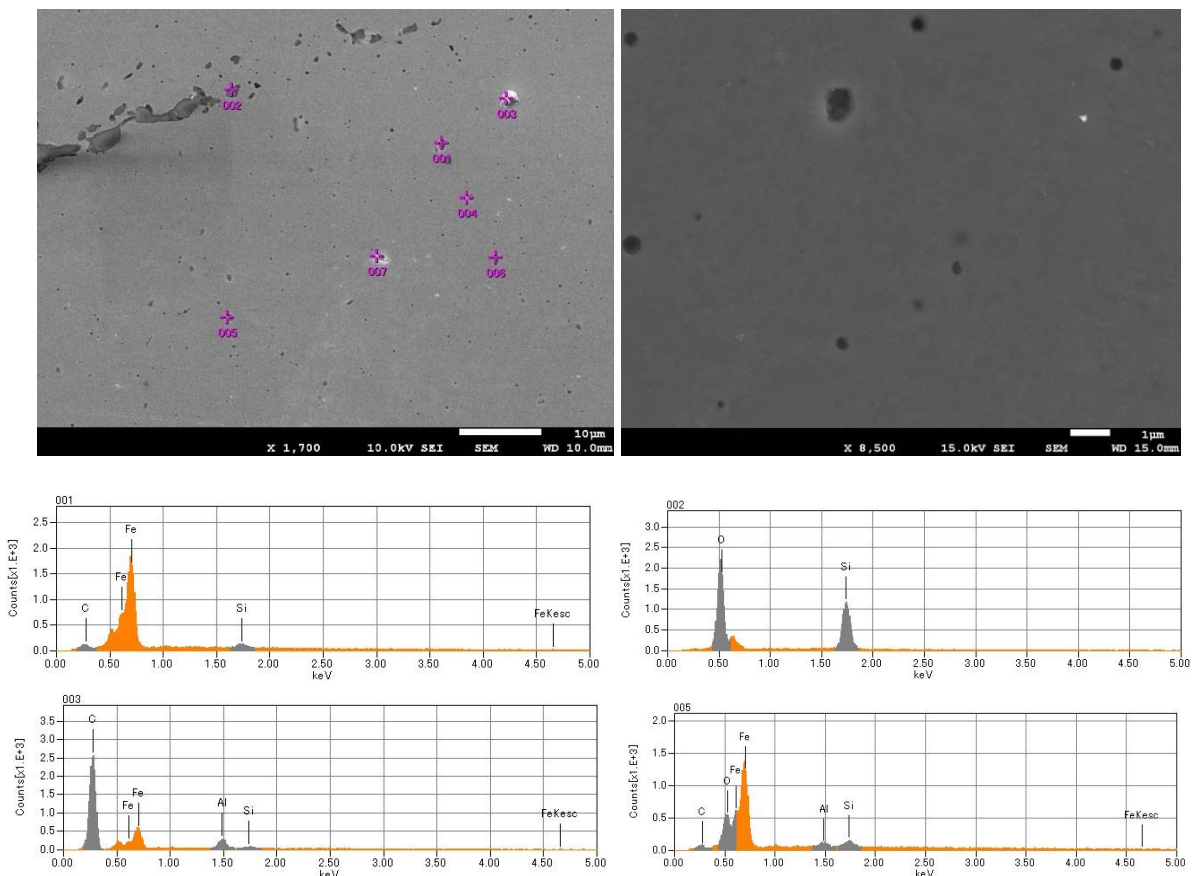
Figure 62 EDS (top left), close up (top right) and results (below) for dark spots in area with acicular ferrite. seem to be defects filled with silicon from grinding and Al from polishing

71
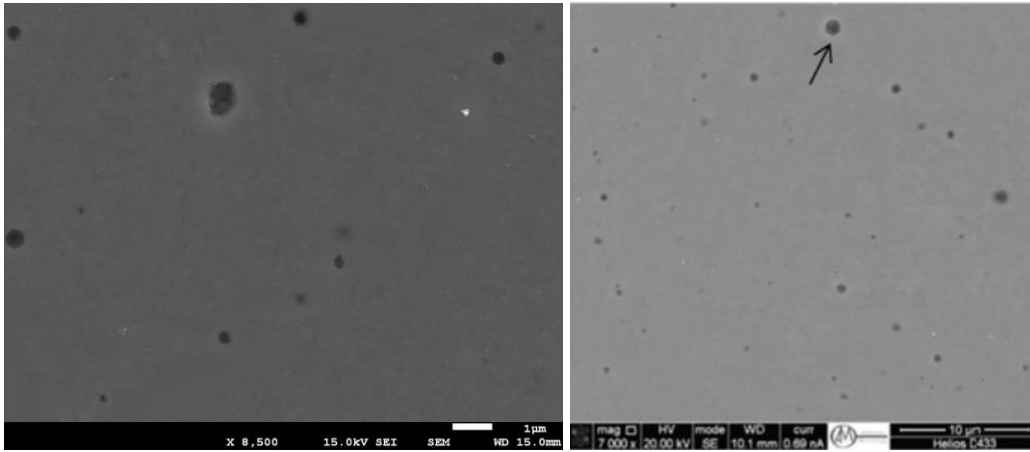
Figure 63 Comparison of the close-up of the dark spots with SMAW sample without TiO₂ from literature [18]

7.3.   TiO$_2$ EDS and XRD Results

The EDS analysis of TiO$_2$ was done using two different voltages, a surface analysis at lower voltage (see Figure 64) and a depth analysis using higher voltage (see Figure 65). The depth analysis shows that the iron impurities on TiO$_2$ particles are surface impurities, while the lighter colored particles do not contain Ti but a multitude of different elements including Al, Si, Zr and Fe. The XRD analysis (see Figure 66) shows that both brookite and anatase are not present in the rutile sand powder, instead it is rutile with impurities of other elements.
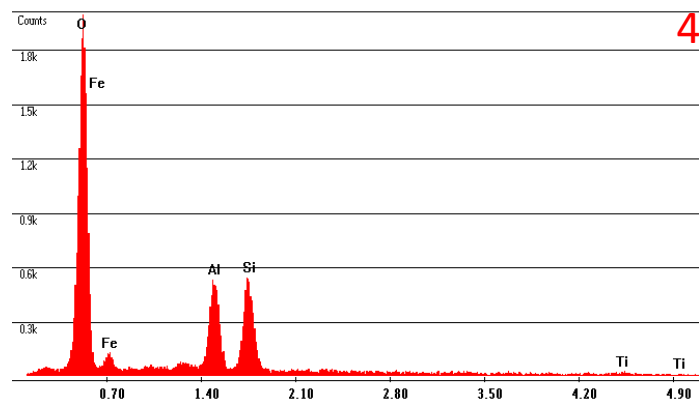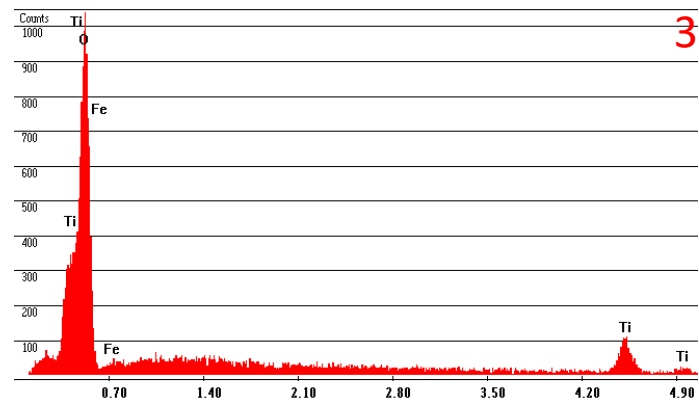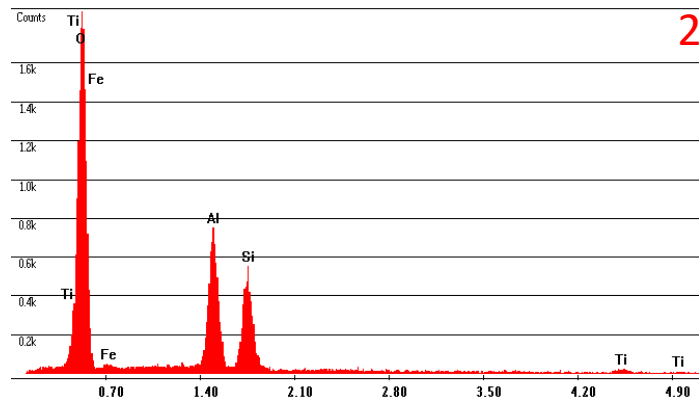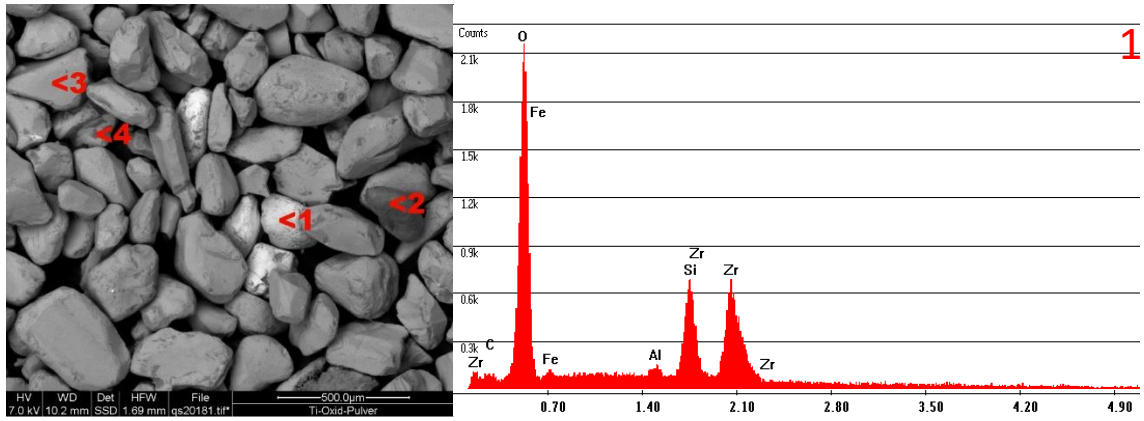
Figure 64 EDS (counts per keV) of rutile at 7kV
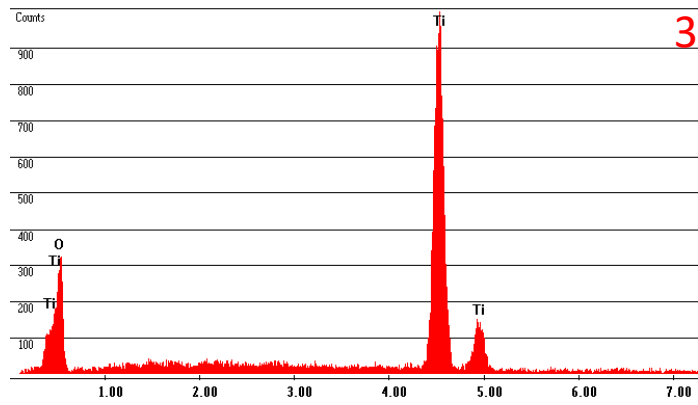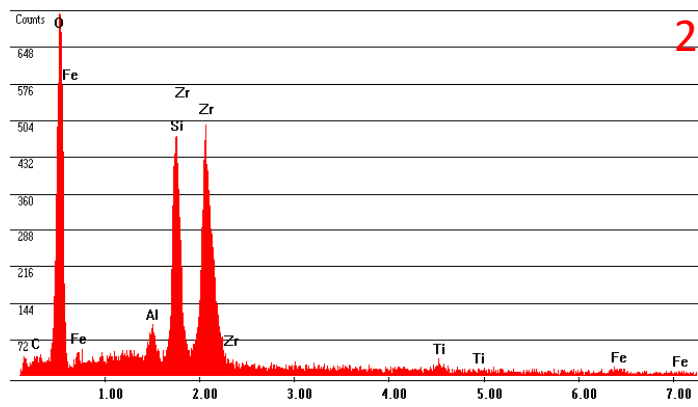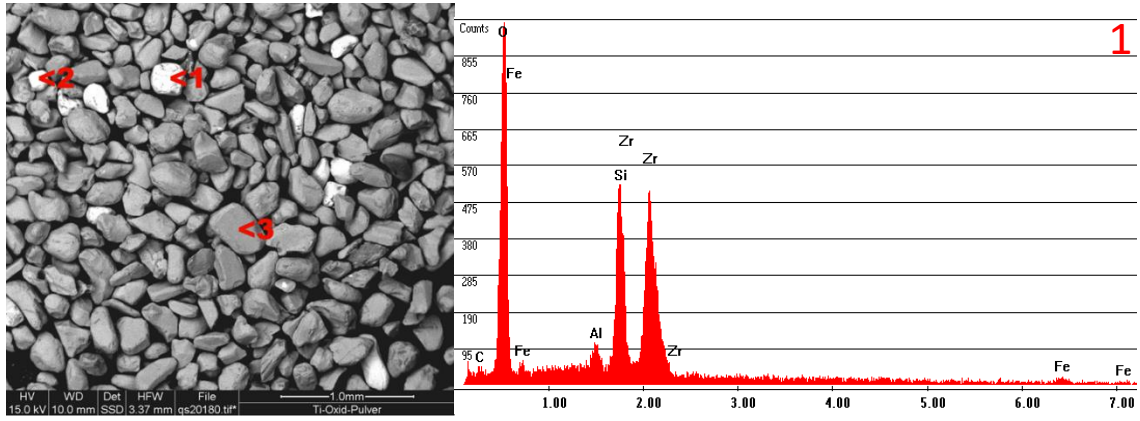
Figure 65 EDS (counts per keV) of rutile at 10kV
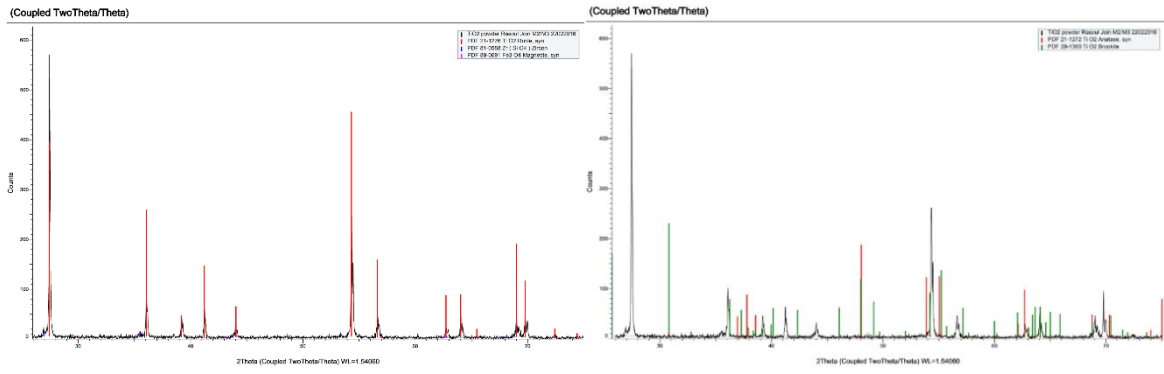
Figure 66 XRD of rutile sand, left for rutile (red) and right for anatase (red) and brookite (green)

7.4. Laser confocal microscopy trail run

The samples were prepared for analysis with laser confocal microscopy but LSCM process was never applied to Samples A-F. Instead the experiments were halted after two calibration runs to properly adjust heating and cooling times in which base material from samples not relevant to this thesis were used. These samples were not analyzed as the parameters were still being adjusted and the FSW temperature curve had not been fully emulated. The reason for the stop of the analysis was that the formation of acicular ferrite was the main focus of this thesis and the link between TiO_2 and acicular ferrite in FSW samples remains unclear. The sample region of sample B which contained globular ferrite was also not chosen for LSCM analysis due to time constraints.

7.5. Sample A-E selected figures in higher resolution and additional images

7.5.1. Sample A

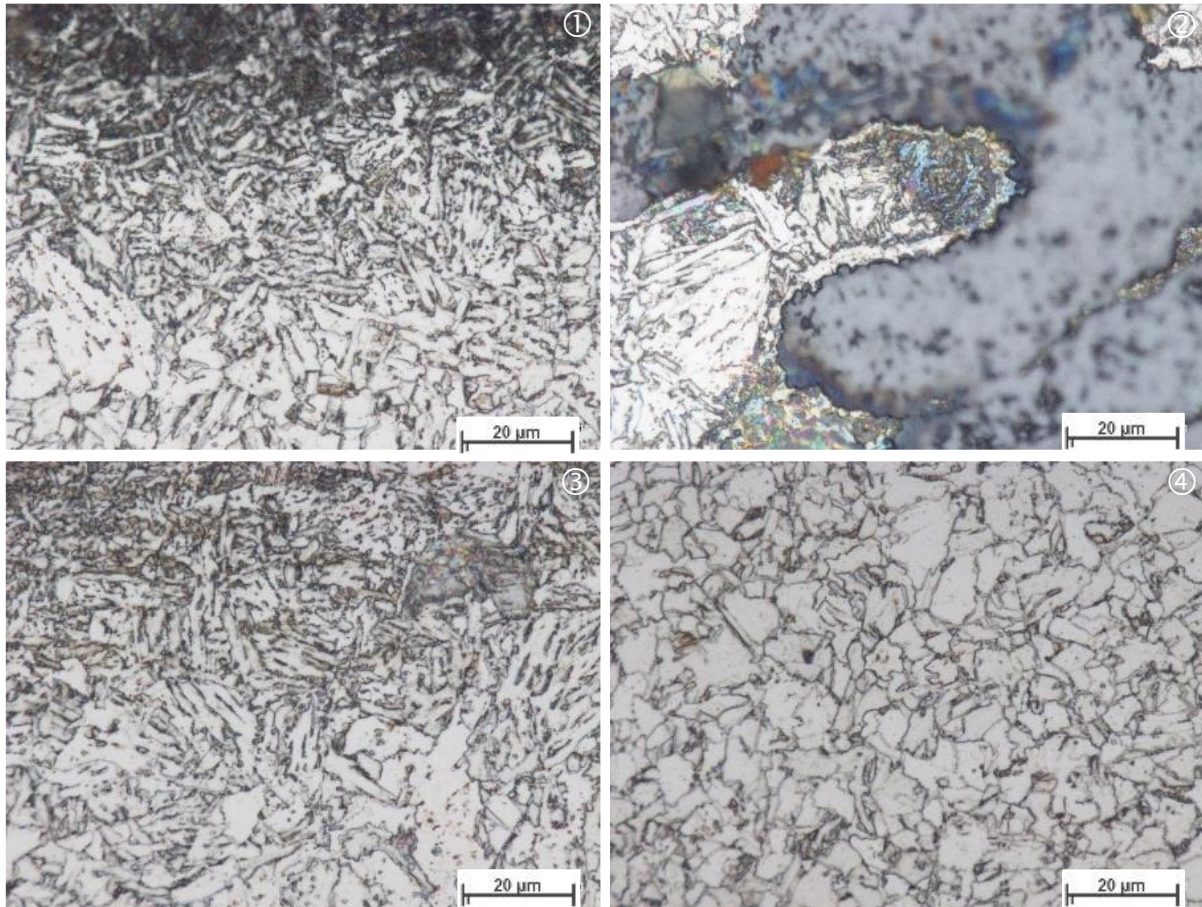Figure 67 shows the microstructure of the center of the sample in a higher resolution.
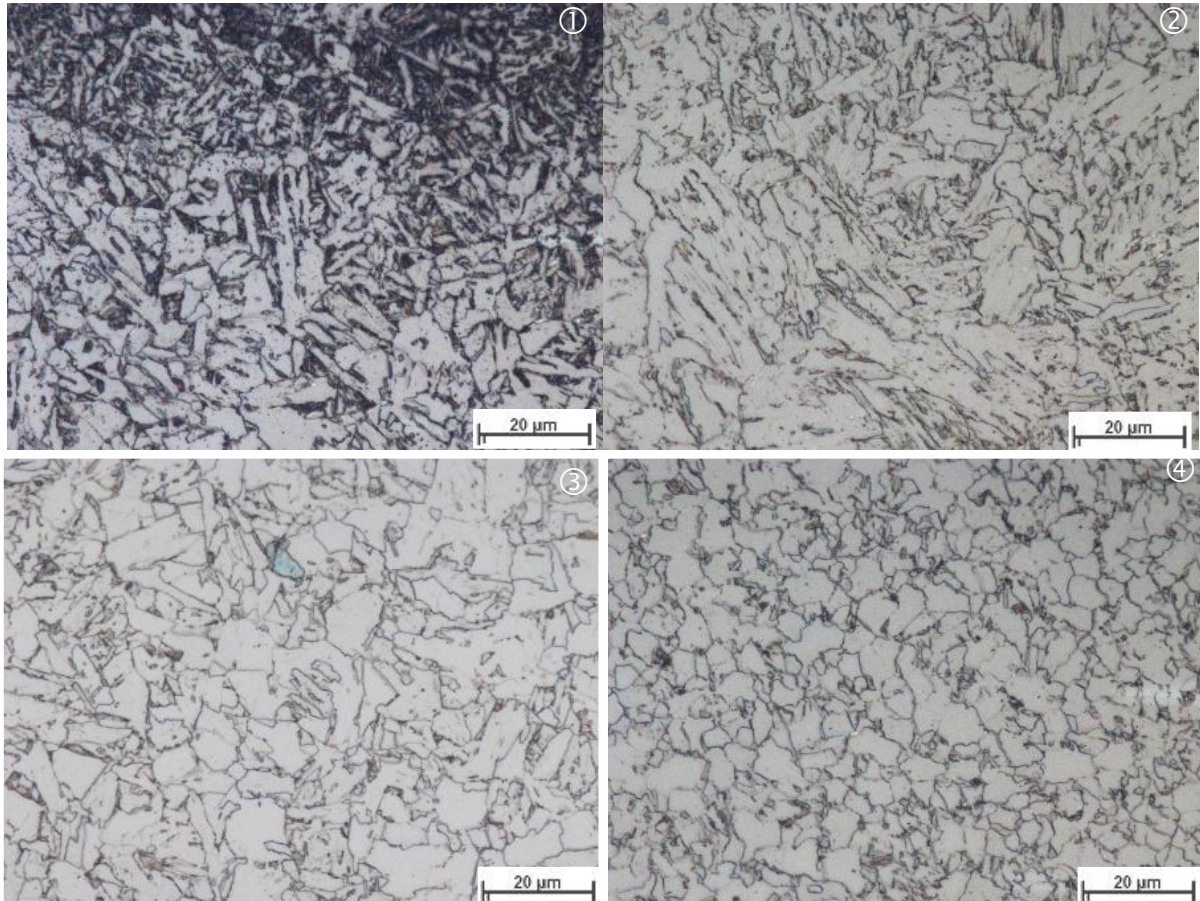
Figure 67 Sample A - LOM microstructure details: ① near surface close to WC abrasion, ② stir zone center and ③ below center, ④ base material outside HAZ

Figure 68 shows the region chosen for EBSD in LOM and SEM which has a bainitic microstructure and Figure 69 shows the 5 austenite grains in the measured region and the pole figures for each grain.
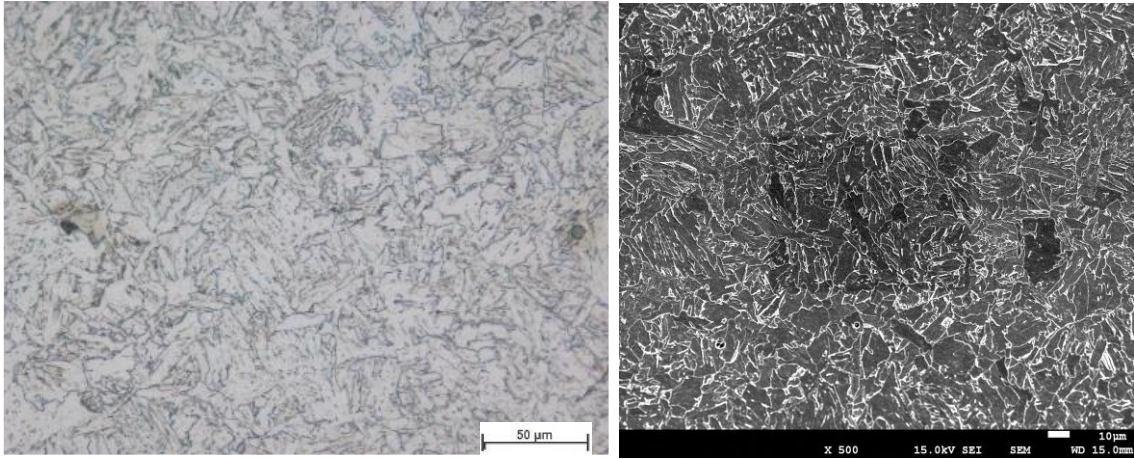
Figure 68 Sample A: EBSD analysis region LOM (left) and SEM (right)
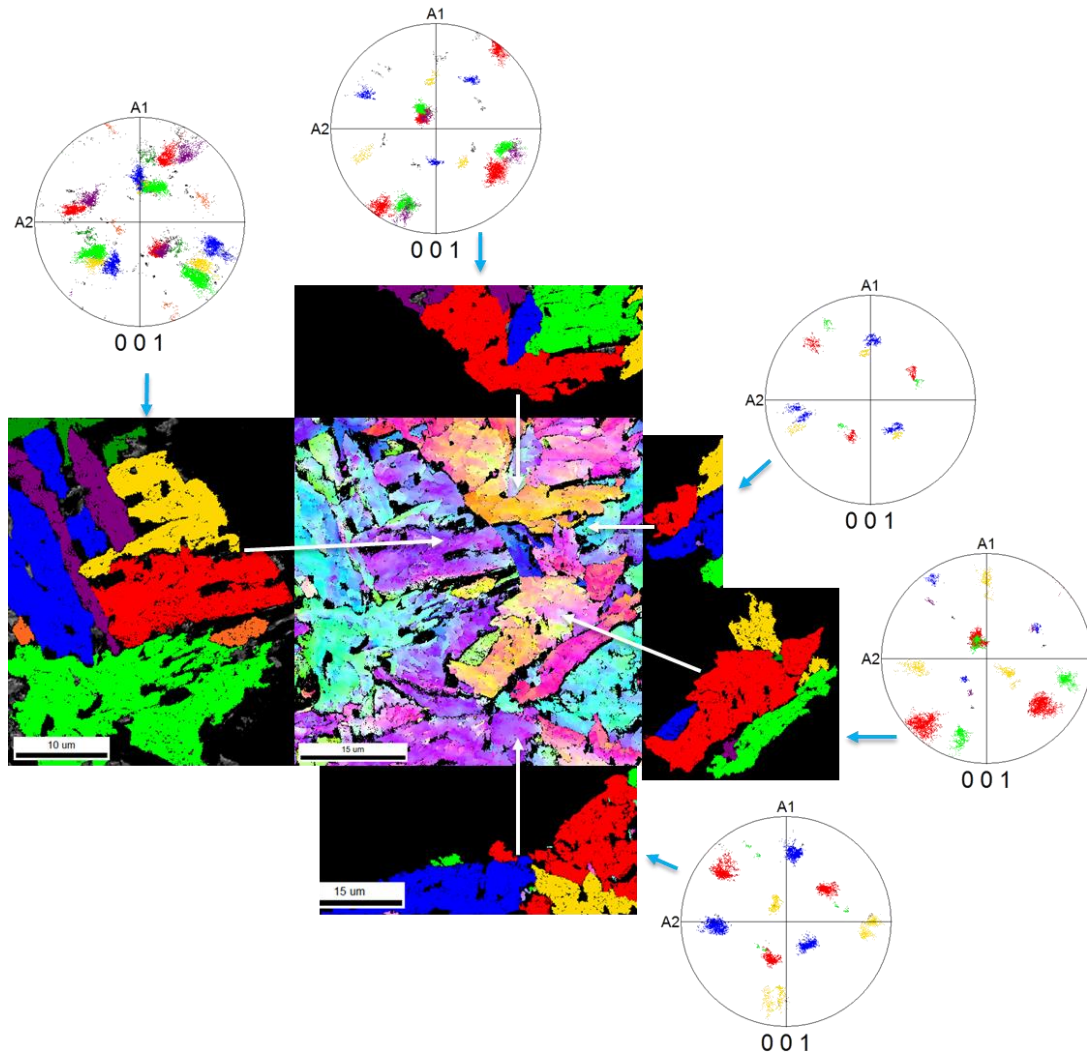
Figure 69 Sample A EBSD: region (center), austenite grains (black rectangles) and pol figures

Figure 70 show areas at the sample surface near WC abrasion which show an acicular microstructure.
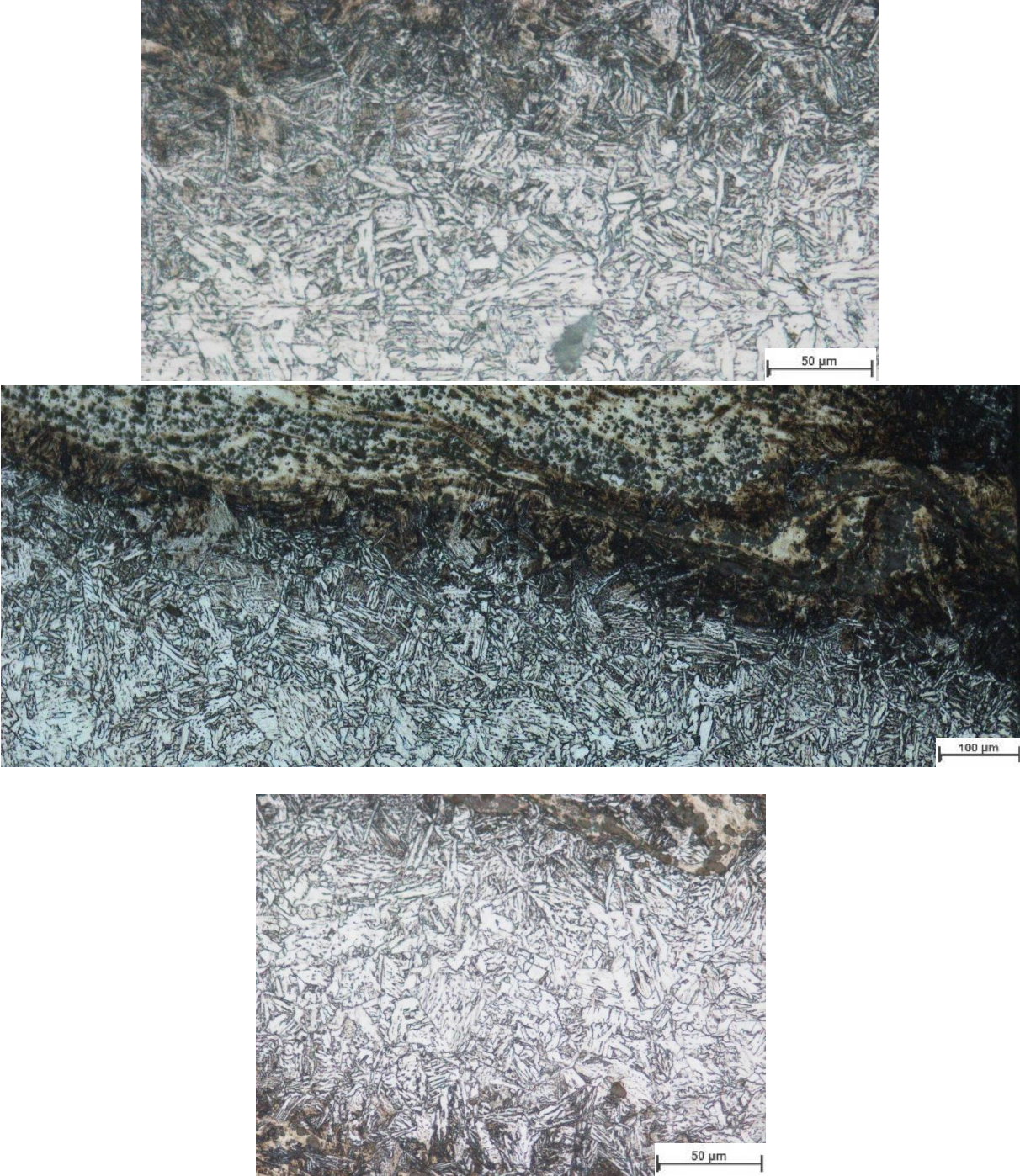
Figure 70 Acicular ferrite near WC abrasions (gold colored)

7.5.2. Sample B

Figure 71 shows the microstructure of the center of the sample in a higher resolution.

Figure 71 Sample B - LOM microstructure details: ① near surface close to WC abrasion, ② stir zone center and ③ below center, ④ outside TMAZ

Figure 72 and Figure 73 show an overview of the center of the weld, showing numerous TiO$_2$ agglomerations and tool abrasions.
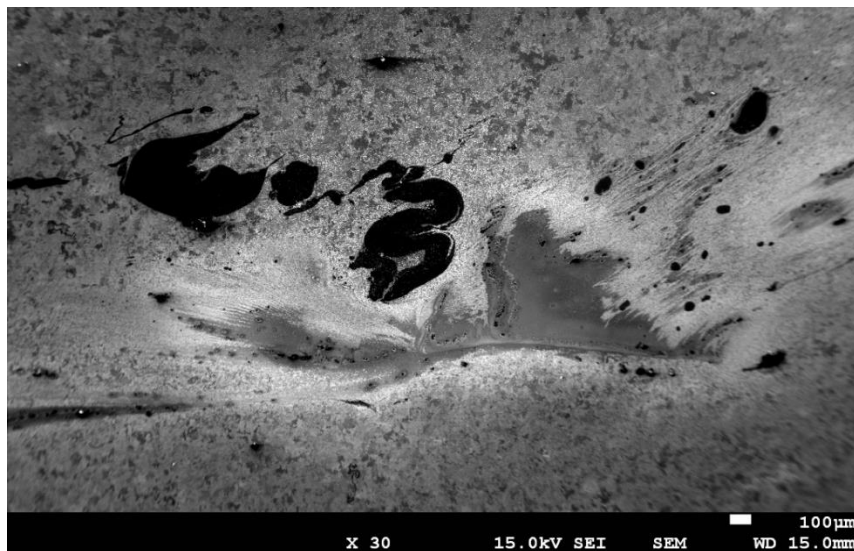
Figure 72 Sample B: SEM image showing TiO$_2$ (black) and WC (dark grey)
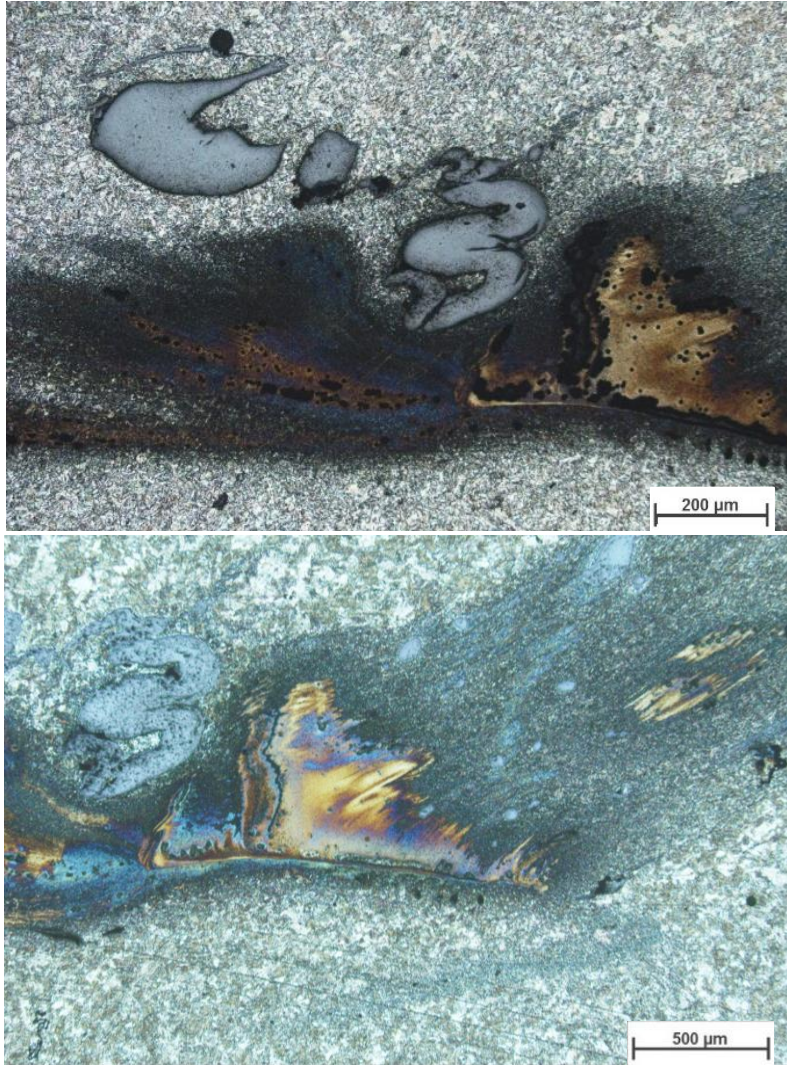
Figure 73 Sample B: overview of the center and center-right of sample B's nugget zone showing ferrite (white), TiO_2 (gray-blue) and WC (gold-tinting colored)

Figure 74 shows an overview of the microstructure between WC and TiO_2
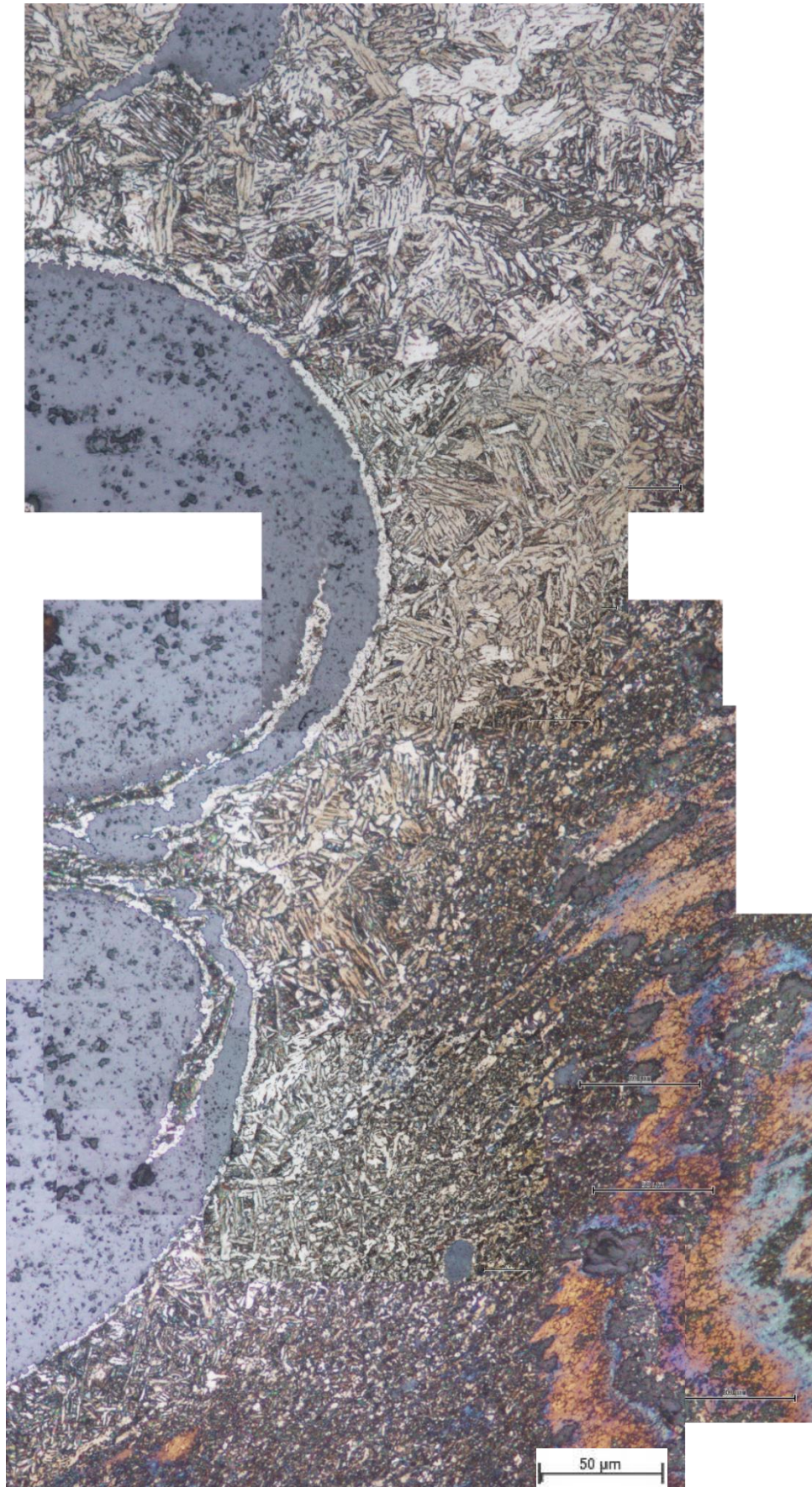
Figure 74 Overview area between WC (tinted, right) and TiO$_2$ (grey, left)

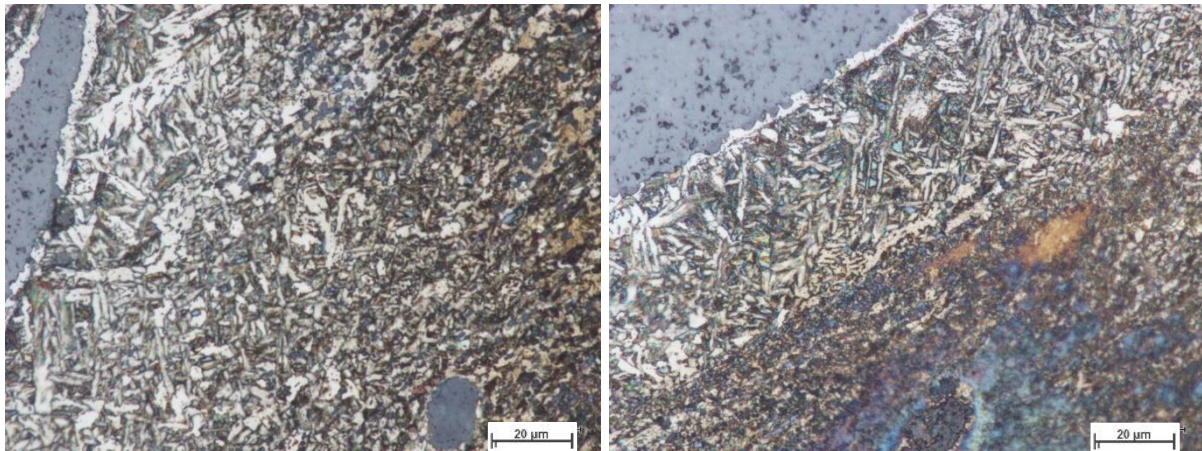Figure 75 shows 2 regions of Figure 74 with acicular ferrite, both close to or containing tool abrasions aside from TiO_2

Figure 75 Sample B section 3: Acicular ferrite, TiO_2 and WC for lower center (left image), lower left center (right image)

Figure 76 shows an EDS mapping of the region between TiO_2 and WC with a different color scheme as in Figure 46 and a linescan of the left image in Figure 75 showing a higher concentration of W than Ti.
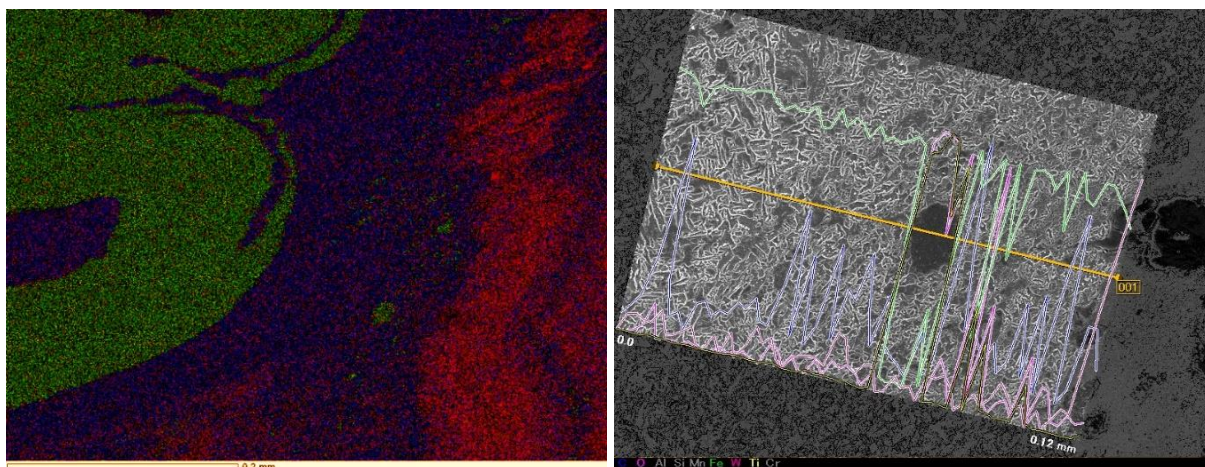
Figure 76 Sample B: EDS acicular ferrite region, green TiO_2, blue Fe, red WC (left image) and linescan (right image)

Figure 77 shows an acicular microstructure below the tool abrasion but without TiO_2 being present in this region
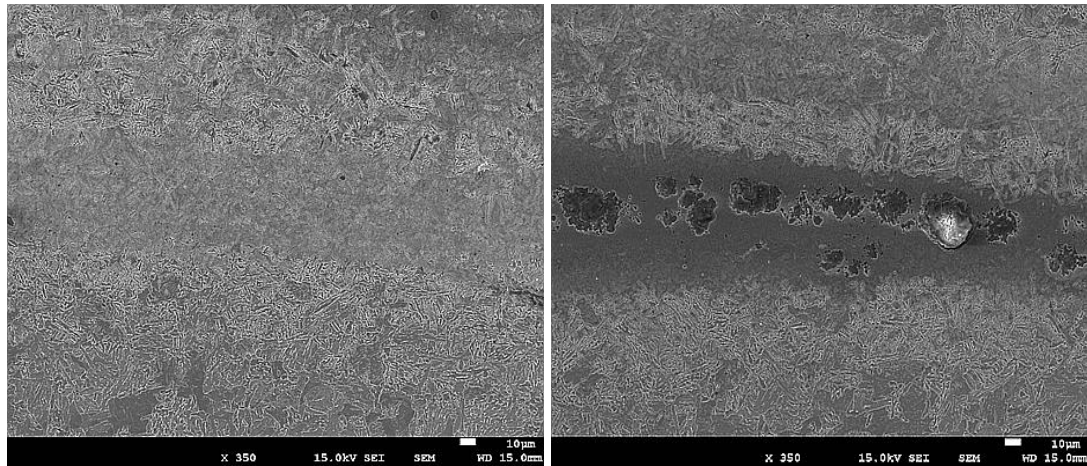
Figure 77 Sample B section 3: acicular ferrite near WC

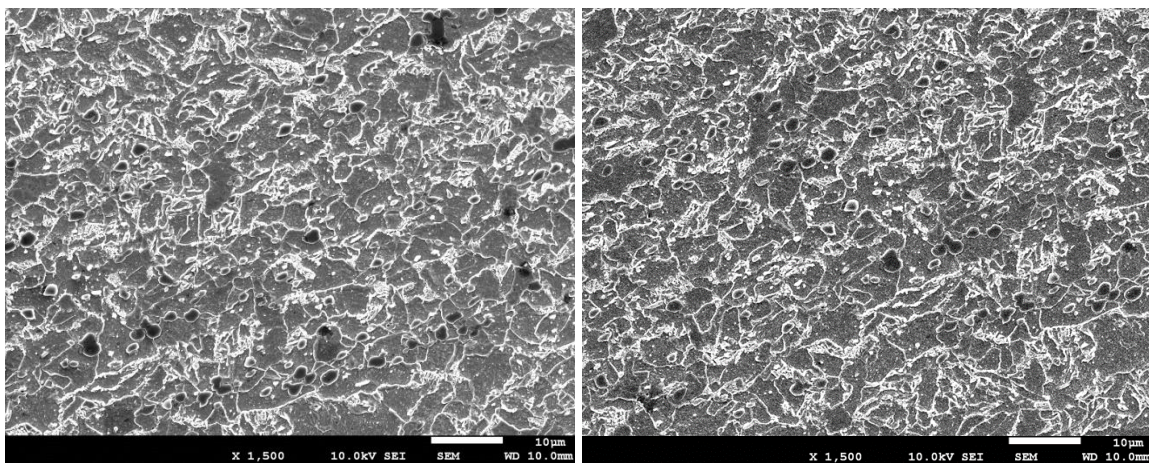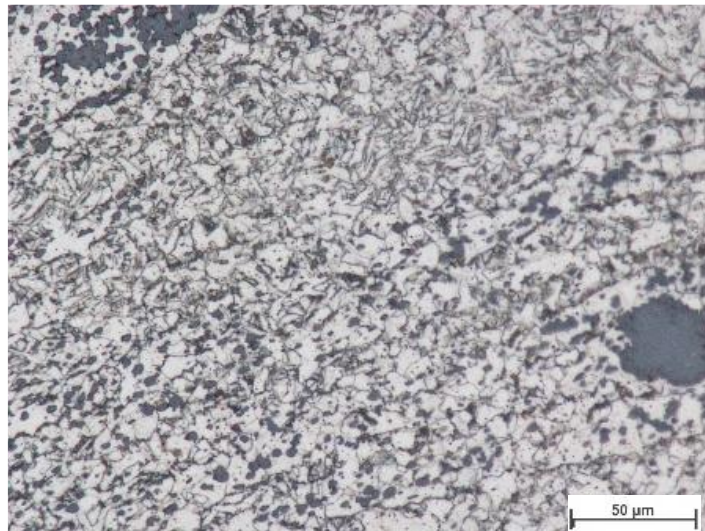Figure 78 shows the region chosen for EBSD in LOM and SEM with a globular ferrite microstructure

Figure 78 Sample B section 4: LOM and SEM images of EBSD scanned area

Figure 79 shows TiO_2 stuck between both plates as a result of the setup of the FSW process or the process itself.
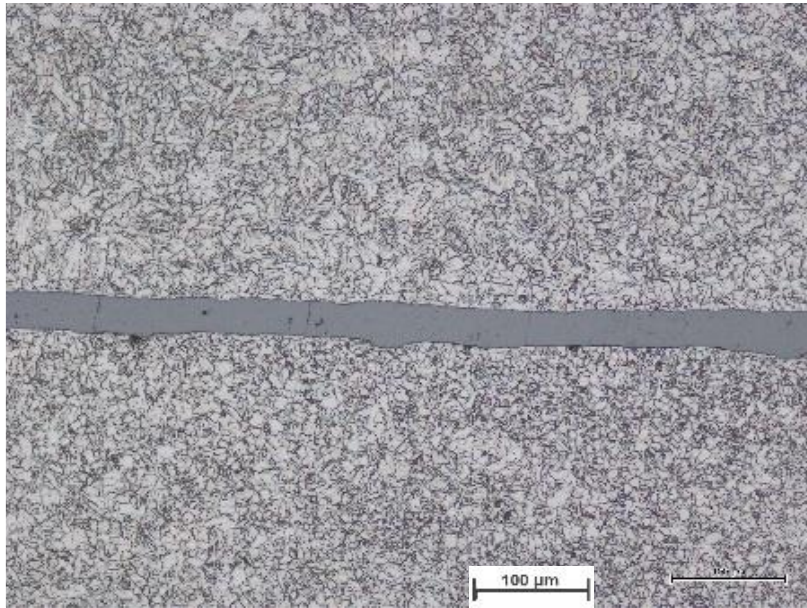
Figure 79 Sample B: TiO$_2$ between the plates

7.5.3. Sample C

Figure 80 shows an overview of the center of the sample with the gray particle in the center being TiO$_2$ and the golden areas covering the surface and center being tool abrasion.

Figure 80 Sample C: Overview center of the weld showing a distinct pattern, TiO$_2$ (grey) and tool abrasion (gold color)

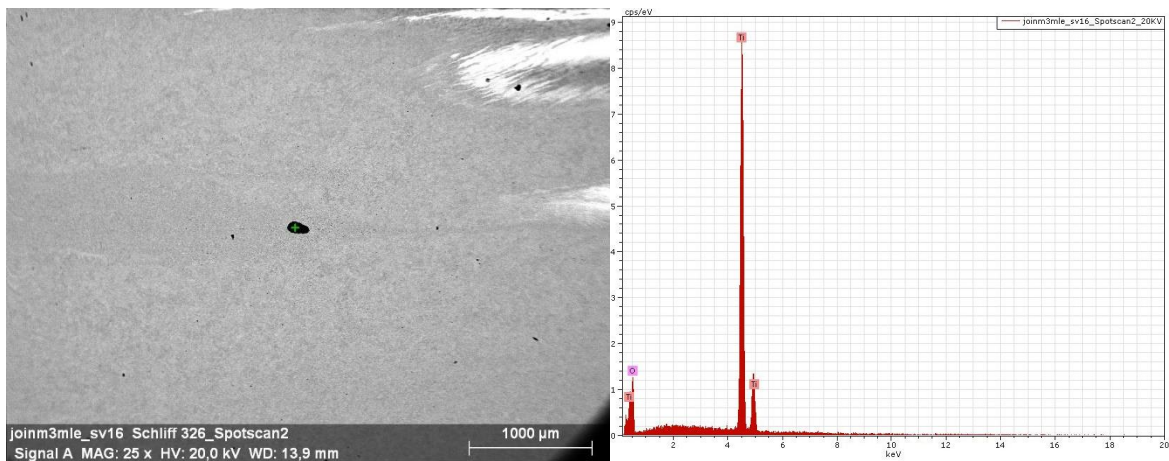Figure 81 shows an EDS point scan and the composition of the TiO$_2$ grain.

Figure 81 Sample C: EDS point scan of the TiO$_2$ particle, Ti red, O, purple

Figure 82 shows the microstructure of the center of the sample in a higher resolution.
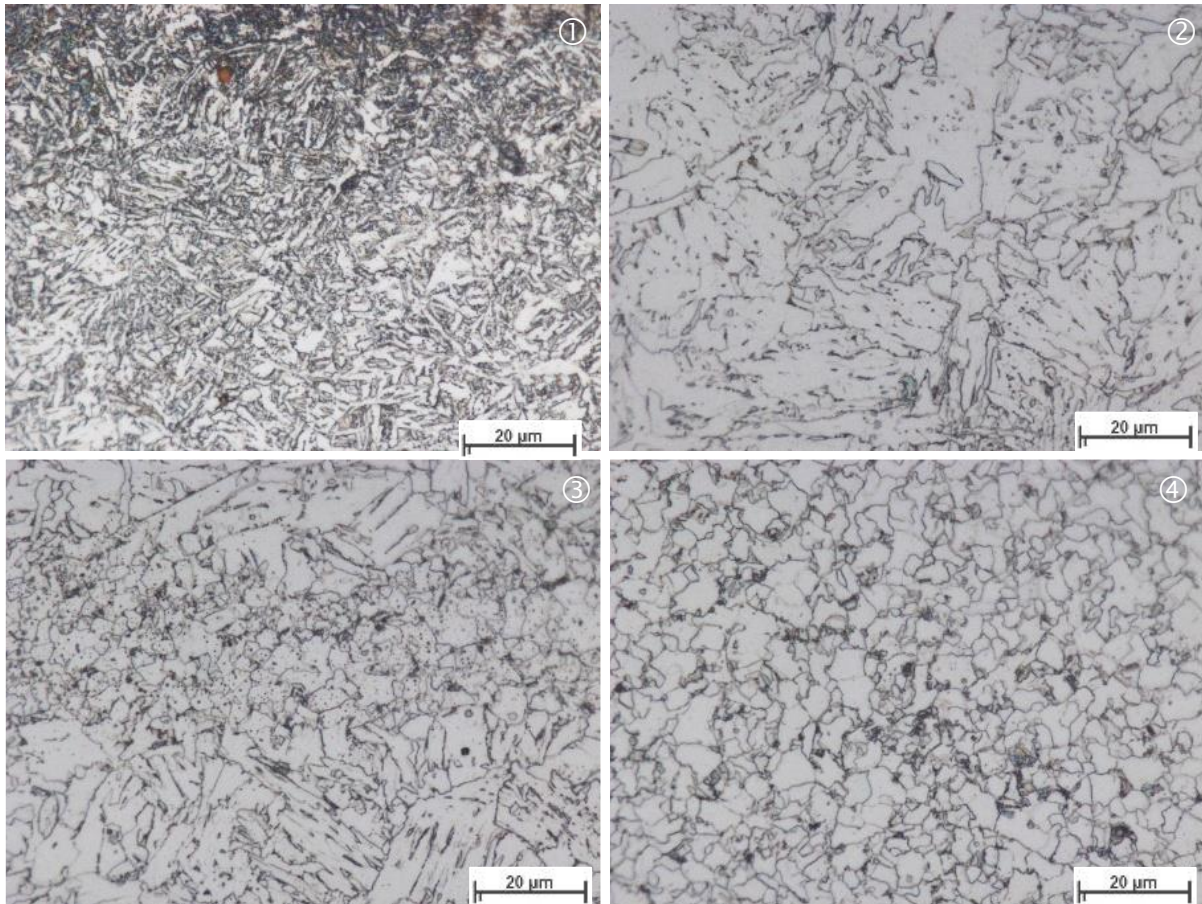
Figure 82 Sample C - LOM microstructure details: ① near surface close to WC abrasion, ② stir zone center and ③ below center, ④ outside TMAZ

Figure 83 shows the TiO₂ particle etched and unetched, the latter showing either inclusions or defects. Figure 84 shows the area at a lower magnification with the defects or inclusions being present and causing the pattern seen in Figure 85
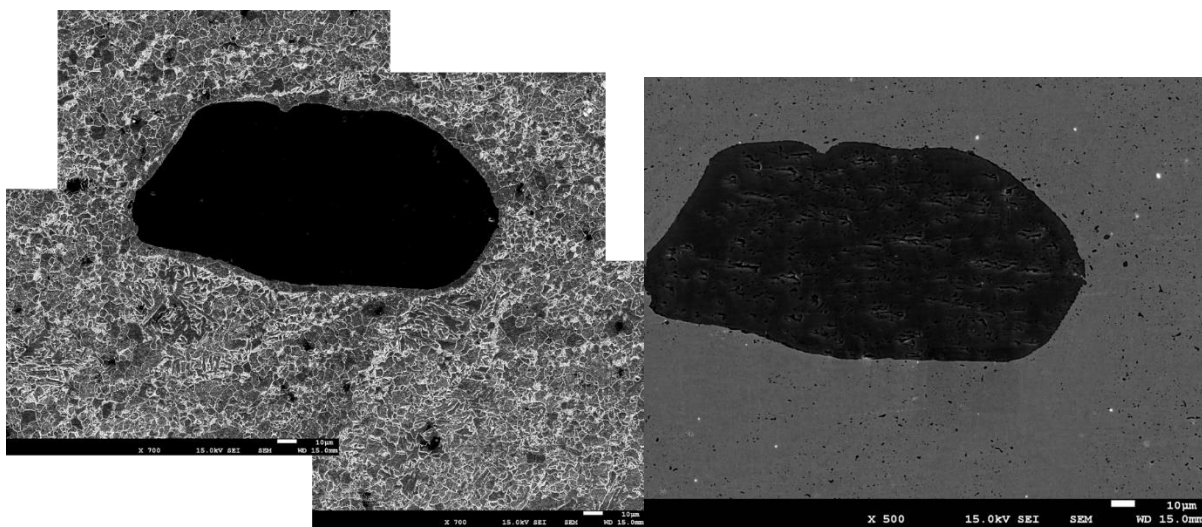

Figure 83: Etched (left) and unetched (right) area surrounding TiO₂ including many black inclusions or defects
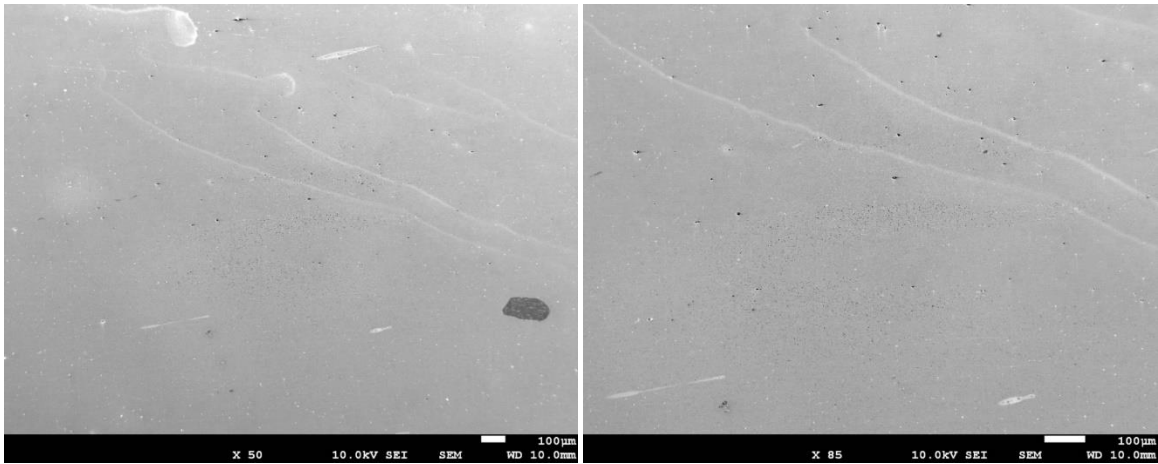
88

Figure 84 Sample C: darker area without etching, lower magnification again showing dark spots
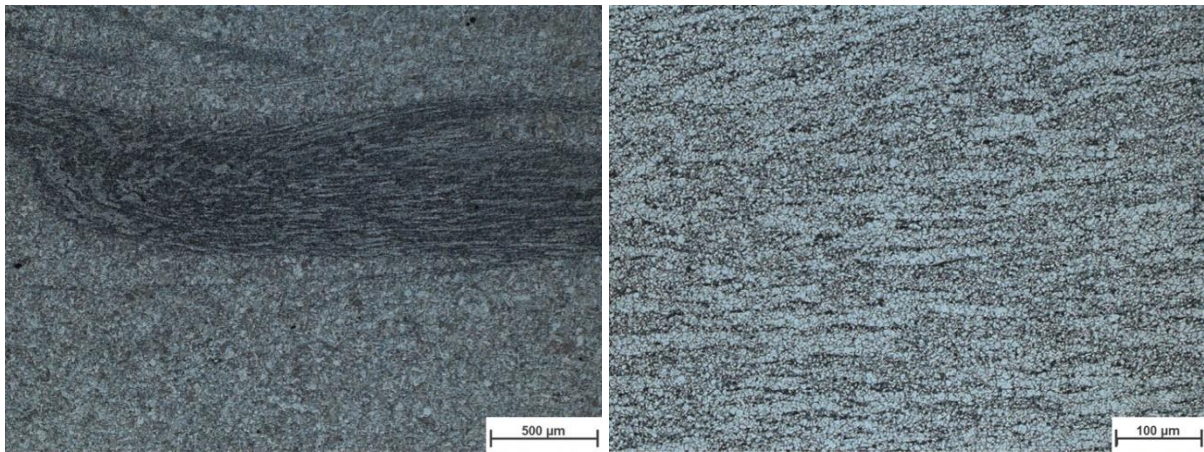

Figure 85 Sample C: LOM of the inclusions or defects

Figure 86 shows a silicon EDS mapping of the region in Figure 84 and Figure 85 with silicon being detected at the defects or inclusions. The slight difference in position on the image is due to movement of the sample during measurement.
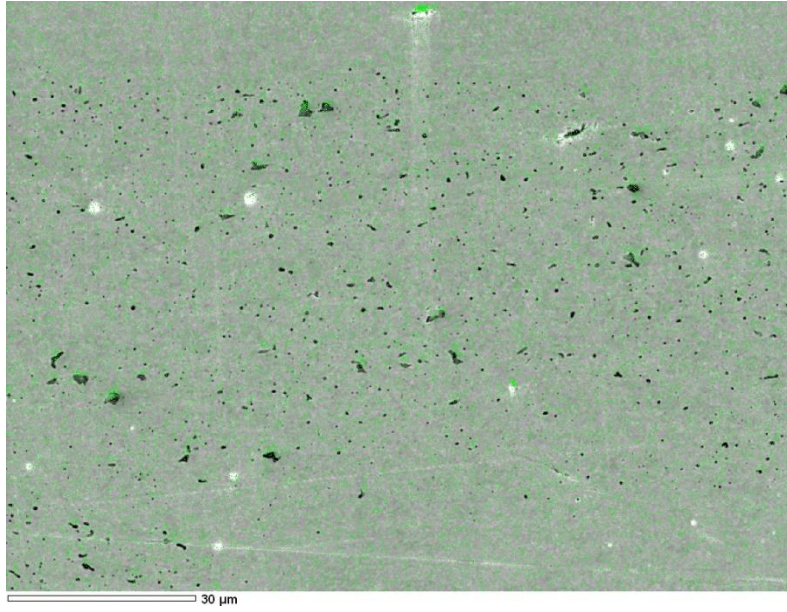
Figure 86 Sample C Si (green) EDS mapping of inclusions or defects showing an overlap

7.5.4. Sample D

Figure 87 shows the microstructure of the center of the sample in a higher resolution.
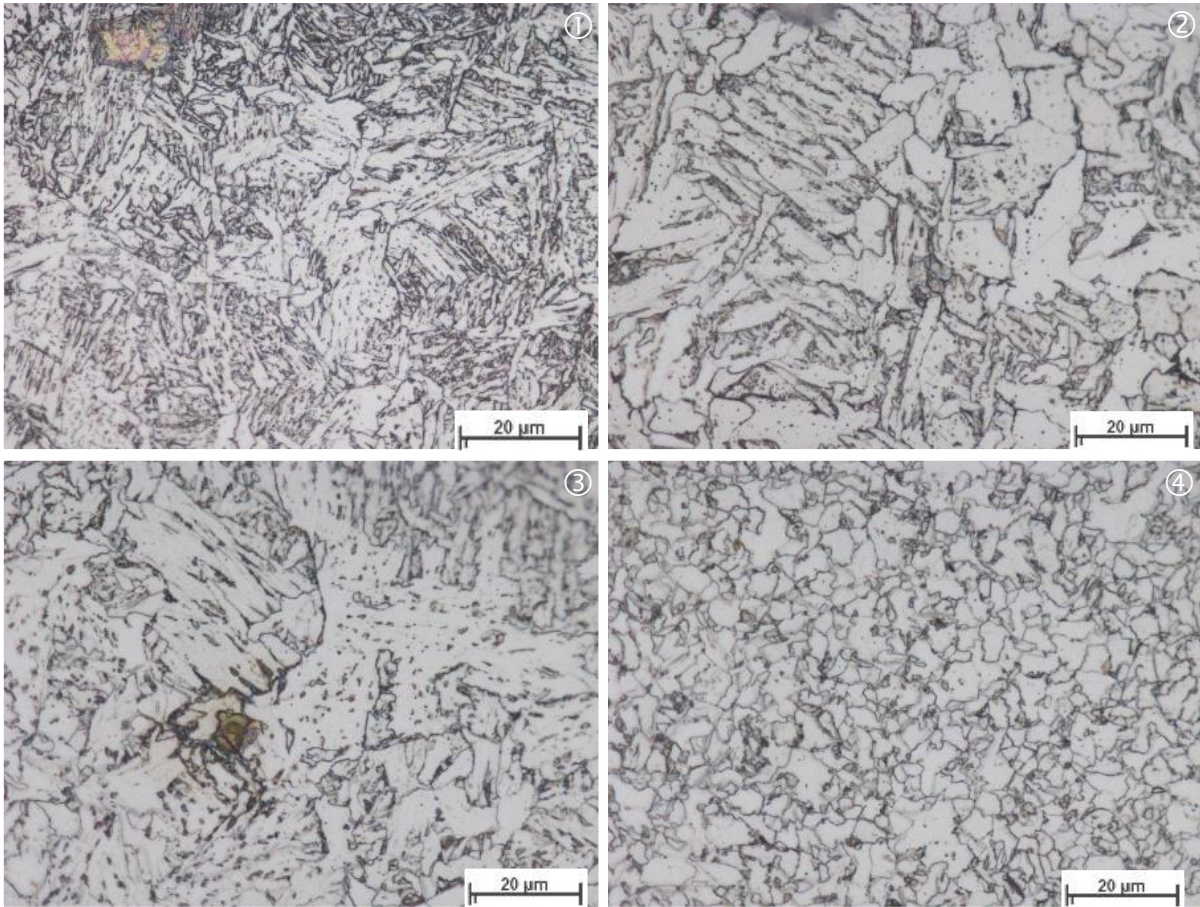
Figure 87 Sample D - LOM microstructure details: ① near surface close to WC abrasion, ② stir zone center and ③ below center, ④ outside TMAZ

Figure 88 shows a lower magnification of the sample surface of sample D with acicular ferrite being present in several areas.
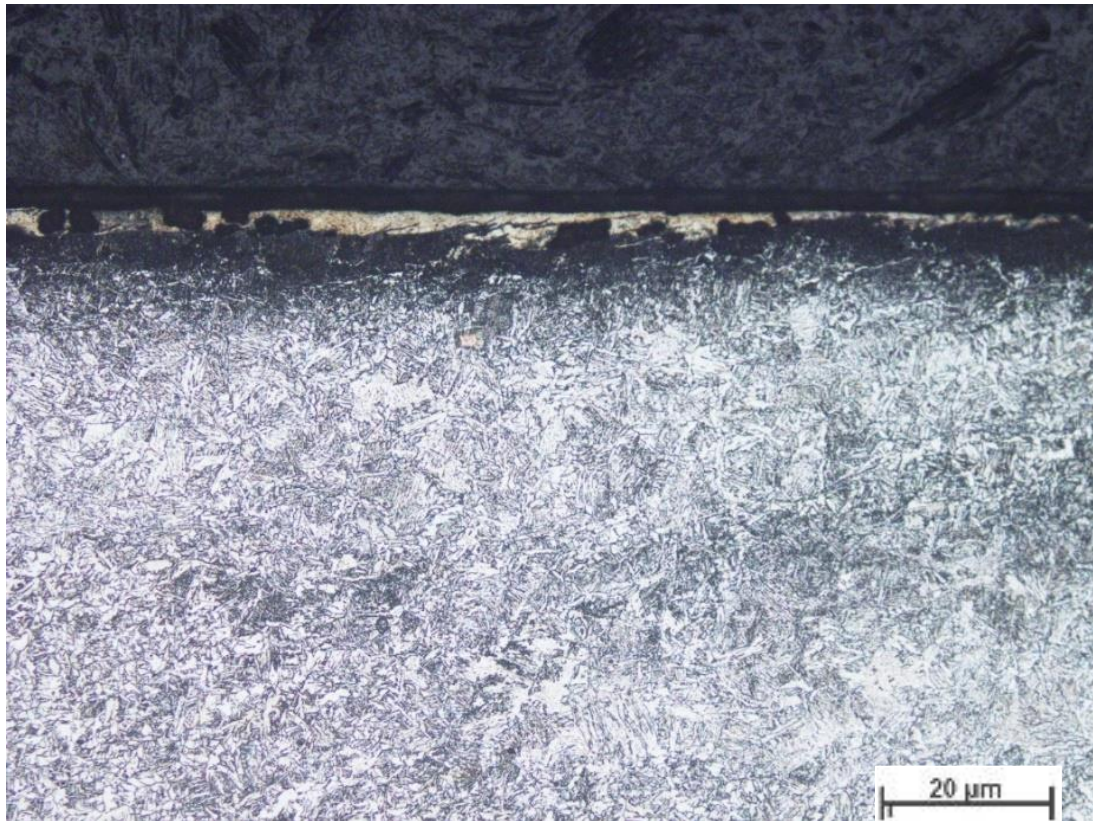
Figure 88 Acicular ferrite in sample D surface

Figure 89 shows the silicon oxide grains in the crack and between the plates.
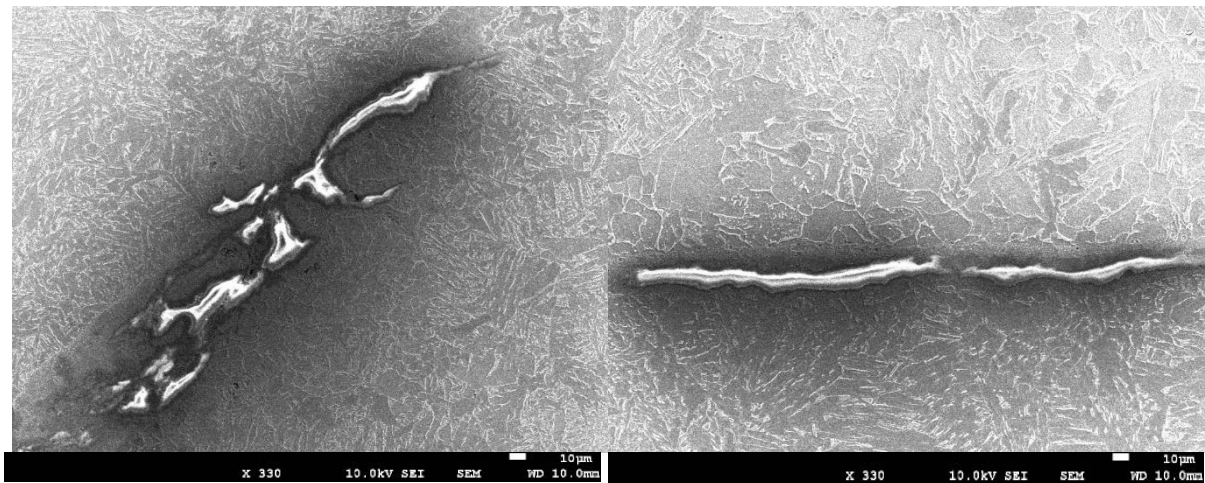
Figure 89 Sample C: Si grains in crack (left) and between plates (right)

Figure 90 shows the center of the weld, etched, unetched and via SEM, the silicon causing a shadow effect on surroundings in the SEM image, which is not present when analyzing regions near TiO_2.
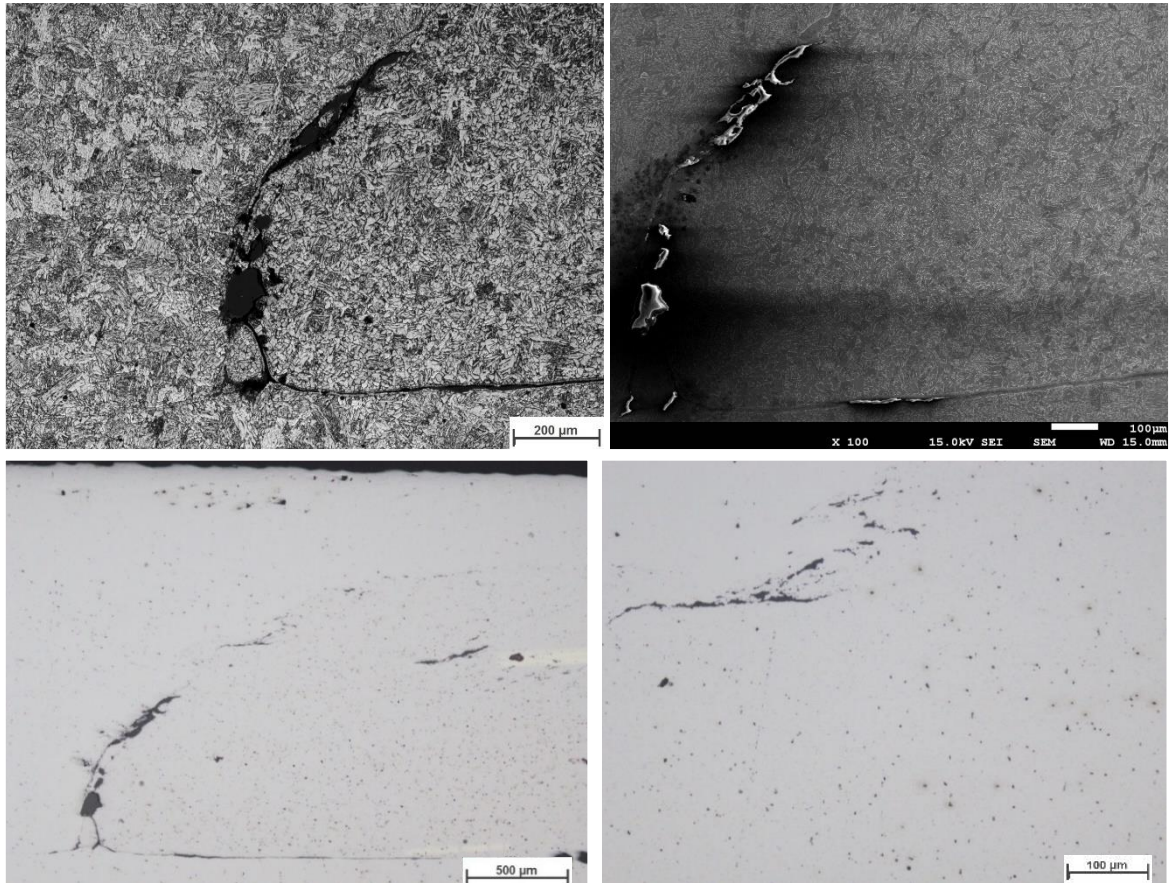
Figure 90 Sample D: Center of the weld LOM etched (top left), SEM etched (top right), LOM unetched (bottom left), region of interest (bottom right)

Figure 91 shows two regions containing acicular ferrite, the lower one being the one which was analyzed via EDS.
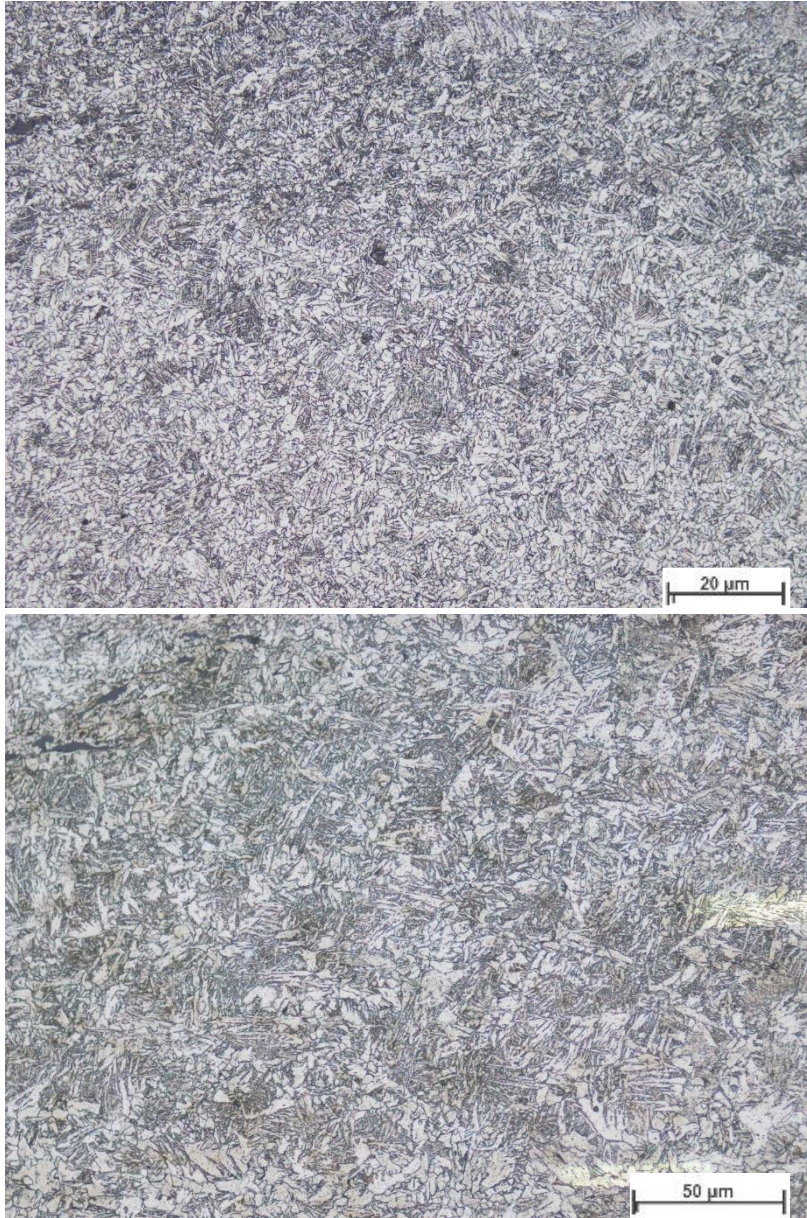
Figure 91 Sample D: Acicular ferrite in Sample D

Figure 92 shows the microstructure close to the crack at the center being primarily ferritic.
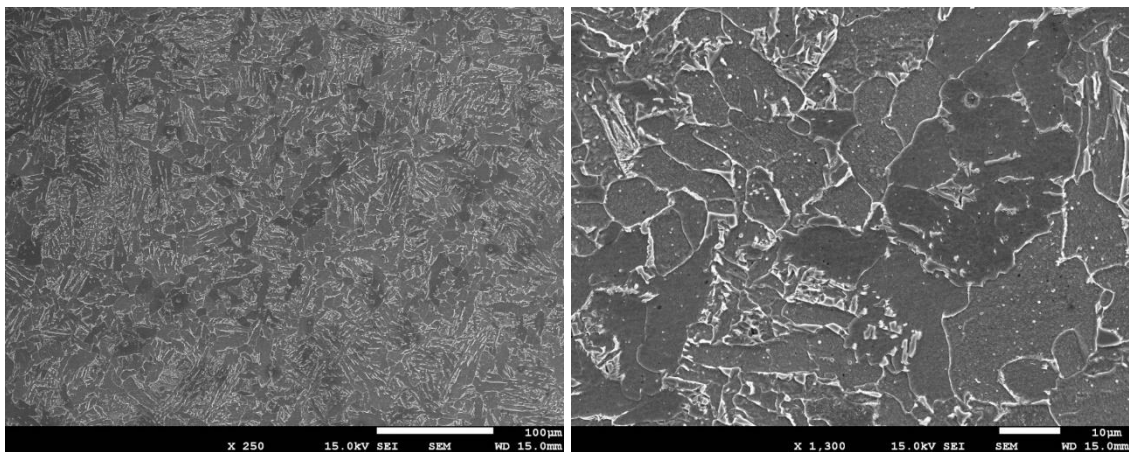
Figure 92 Sample D: area next to crack, showing ferrite grains

7.5.5. Sample E

Figure 93 shows an overview of the center of the sample, with the golden areas covering the surface and tool residue in the mid center.

Figure 93 Sample E: Overview center of the weld showing a distinct pattern and tool abrasion (gold color)

Figure 94 shows the microstructure of the center of the sample in a higher resolution.
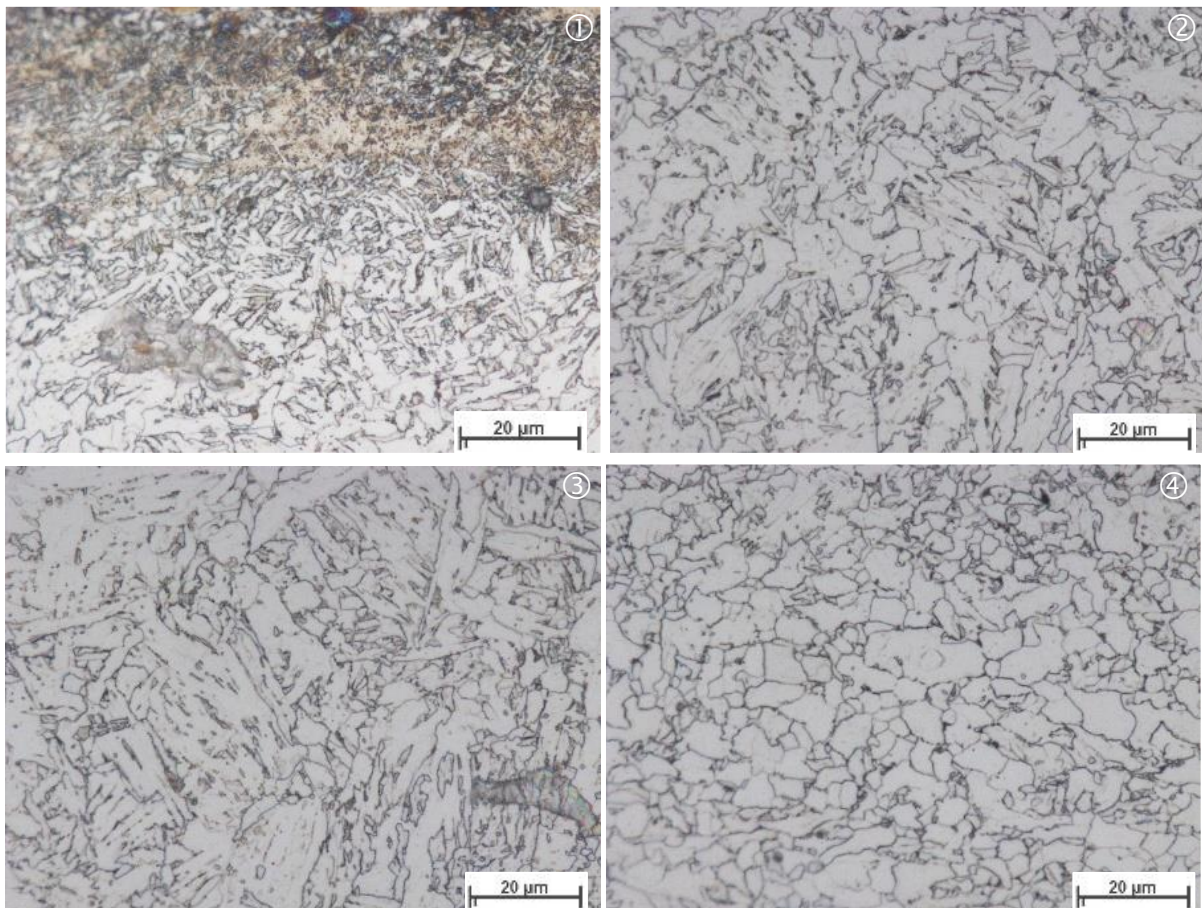
Figure 94 Sample E - LOM microstructure details: ① near surface close to WC abrasion, ② stir zone center and ③ below center ④

Figure 95 shows an LOM of the same pattern as in sample C for sample E
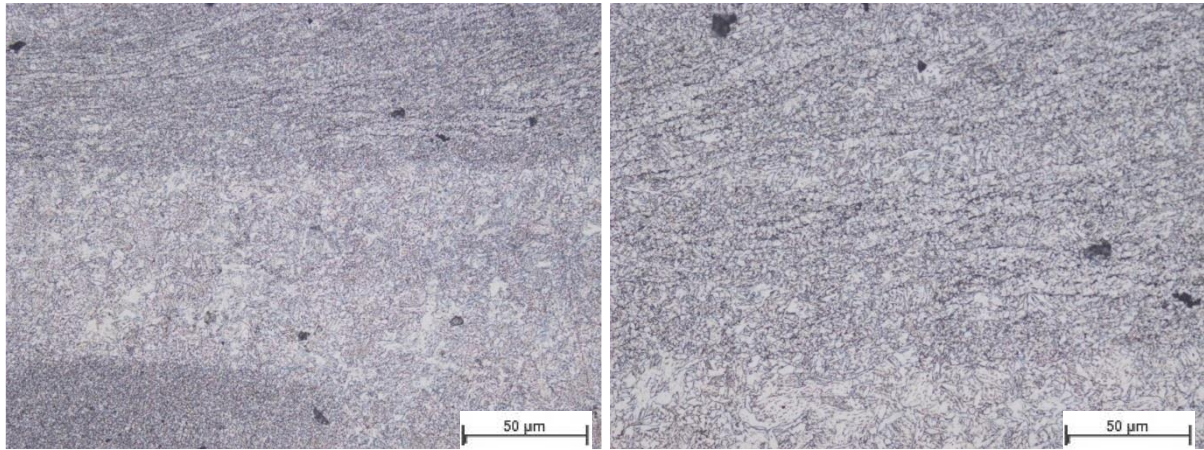
Figure 95 Sample E: LOM of the inclusions or defects

Figure 96 shows a Silicon EDS mapping of pattern region with the Silicon being detected at the defects or inclusions. The slight difference in position on the image is due to movement of the sample during measurement.
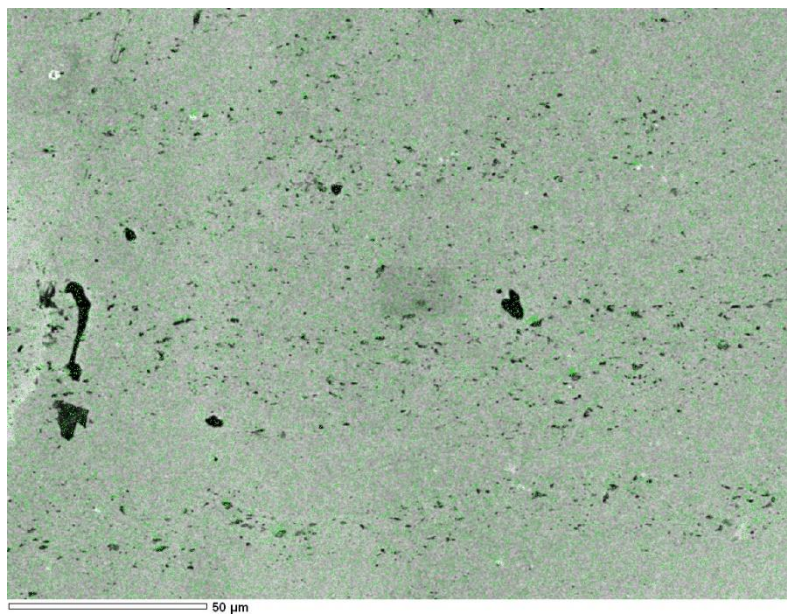
Figure 96 Sample E: Si (green) EDS mapping of inclusions or defects showing an overlap

Figure 97 shows an EDS point scan and the composition of the WC abrasion.
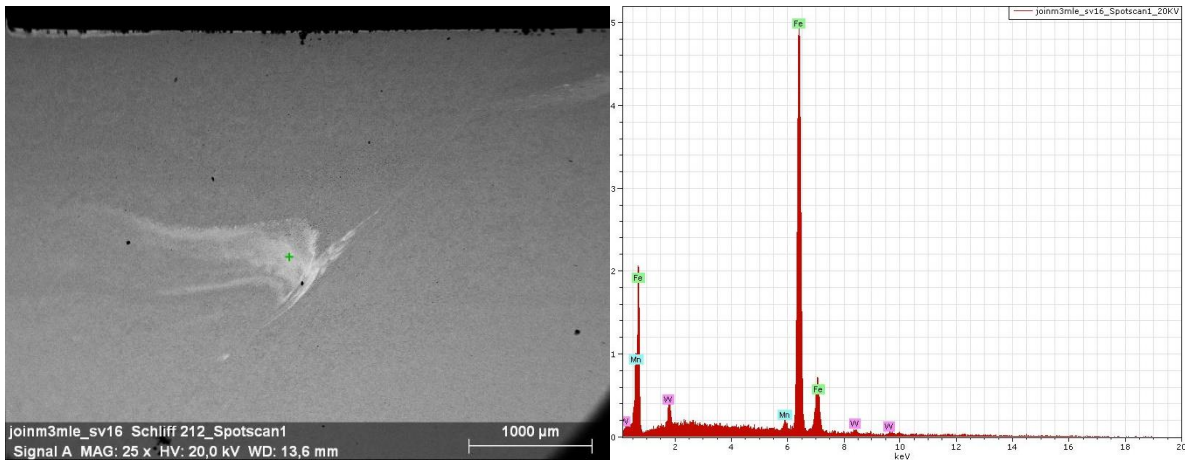
Figure 97 Sample E: EDS analysis of the tool abrasion

7.5.6. Additional hot pressing Samples

In addition to sample F other hot pressing samples were created but not analyzed. To avoid another current breakdown the first heating cycle, meant to weld both cube-halves together was abandoned for subsequent samples and instead the pressing was done at the highest temperature for a second, which also simulates the welding process better, see Figure 98. This short load and the thermal cycle managed to fuse the samples sufficiently.

Figure 98 Adjusted thermal (orange) and pressure (blue) program for hot pressing samples after sample F

7.6. APLI 5l Specifications[6]

Chemical Composition for PSL 1 pipe with t ≤ 0. 984"

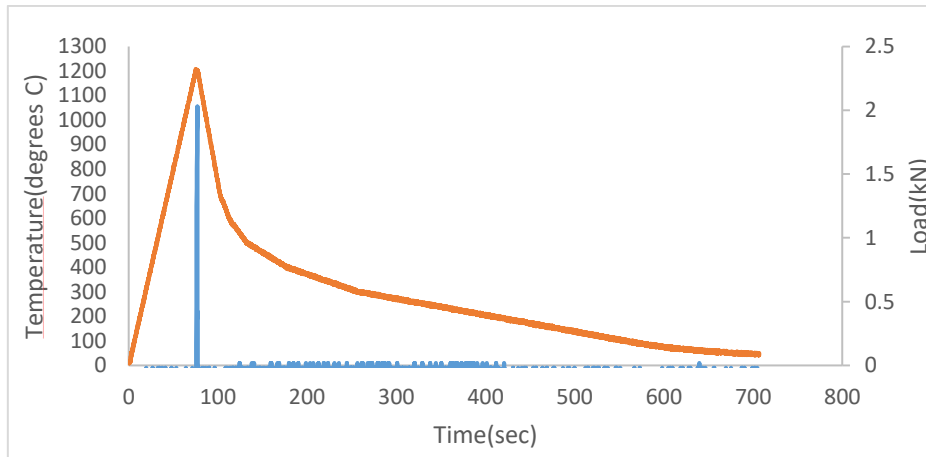| Steel Grade	Mass fraction, % based on heat and product analyses a,g						
	C max b	Mn max b	P max	S max	V max	Nb max	Ti max
Seamless Pipe							
A	0. 22	0. 90	0. 30	0. 30	-	-	-
B	0. 28	1. 20	0. 30	0. 30	c,d	c,d	d
X42	0. 28	1. 30	0. 30	0. 30	d	d	d
X46	0. 28	1. 40	0. 30	0. 30	d	d	d
X52	0. 28	1. 40	0. 30	0. 30	d	d	d
X56	0. 28	1. 40	0. 30	0. 30	d	d	d
X60	0. 28 e	1. 40 e	0. 30	0. 30	f	f	f
X65	0. 28 e	1. 40 e	0. 30	0. 30	f	f	f
X70	0. 28 e	1. 40 e	0. 30	0. 30	f	f	f
Welded Pipe							
A	0. 22	0. 90	0. 30	0. 30	-	-	-
B	0. 26	1. 2	0. 30	0. 30	c,d	c,d	d
X42	0. 26	1. 3	0. 30	0. 30	d	d	d
X46	0. 26	1. 4	0. 30	0. 30	d	d	d
X52	0. 26	1. 4	0. 30	0. 30	d	d	d
X56	0. 26	1. 4	0. 30	0. 30	d	d	d
X60	0. 26 e	1. 40 e	0. 30	0. 30	f	f	f
X65	0. 26 e	1. 45 e	0. 30	0. 30	f	f	f
X70	0. 26e	1. 65 e	0. 30	0. 30	f	f	f

a. Cu ≤ = 0. 50% Ni; ≤ 0. 50%; Cr ≤ 0. 50%; and Mo ≤ 0. 15%
b. For each reduction of 0. 01% below the specified max. concentration for carbon, and increase of 0. 05% above the specified max. concentration for Mn is permissible, up to a max. of 1. 65% for grades ≥ B, but ≤ = X52; up to a max. of 1. 75% for grades > X52, but < X70; and up to a maximum of 2. 00% for X70.
c. Unless otherwise agreed NB + V ≤ 0. 06%
d. Nb + V + TI ≤ 0. 15%
e. Unless otherwise agreed.
f. Unless otherwise agreed, NB + V = Ti ≤ 0. 15%
g. No deliberate addition of B is permitted and the residual B ≤ 0. 001%

Chemical Composition for PSL 2 pipe with t ≤ 0. 984"

Steel Grade	Mass fraction, % based on heat and product analyses									Carbon Equiv a	
	C max b	Si max	Mn max b	P max	S max	V max	Nb max	Ti max	Other	CE IIW max	CE Pcm max
Seamless and Welded Pipe											
BR	0. 24	0. 40	1. 20	0. 025	0. 015	c	c	0. 04	e,l	. 043	0. 25
X42R	0. 24	0. 40	1. 20	0. 025	0. 015	0. 06	0. 05	0. 04	e,l	. 043	0. 25
BN	0. 24	0. 40	1. 20	0. 025	0. 015	c	c	0. 04	e,l	. 043	0. 25
X42N	0. 24	0. 40	1. 20	0. 025	0. 015	0. 06	0. 05	0. 04	e,l	. 043	0. 25
X46N	0. 24	0. 40	1. 40	0. 025	0. 015	0. 07	0. 05	0. 04	d,e,l	. 043	0. 25
X52N	0. 24	0. 45	1. 40	0. 025	0. 015	0. 10	0. 05	0. 04	d,e,l	. 043	0. 25
X56N	0. 24	0. 45	1. 40	0. 025	0. 015	0. 10f	0. 05	0. 04	d,e,l	. 043	0. 25
X60N	0. 24f	0. 45f	1. 40f	0. 025	0. 015	0. 10f	0. 05f	0. 04f	g,h,l	As agreed	
BQ	0. 18	0. 45	1. 40	0. 025	0. 015	0. 05	0. 05	0. 04	e,l	. 043	0. 25
X42Q	0. 18	0. 45	1. 40	0. 025	0. 015	0. 05	0. 05	0. 04	e,l	. 043	0. 25
X46Q	0. 18	0. 45	1. 40	0. 025	0. 015	0. 05	0. 05	0. 04	e,l	. 043	0. 25

X52Q	0. 18	0. 45	1. 50	0. 025	0. 015	0. 05	0. 05	0. 04	e,l	. 043	0. 25
X56Q	0. 18	0. 45f	1. 50	0. 025	0. 015	0. 07	0. 05	0. 04	e,l	. 043	0. 25
X60Q	0. 18f	0. 45f	1. 70f	0. 025	0. 015	g	g	g	h,l	. 043	0. 25
X65Q	0. 18f	0. 45f	1. 70f	0. 025	0. 015	g	g	g	h,l	. 043	0. 25
X70Q	0. 18f	0. 45f	1. 80f	0. 025	0. 015	g	g	g	h,l	. 043	0. 25
X80Q	0. 18f	0. 45f	1. 90f	0. 025	0. 015	g	g	g	i,j	As agreed	
X90Q	0. 16f	0. 45f	1. 90	0. 020	0. 010	g	g	g	j,k	As agreed	
X100Q	0. 16f	0. 45f	1. 90	0. 020	0. 010	g	g	g	j,k	As agreed	
Welded Pipe											
BM	0. 22	0. 45	1. 20	0. 025	0. 015	0. 05	0. 05	0. 04	e,l	. 043	0. 25
X42M	0. 22	0. 45	1. 30	0. 025	0. 015	0. 05	0. 05	0. 04	e,l	. 043	0. 25
X46M	0. 22	0. 45	1. 30	0. 025	0. 015	0. 05	0. 05	0. 04	e,l	. 043	0. 25
X52M	0. 22	0. 45	1. 40	0. 025	0. 015	d	d	d	e,l	. 043	0. 25
X56M	0. 22	0. 45f	1. 40	0. 025	0. 015	d	d	d	e,l	. 043	0. 25
X60M	0. 12f	0. 45f	1. 60f	0. 025	0. 015	g	g	g	h,l	. 043	0. 25
X65M	0. 12f	0. 45f	1. 60f	0. 025	0. 015	g	g	g	h,l	. 043	0. 25
X70M	0. 12f	0. 45f	1. 70f	0. 025	0. 015	g	g	g	h,l	. 043	0. 25
X80M	0. 12f	0. 45f	1. 85f	0. 025	0. 015	g	g	g	i,j	. 043f	0. 25
X90M	0. 10	0. 55f	2. 10f	0. 020	0. 010	g	g	g	i,j	-	0. 25
X100M	0. 10	0. 55f	2. 10f	0. 020	0. 010	g	g	g	i,j	-	0. 25

a. SMLS t>0. 787", CE limits shall be as agreed. The CEIIW limits applied fi C > 0. 12% and the CEPcm limits apply if C ≤ 0. 12%

b. For each reduction of 0. 01% below the specified max. concentration for carbon, and increase of 0. 05% above the specified max. concentration for Mn is permissible, up to a max. of 1. 65% for grades ≥ B, but ≤ = X52; up to a max. of 1. 75% for grades > X52, but < X70; and up to a maximum of 2. 00% for X70.

c. Unless otherwise agreed Nb = V ≤ 0. 06%

d. Nb = V = Ti ≤ 0. 15%

e. Unless otherwise agreed, Cu ≤ 0. 50%; Ni ≤ 0. 30% Cr ≤ 0. 30% and Mo ≤ 0. 15%

f. Unless otherwise agreed

g. Unless otherwise agreed, Nb + V + Ti ≤ 0. 15%

h. Unless otherwise agreed, Cu ≤ 0. 50% Ni ≤ 0. 50% Cr ≤ 0. 50% and MO ≤ 0. 50%

i. Unless otherwise agreed, Cu ≤ 0. 50% Ni ≤ 1. 00% Cr ≤ 0. 50% and MO ≤ 0. 50%

j. B ≤ 0. 004%

k. Unless otherwise agreed, Cu ≤ 0. 50% Ni ≤ 1. 00% Cr ≤ 0. 55% and MO ≤ 0. 80%

l. For all PSL 2 pipe grades except those grades with footnotes j noted, the following applies. Unless otherwise agreed no intentional addition of B is permitted and residual B ≤ 0. 001% .

Tensile and Yield – PSL1 and PSL2

Pipe Grade	Tensile Properties - Pipe Body of SMLS and Welded Pipes PSL 1			Seam of Welded Pipe
	Yield Strength a $R_{t0,5}$ PSI Min	Tensile Strength a Rm PSI Min	Elongation (in 2in A_f % min)	Tensile Strength b Rm PSI Min
A	30,500	48,600	c	48,600
B	35,500	60,200	c	60,200
X42	42,100	60,200	c	60,200
X46	46,400	63,100	c	63,100
X52	52,200	66,700	c	66,700
X56	56,600	71,100	c	71,100
X60	60,200	75,400	c	75,400
X65	65,300	77,500	c	77,500
X70	70,300	82,700	c	82,700

a. For intermediate grade, the difference between the specified minimum tensile strength and the specified minimum yield for the pipe body shall be as given for the next higher grade.

b. For the intermediate grades, the specified minimum tensile strength for the weld seam shall be the same as determined for the body using foot note a.

c. The specified minimum elongation, A_f, expressed in percent and rounded to the nearest percent, shall be determined using the following equation: $A_f = C \frac{A_{xc}^{0,2}}{U^{0,9}}$

Where C is 1 940 for calculation using Si units and 625 000 for calculation using USC units

A_{xc} is the applicable tensile test piece cross-sectional area, expressed in square millimeters (square inches) , as follows

Pipe Grade	Tensile Properties - Pipe Body of SMLS and Welded Pipes PSL 2						Seam of Welded Pipe
	Yield Strength a $R_{t0,5}$ PSI Min		Tensile Strength a R_m PSI Min		Ratio a,c $R_{10,5}IR_m$	Elongation (in 2in) Af %	Tensile Strength d R_m (psi)
	Minimum	Maximum	Minimum	Maximum	Maximum	Minimum	Minimum
BR, BN,BQ,BM	35,500	65,300	60,200	95,000	0. 93	f	60,200
X42,X42R,X2Q,X42M	42,100	71,800	60,200	95,000	0. 93	f	60,200
X46N,X46Q,X46M	46,400	76,100	63,100	95,000	0. 93	f	63,100
X52N,X52Q,X52M	52,200	76,900	66,700	110,200	0. 93	f	66,700
X56N,X56Q,X56M	56,600	79,000	71,100	110,200	0. 93	f	71,100
X60N,X60Q,S60M	60,200	81,900	75,400	110,200	0. 93	f	75,400
X65Q,X65M	65,300	87,000	77,600	110,200	0. 93	f	76,600
X70Q,X65M	70,300	92,100	82,700	110,200	0. 93	f	82,700
X80Q,X80M	80,500	102,300	90,600	119,700	0. 93	f	90,600

a. For intermediate grade, refer to the full API5L specification.

b. for grades > X90 refer to the full API5L specification.

c. This limit applies for pies with D> 12. 750 in

d. For intermediate grades, the specified minimum tensile strength for the weld seam shall be the same value as was determined for the pipe body using foot a.

e. for pipe requiring longitudinal testing, the maximum yield strength shall be ≤ 71,800 psi

f. The specified minimum elongation, A_f expressed in percent and rounded to the nearest percent, shall be determined using the following equation: $Af = C \frac{A_{xc}^{0,2}}{U^{0,9}}$

Where C is 1 940 for calculation using Si units and 625 000 for calculation using USC units

  A_{xc} is the applicable tensile test piece cross-sectional area, expressed in square millimeters (square inches) , as follows
- For circular cross-section test pieces, 130mm^2 (0. 20 in^2) for 12. 7 mm (0. 500 in) and 8. 9 mm (. 350 in) diameter test pieces; and 65 mm^2 (0. 10 in^2) for 6. 4 mm (0. 250in) diameter test pieces.
- For full-section test pieces, the lesser of a) 485 mm^2 (0. 75 in^2) and b) the cross-sectional area of the test piece, derived using the specified outside diameter and the specified wall thickness of the pipe, rounded to the nearest 10 mm^2 (0. 10in^2)
- For strip test pieces, the lesser of a) 485 mm^2 (0. 75 in^2) and b) the cross-sectional area of the test piece, derived using the specified width of the test piece and the specified wall thickness of the pipe, rounded to the nearest 10 mm^2 (0. 10in^2)

  U is the specified minimum tensile strength, expressed in megapascals (pounds per square inch

g. Lower values fo $R_{10,5}IR_m$ may be specified by agreement

h. for grades > x90 refer to the full API5L specification.